Lunar megaregolith mixing by impacts: the spatial diffusion of surface material and its implications for sample interpretation

vorgelegt von

M. Sc. Tiantian Liu

ORCID: 0000-0002-1539-495X

an der Fakultät VI - Planen Bauen Umwelt
der Technischen Universität Berlin
zur Erlangung des akademischen Grades

Doktor der Ingenieurwissenschaften

- Dr.- Ing -

genehmigte Dissertation

Promotionsausschuss:

Vorsitzender: Prof. Dr. Harald Schuh
Gutachter: Prof. Dr. Jürgen Oberst
Gutachter: Prof. Dr. Kai Wünnemann
Gutachter: Prof. Dr. Harald Hiesinger
Gutachter: Prof. Dr. Menghua Zhu

Tag der wissenschaftlichen Aussprache: 24. November 2020

Berlin 2021

PhD Thesis

Lunar megaregolith mixing by impacts: the spatial diffusion of surface material and its implications for sample interpretation

Supervised by:

Dr. Greg Michael & Prof. Dr. Jürgen Oberst

Released by:

Tiantian Liu, MSc

Acknowledgements

First I would like to thank Dr. Jürgen Oberst for giving me the opportunity to work at Technical University Berlin and supporting me extensively throughout my work. I also would like to thank Dr. Menghua Zhu and my previous supervisor Dr. Wenzhe Fa. You gave me support when I was looking for a proper doctoral position, and I appreciate that you told me the potential opportunity to pursue my PhD degree in Germany. Thanks to the Deutsche Forschungsgemeinschaft DFG for supporting me and giving me a great chance to learn from leading experts in the TRR 170.

A very big thank you goes to Dr. Greg Michael, my second supervisor. How fortunate I am to be able to work with him! This work would have never been achieved without his support. He always stood behind me in all the ups and downs. I appreciate his countless hours of discussions. His advice has always helped me to overcome the bottlenecks of my research, and his feedbacks greatly improved the quality of my manuscripts including both the scientific significance and phrasing. Not only that, but he also gave me a lot of warmth and help in my daily life. I spent Christmas with his family and we greeted the new year together. He has let me know that I am not alone in Germany. Greg, Adriana, and their daughter Zizi give me a "home" in Berlin. Thank you so much!

A warm thank you goes to Daniel Wahl, with whom I enjoyed every moment of my time at TU. His kindness and cheerful laugh color my life. Thanks to Philipp Gläser and Daniel Wahl for their great help when I just arrived in Berlin. Thanks to all of my other colleagues at TU, Anastasios Margonis, Ramona Ziese, Haifeng Xiao, Friedrich Damme, Isabel Haase, and Rosemarie Kunkel, who were there for me in all moments.

Thanks to all my colleagues at Freie Universität Berlin. A warm thank you to Sebastian Walter and Dominik Neu for technical support, and to Wilhelm Zuschneid for proof-reading of my manuscripts and this thesis. A warm merci to all the other colleagues: Csilla Orgel, Christian Riedel, Anne Dreißigacker, Tilmann Denk, Christoph Gross, Stephanie Pott, Stephanie Mikulla, Heike Balthasar, and Björn Schreiner.

I am very grateful to Prof. Kai Wünnemann from the Museum für Naturkunde in Berlin for giving me professional guidance regarding impact processes. Thanks to Robert Luther and Natasha Artemieva for giving me valuable advice concerning ejecta deposit. Particularly, I would like to thank Dr. Menghua Zhu again for the fruitful discussions every time he worked in Museum für Naturkunde Berlin. I also wish to thank the other group members and colleagues, Lukas Manske and Tomke Lompa.

Thanks to Harry Becker, Thomas Haber, and Dennis Vanderliek for their great help concerning geochemistry.

Thanks to Alexander Bazilevski for his support during the time I was looking for a postdoctoral position, and it was a good time we work together.

A special merci beaucoup for Jingyan Hao, who brings me much happiness and has become my best friend in Germany.

Finally, I would like to thank my family. Thanks to my parents, who give me unconditional love and the precious freedom to choose the life I want. Thanks to my parents-in-law, who cherish me like a daughter. Thanks to my husband, who understands me, gives me endless support, and spoils me with his love and caring. Finally, I would like to thank all the other friends and people who supported me during all tough times.

Structure of the dissertation

This cumulative dissertation is structured in eight chapters. First an introduction to the formation of the Moon and the important roles of giant impacts (i.e., impact basins) and collected samples on improving understanding of the lunar bombardment history. The two geologic processes, impact cratering and maria volcanic flooding, that are the major mechanism altering the composition of the surface material are also described. Then the methods including the model framework and essential scaling laws are presented. The methods chapter is followed by three original research papers published in peer-reviewed journals. These three papers build on another with the aim to gradually unveil a complete picture of material diffusion by improving the methodological approach from an initially 2D to a 3D model and by expanding the model application from individual basins to a more global study of the melt distribution and to the evolution of mare material:

Research paper I:

Tiantian Liu, Greg Michael, Juliane Engelmann, Kai Wünnemann, and Jürgen Oberst.

Regolith mixing by impacts: Lateral diffusion of basin melt.

Accepted manuscript, Published in *Icarus*, 321, 691–704, 2019, DOI: 10.1016/j.icarus.2018.12.026.

Research paper II:

Tiantian Liu, Greg Michael, Kai Wünnemann, Harry Becker, and Jürgen Oberst.

Lunar megaregolith mixing by impacts: spatial diffusion of basin melt and its implications for sample interpretation.

Accepted manuscript, Published in *Icarus*, 113069, 2020, DOI: 10.1016/j.icarus.2019.113609.

Research paper III:

Tiantian Liu, Greg Michael, Wilhelm Zuschnied, Kai Wünnemann, Jürgen Oberst.

Lunar megaregolith mixing by impacts: Evaluation of the non-mare component of mare soils.

Accepted manuscript, Published in *Icarus*, 114206, 2020, DOI: 10.1016/j.icarus.2020.114206.

They are stand-alone articles, and therefore contain individual introduction and conclusions. As the first author of all three papers. I built the model, reviewed the relevant literature, interpreted the results, and concluded the work. The coauthors participated in the discussion and draft reviewers. Greg Michael and Jürgen Oberst were consulted during drafts preparation of all three papers, as they supervised this doctoral work. In the paper of Chapter 4, Juliane Engelmann provided an important scaling law concerning the distribution of impact melt. In the paper of Chapter 5, Harry Becker contributed to the discussion of geochemical characteristics of lunar

rocks and wrote some discussions concerning interpretations of radioisotopic ages. In the paper of Chapter 6, Wilhelm Zuschneid contributed to the discussion of the lunar volcanic history and the interpretations of modeling results. In all the three papers of Chapters 4-6, Kai Wünnemann offered guidance concerning the impact cratering process.

A general discussion of all three papers, future work, and the synthesis of this dissertation are given in Chapter 7 and Chapter 8. In the following abstract of this thesis, Daniel Wahl and Jürgen Oberst help to translate it into German.

This work is supported by TRR 170, a systematic project studying the late accretion onto terrestrial planets. The goal of TRR170 program is to improve our current understanding of the late-accretion history of the Earth, its Moon, and other terrestrial planets from 4.5 to 3.8 billion years ago. Using a multidisciplinary approach, it aims to provide novel insights into the timing and rates (TRR 170 Area A), chemical budget (TRR170 Area B), and geodynamic implications (TRR170 Area C) of late accretion and will constrain the physicochemical boundary conditions during this time interval. The results in this study contribute to TRR 170 Area A, which helps to unveil the record of early bombardment, and hence to calibrate the cratering record of other solar system objects.

Abstract

The Moon has experienced a great number of impact events since the formation of its crust. The impact cratering process mixes material of different origins leading to a complex surface composition. The samples that were collected from the lunar surface were found to consist of various components. Because of the difficulty to link any particular component to a specific impact event on the Moon, inferences about the origin of some components, and in particular, their association with specific basin forming events, remain uncertain.

In this thesis, a spatially resolved numerical model tracing the evolving distribution of surface material is developed using the Monte Carlo method. Based on this model, components of known origin can be traced in their presence and abundance into the present-day surface material, providing a quantitative aid in interpreting the origin of the different components observed in the returned samples.

Impact melt, the material heated to the high temperature caused by the hypervelocity impact events, is a common product of impact cratering. The age of impact melt and hence the occurrence time of the impact event can be measured using radioisotopic dating techniques based on the isotopic clock of the incorporated radioactive elements. The radioisotopic clock of the elements that possess the relatively low closure temperature (e.g. K-Ar system) can be easily reset by the high temperature. By measuring the abundance of the incorporated radioactive elements, the absolute age of the melt can then be measured. If we understand the abundance of impact melt of different ages, the lunar bombardment history can be well constrained. This thesis is, therefore, first focusing on the evolving distribution of impact melt.

The impact melts of lunar basins whose diameter is larger than 300 km have been of particular interest. They formed earlier than ~3.9 Ga and are of great volume being the great tool to investigate the early bombardment history by linking the melt contained in the lunar samples to these giant basins. Since the impact melts of the later-formed basins are most likely to have a significant presence and to have been identified in the collected samples, this study first focuses on three mid- to late-forming basins (Serenitatis, Crisium, and Imbrium). The lateral diffusion features of these basins' melt along a path passing through them were investigated based on a 2D model. The survival probability of these basins' melt at the Apollo and Luna sampling spots was derived and was found to be consistent with the K-Ar radiometric dates of the samples. The results indicate a substantial mixing of the impact melt from these three basins, particularly the Imbrium melt, at the sampling spots.

The ancient impact melt is important to constrain the early bombardment history. However, the old impact melt appears absent in the lunar samples. In developing the 2D model into a 3D model, a more complete picture of the melt evolving pattern was established where the diffusion

of impact melt over the global surface and with depth was traced. All basin-forming events with known model age and a great number of smaller impact events were simulated in the 3D model. The spatial distributions of all the considered basins were estimated. The average composition of the global surface and the composition at the sampling sites were calculated and compared with the radioisotopic ages of the lunar meteorites and the returned samples. As for the results of the 2D model, the 3D model predicts a significant occurrence of Imbrium melt in the collected samples. In addition, it is expected to have abundant old impact melt at the surface. There is, therefore, likely to be a more ancient impact melt in the samples that could be found by using different radioisotopic techniques.

Non-mare components have been found in the mare soil samples, and in some samples, their abundances are significantly great. The source of those materials is an issue that has been debated for decades. The 3D model was subsequently applied to investigate the mixing mechanism of lunar mare/non-mare components in the upper regolith by incorporating the process of volcanic flooding of the mare basins. The evolving features of mare/non-mare material were pictured, and the overall concentration of non-mare components over the mare surfaces and the sampling sites were calculated. The results show that the overall mare surface has mixed some non-mare components, and the non-mare component that was found to be much more abundant than the average mixture is probably caused by some other geologic processes.

In summary, in this thesis, an innovative methodological approach was developed to trace the material diffusion with long-time impact mixing on the Moon. It allows for a more precise statistical analysis of the mixing of impactites into lunar soils which is key for an accurate interpretation of the ages of lunar samples. In the future, this approach can be further refined by involving the more accurate scaling laws of impact cratering and by considering the impact mixing of small-scaled impact craters. In addition, this approach can be used to investigate the diffusion of different components of interest, such as the KREEP materials which may give insight into our understanding of the lunar differentiation history.

Zusammenfassung

Der Mond hat seit der Bildung seiner Kruste eine große Zahl von Einschlagsereignissen erlebt. Beim Impaktkraterprozess vermischt sich Material unterschiedlichen Ursprungs, was zu einer komplexen Oberflächenzusammensetzung führt. Es wurde festgestellt, dass die Proben, die von der Mondoberfläche entnommen wurden, aus verschiedenen Komponenten bestehen. Einige Komponenten wurden als Impaktschmelze erkannt, aber wegen der Schwierigkeit, eine bestimmte Komponente mit einem bestimmten Impaktereignis auf dem Mond in Verbindung zu bringen, bleiben Rückschlüsse auf den Ursprung einiger Komponenten und insbesondere ihre Verbindung mit bestimmten beckenbildenden Ereignissen unsicher.

In dieser Arbeit wird ein räumlich aufgelöstes numerisches Modell entwickelt, das die sich entwickelnde Verteilung des Oberflächenmaterials mit Hilfe der Monte-Carlo-Methode nachzeichnet. Auf der Grundlage dieses Modells können Komponenten bekannten Ursprungs in ihrer Anwesenheit und Häufigkeit im heutigen Oberflächenmaterial zurückverfolgt werden, was eine quantitative Hilfe bei der Interpretation des Ursprungs der verschiedenen in den zurückgesandten Proben beobachteten Komponenten darstellt.

Einschlagschmelze, das Material, das auf die durch die Hypervelocity-Einschlagereignisse verursachte hohe Temperatur erhitzt wird, ist ein häufiges Produkt der Einschlagkraterbildung. Das Alter der Impaktschmelze und damit der Zeitpunkt des Auftretens des Impaktereignisses kann mit Hilfe von Radioisotopen-Datierungstechniken gemessen werden, die auf der Isotopenuhr der eingebauten radioaktiven Elemente basieren. Die radioisotopische Uhr der Elemente, die die relativ niedrige Verschlusstemperatur besitzen (z.B. K-Ar-System), kann durch die hohe Temperatur leicht nachgestellt werden. Durch Messung der Häufigkeit der eingebauten radioaktiven Elemente kann dann das absolute Alter der Schmelze gemessen werden. Wenn wir die Häufigkeit der Einschlagsschmelze unterschiedlichen Alters verstehen, kann die Bombardierung und späte Akkretionsphase des Mondes gut eingegrenzt werden. Diese Arbeit konzentriert sich daher zunächst auf die sich entwickelnde Verteilung der Einschlagsschmelze.

Von besonderem Interesse sind die Einschlagsschmelzen von Mondbecken, deren Durchmesser größer als 300 km sind. Sie bildeten sich früher als ~3,9 Ga und sind somit ein wichtiges Werkzeug zur Untersuchung der frühen Bombardierungsgeschichte, indem sie die in den Mondproben enthaltene Schmelze mit diesen riesigen Becken in Verbindung bringen. Da die Einschlagsschmelzen der später entstandenen Becken signifikant vorhanden und in den gesammelten Proben identifiziert worden sind, konzentriert sich diese Studie zunächst auf drei mittel- bis spätgebildete Becken (Serenitatis, Crisium und Imbrium). Die lateralen Diffusionsmerkmale der Schmelze dieser Becken entlang eines durch sie verlaufenden Pfades

wurden auf der Grundlage eines 2D-Modells untersucht. Die Überlebenswahrscheinlichkeit der Schmelze dieser Becken an den Apollo- und Luna-Probenahmestellen wurde abgeleitet und als konsistent mit den radiometrischen K-Ar-Daten der Proben befunden. Die Ergebnisse deuten auf eine erhebliche Vermischung der Impaktschmelze aus diesen drei Becken, insbesondere der Imbrium-Schmelze, an den Probenentnahmestellen hin.

Die alte Impaktschmelze ist wichtig, um die frühe Bombardierungsgeschichte einzugrenzen. Diese scheint jedoch in den Mondproben nicht vorhanden zu sein. Bei der Entwicklung des 2D-Modells zu einem 3D-Modell wurde ein vollständigeres Bild des Musters der Schmelzentwicklung erstellt, bei dem die Diffusion der Impaktschmelze über die globale Oberfläche und mit der Tiefe verfolgt wurde. Alle beckenbildenden Ereignisse mit bekanntem Modellalter und eine große Anzahl kleinerer Einschlagsereignisse wurden im 3D-Modell simuliert. Die räumlichen Verteilungen aller betrachteten Becken wurden geschätzt. Die durchschnittliche Zusammensetzung der globalen Oberfläche und die Zusammensetzung an den Probenentnahmestellen wurden berechnet und mit dem Radioisotopenalter der Mondmeteorite und der zurückgesandten Proben verglichen. Was die Ergebnisse des 2D-Modells betrifft, so sagt das 3D-Modell ein signifikantes Vorkommen von Imbriumschmelze in den gesammelten Proben voraus. Darüber hinaus wird erwartet, dass es an der Oberfläche reichlich alte Einschlagsschmelze gibt. Es ist daher wahrscheinlich, dass in den Proben ältere Impaktschmelze vorhanden ist, die mit verschiedenen Radioisotopentechniken gefunden werden könnte.

In Mare-Bodenproben wurden auch Nichtmarebestandteile gefunden, und in einigen Proben sind ihre Häufigkeiten signifikant. Die Herkunft dieser Materialien ist ein Thema, das seit Jahrzehnten diskutiert wird. Das 3D-Modell wurde anschließend angewandt, um den Mischungsmechanismus von lunaren Stuten-/Nichtstutenkomponenten im oberen Regolith zu untersuchen, indem der Prozess der vulkanischen Überflutung der Marebecken mit einbezogen wurde. Die sich entwickelnden Merkmale des Mare-/Nichtmarematerials wurden abgebildet, und die Gesamtkonzentration der Nichtmarekomponente über die Mareoberflächen und die Probenentnahmestellen wurde berechnet. Die Ergebnisse zeigen, dass die gesamte Mareoberfläche einige Nichtmarekomponenten gemischt hat, und die Nichtmarekomponente, die viel häufiger als die durchschnittliche Mischung vorkam, ist wahrscheinlich auf andere geologische Prozesse zurückzuführen.

Zusammenfassend lässt sich sagen, dass in dieser Arbeit ein innovativer methodischer Ansatz entwickelt wurde, um die Materialdiffusion mit Langzeitwirkung der Vermischung auf dem Mond zu verfolgen. Er ermöglicht eine präzisere statistische Analyse der Vermischung von Impaktiten in Mondböden, was für eine genaue Interpretation des Alters der Impaktiten von entscheidender Bedeutung ist.

List of Abbreviations

Abbreviations	Variables or parameters
SFD	Size-Frequency Distribution
PF	Production Function
CF	Chronology Function
D	Crater diameter in km
D_{max}	The maximum crater diameter in simulations
D_{min}	The minimum crater diameter in simulations
D_t	Diameter of transient craters
R_t	Radius of transient craters
N	Number of craters with diameters >D per km^2 per Ga
D_Q	Simple-complex transition diameter (21 km)
d_{exc}	Excavation depth
d_t	Transient crater depth
V_{exc}	Volume of the excavated material during the formation of a crater
V_{melt}	Volume of impact melt
δ	Ejecta thickness
δ_m	Impact melt thickness in ejecta
f_m	Fraction of impact melt in ejecta
r	Distance from crater center
t	Occurrence time of impact events
μ	Mixing ratio of local material to ejecta
h_{min}	The thickness of the farthest ejecta
t_{end}	Rough cessation time of the main filling among mare regions

List of Figures

Figure 1 Lunar impact history. (a) Lunar production function (Neukum, 1983). (b) Lunar chronology function (Neukum, 1983). (c) Impact rate showing two debating scenarios of the early bombardment history (Bottke & Norman, 2017). 5

Figure 2 Summary of proposed various opinions on lunar impact flux (after Zellner, 2017). 6

Figure 3 Series of cross-section diagrams showing progressive development of a small, bowl-shaped simple impact structure (after French 1998): (a) contact/compression stage; (b) start of excavation stage; (c) middle of excavation stage; (d) end of excavation stage; (e) start of modification stage. The generated high temperature melts part of the target material which is shown in black in (c)-(e).....10

Figure 4 An example of impact ejecta on the Moon. (a) A small Copernican-aged crater (25.876°S, 136.081°E; ~270 m in diameter). The ejecta including continuous deposits (ejecta blanket), discontinuous deposits, and rays display high reflectance. (b) An enlarged view of the area outlined by the dashed square in (a).....11

Figure 5 Different morphology of impact craters on the Moon. (a) Simple crater (Moltke, D = 6 m). (b) Central peak crater (Copernicus, D = 96 km). (c) Multi rim basin (Orientale basin, D = 327 km). D is the diameter of craters.....11

Figure 6 An example of impact melt pool on the Moon: The young crater Giordano Bruno (a; 21 km diameter) and a giant swirl of impact melt on the west of the crater floor (b) (Image credit: NASA/GSFC/ASU). 12

Figure 7 Different approaches to determining extent and flux of mare basalts (after Head and Wilson 1992): returned samples (A), Surface exposure of deposits (B), Stratigraphic assessment of volumes (C), accounting for probable volcanism in the period of early bombardment (D), flux on the basis of combined approaches (E) (after Head & Wilson, 1992; Hiesinger et al., 2011). 16

Figure 8 Percentage of chemically estimated non-mare components in lunar soil samples versus distance from a mare-highland boundary. Data for individual sampling stations at the Apollo 15 and 17 landing sites are shown in greater detail in the inset (Rhodes, 1977). 17

Figure 9 Progress of the model development and the specification of the model.....20

Figure 10 Calculated distribution of the ejecta thickness with different impact velocities using iSALE-2D numerical approach. The target material is nonporous, cohesionless, and has a coefficient of friction of 0.6 (Luther et al., 2018). 22

Figure 11 Comparison of melt volumes as a function of transient-cavity diameter where a wide range of projectile types and impact velocities was considered (Cintala & Grieve, 1998). ...23

Figure 12 Thickness of ejecta and melt with the distance from crater center based on the simulations with various projectile sizes (a) and impact velocities (b). vi and L are the impact velocity and diameter of projectiles, respectively. 24

Figure 13 Schematic of the model where the white represents unheated material, red is the impact melt generated from the first impact event when time is t_1, and blue is the melt from the second impact at time t_2. The arrow in (d) points at the region of superposing ejecta....28

Figure 14 Schematic showing typical geometry of melting zone in iSALE modeling, with the impact-induced melt zone (red) and excavation zone in half space (grey, after Zhu et al. 2015). The calculation of V_{exc} in this study is on the basis of the simplified excavation zone shown as an area that filled with black slash.....29

Figure 15 Distribution of ejecta and melt with increasing distance from the crater center, where black, red and blue are from craters with diameter as 300, 100, and 5 km, respectively. Dashed and solid lines are on the basis of theoretical and compressed 2D models, respectively. (a) Ejecta thickness distribution. (b) Melt thickness distribution (c) Melt percentage in ejecta. (d) Ejecta (solid lines, left *y*-axis) and melt volume (lines with dots, right *y*-axis) in a compressed 2D model taking the band width of 1 m. 31

Figure 16 Schematic distribution of excavated materials for a crater half-space inside the band when reducing the problem to two dimensions. (a) The excavated material in the narrow band of the 2D model is traced (blue). This material would be radially distributed as indicated by the black arrows. (b) The excavated materials are distributed within five radii (semicircle outlined by dashed curves), where the farther locations receive less absolute melt quantity, but it nevertheless makes up a greater fraction of the ejecta there, indicated by the darker blue. To conserve the mass in 2D, the ejecta materials that would be deposited outside the band are added into it. (c) The band therefore possesses more ejecta material appearing the much darker blue. This compensates ejecta generated by craters outside the band that the model does not record, while maintaining a realistic average transport distance. 33

Figure 17 A band passing along the great circle through the mid- to late-forming Imbrium, Serenitatis, and Crisium basins, where the solid and dashed outlined circles indicate the rims of final and transient craters, respectively.....34

Figure 18 Evolving distribution of impact melt after one (first column), 30 (second column), 50 (third column), 100 (fourth column) and 150 (last column) impact events, where D_t is fixed to be 40 km. Both a1-a5 (linear depth) and b1-b5 (logarithmic depth) show the spatial distribution of the impact melt from the first impact event. The latter better displays the melt distribution at the near surface. The distribution of total melt volume of the first impact event (c1-c5) indicates that the generated impact melt is depleted by the re-melting process of subsequent impact events. The melt that was transported farthest has the smallest volume. The total melt volume distribution is shown in e1-e5. More and more impact melt is generated with the increasing number of impact events, but the local diversity is quite strong. In a1-a5, b1-b5, and d1-d5, depth is referenced to the surface boundary, and thus shows no topography. Note that all the calculations concerning melt volume are based on a band of 1 m in width. 37

Figure 19 (a) Spatial distribution of impact craters, where bigger points represent the larger impact craters (but not to scale), and different colors are applied to better distinguish the impact positions. (b), (c), and (d) show the spatial distribution of melt from impact 'b', 'c', and 'd', respectively, the impact location of which is denoted by the arrows in (a). b_{next} in (a)

points out the location of the impact that occurred after impact 'b'. The distribution of melt volume of impact 'b', 'c', and 'd' is shown in (e), (f), and (g), respectively. Note that all the calculations concerning melt volume are based on a chosen band width of 1 m. 39

Figure 20 (a) Exponential decay rate function for crater size-frequency over time (Neukum, 1983). (b) Spatial distribution of impact centers. The locations of Imbrium, Crisium, and Imbrium basin are denoted by the arrows. (c) to (e) show the present day distribution of impact melt of Serenitatis, Crisium, and Imbrium basin, respectively. The D_t of each basin is marked on top of each figure. Depth is referenced to surface boundary, and thus shows no topography. The arrows in (c) and (e) denote the re-excavated Serenitatis and Crisium melt, respectively. 41

Figure 21 (a) The distributions of melt fraction with depth, where the red, green, and blue indicate the melt from Serenitatis, Crisium, and Imbrium basins, respectively. The dots on curves indicate the thickness of the simplified stack layers. (b) The local distribution of melt volume. The arrows point out the peak values caused by the three basins. (c) The distributions of melt volume with age. The arrows point out the melt generated by the three basins. Note that all the calculations concerning melt volume are based on a chosen band width of 1 m. 43

Figure 22 Average fraction of melt from Serenitatis basin (a), Crisium basin (b), and Imbrium basin (c) in the top 0.1 m (the first stack layer). The black dashed lines indicate the center of each basin. The figures are plotted twice: the red, green, and blue shaded plots are Serenitatis, Crisium, and Imbrium melt in linear scale; the grey shaded plots are the same data in logarithmic scale to show the small values. The arrows in (a) to (c) point out the relative distances between the Apollo and Luna sampling sites and the center of each basin, where 'A' and 'L' mean 'Apollo' and 'Luna', respectively. (d) Relative age probability plots of the K-Ar ages of lunar highland rocks for the Apollo and Luna returned samples, where Apollo 14, 15, 16, and Lunar 20 highland samples have 25, 8, 41, 36 and 7 determinations, respectively (after Michael et al. 2018). The red, green, and blue dashed lines indicate the calculated possible formation times of Serenitatis (4.13 Ga), Crisium (4.09 Ga), and Imbrium (3.88 Ga) basins, respectively. Implications for the choice of future sampling sites 47

Figure 23 Map of basins. Circles mark the estimated transient cavities of 30 basins, and the numbers indicate their estimated ages (Orgel et al., 2018). Filled stars mark the locations of Apollo 14-17 (A14-17) and Luna 20 (L20) sampling sites. The background image is Lunar Reconnaissance Orbiter Camera (LROC) Wide Angle Camera (WAC) mosaic (<75° in latitude) (Robinson et al., 2010). The ages are based on recent work by Orgel et al. (2018). 56

Figure 24 (a) Size distribution of basins normalized to the diameter of Imbrium basin. The formation times of SPA and Imbrium basin from Orgel et al. (2018) are $\mu 4.31 - 0.021 + 0.019$ $\mu 3.87 - 0.046 + 0.035$ Ga, respectively. (b) Relative probability plot of $^{40}Ar/^{39}Ar$ from 65 impact melt clasts in lunar meteorites (after Fernandes et al. 2013). The vertical scale is linear. The peak near 3.8 Ga is commonly interpreted to reflect the age of the

Imbrium impact. (c) Fraction of melt component (i.e., relative melt abundance among all the generated melt) in the top one meter of lunar near-surface (left scale). The expected melt generated by SPA, Imbrium and Orientale basins are indicated by three vertical arrows. To show the small melt quantity from smaller impacts, melt fractions have been normalized to the absolute melt fraction derived from the second most abundant melt reservoir, the Imbrium basin (i.e., its relative abundance is equal to 1.0). The crater formation rate (right scale) shows that the high impact rate in the early lunar history is accompanied by a greater melt production. Note that if melt fractions were normalized to SPA melt fractions, the relative quantity of other melt fractions would be so small that specific distribution features are easily masked. Thus, the relative abundance of SPA melt fraction exceeds 1.0, and the exact value is not presented.....59

Figure 25 The global present-day distribution of melt from Imbrium (a), Crisium (b), and (c) Serenitatis basin in the near-surface (top five meters). Warmer colors indicate higher melt fractions (i.e., fraction of basin melt among all impact melt). Red stars indicate Apollo 14-17 and Luna 20 sampling sites. The main coverage of Imbrium and Crisium ejecta is indicated by the dashed regions. The black arrows in (c) indicate re-excavation zones of Serenitatis melt. (d)-(f) are the expected Imbrium, Crisium and Serenitatis melt abundances without local mixing processes.....61

Figure 26 Relative distribution of K-Ar dates obtained on impact melt breccias at the Apollo 14-17 and Luna 20 sampling sites from samples (upper diagrams, Michael et al. 2018) in comparison with relative melt abundances at the Apollo 14-17 and Luna 20 sampling sites based on simulations (lower histograms; relative abundance among all the generated melt). The simulation data reflect melt abundances over a radius of 50 km at each landing site in the top 1 m of the near-surface. Model histograms are shown in black (absolute scale, left) and in grey (logarithmic scale, right). In the black histograms, the peaks caused by Imbrium (3.87 Ga) and Crisium (4.07 Ga) melt are highlighted by red and green color, respectively. Both ages were calculated based on the Neukum (1983) crater chronology and decay constants of that time, which are also the basis of the impactor flux used in our model (see text for further explanation). Note that Pb-Pb ages of phosphates suggest that the true age of the Imbrium basin is probably 3.92±0.02 Ga (the semitransparent-red bar, Snape et al., 2016). Stöffler (2006) suggested that Crisium-derived melt was 3.95-3.85 Ga (the semitransparent-green bars). Overall, the abundance of Imbrian 'ages' near 3.87 Ga at the Apollo landing sites agree with predictions from the model, whereas older K-Ar ages are much less common or do not occur (Apollo 15). 64

Figure 27 Predicted melt component in the top one meter within the SPA region.....67

Figure 28 Example of 1000 points that are evenly distributed on a sphere using a Fibonacci lattice.....73

Figure 29 The migration of the melt generated by the first impact event, where the Dt of all the simulated craters is 50 km. Panels (a) to (f) show the spatial distribution of melt of the first impact after it was gardened by 0, 10, 30, 50, 100 and 150 impact events. Warmer colors

indicate a higher melt volume, and grey areas indicate a melt fraction of less than 10-3. The initial distribution of melt from the first impact is shown in detail in the inset of (a). The melt is distributed over a larger area by the impact gardening, but the majority is still located close to where it formed. The melt vacant zone "va" in the inset of (b) results from the excavation process. The melt is redistributed over "va" indicated by "rf" in the inset of (c). (g) The decreasing total volume of melt from the first impact (left scale) and the percentage of the remaining quantity (right scale). The arrows indicate the total melt volume at the stages (a) to (f). (h) The evolving melt abundance with depth, where blue, green, and grey colors represent the top 50 m, 50-500 m, and deeper than 500 m, respectively. If the melt-enriched region is gardened, especially the cavity of the first crater, the melt abundance of the top layer can decrease, such as at the time labeled "P". The mark "V" indicates a re-excavation event bringing buried melt back to the surface. 75

Figure 30 Schematic example of the filtering method to remove inconsequential gardening events. The considered impact is highlighted in green; its continual ejecta region in grey. Filtering steps (a) to (d). 76

Figure 31 Comparison of the distribution of impact events after filtering. (a) Cumulative distribution of differently sized and of (b) differently-aged craters. The solid and dashed lines represent impacts before and after filtering. (c) Staggered relative melt abundance at various depths after filtering procedure. 77

Figure 32 Staggered absolute difference of relative melt abundance at various depths when two times (a) and ten times (b) more melt is produced in individual impacts. 78

Figure 33 Staggered absolute difference of relative melt abundance at various depths when 5% less (a) and 5% more (b) melt is ejected during the formation individual impacts. 78

Figure 34 The global present-day distribution of melt from Serenitatis basin in the near-surface (top five meters) when Serenitatis basin forms later than Nectaris basin. 78

Figure 35 (a1-a4) A schematic of the filling of volcanic material. (b) The thickness distribution of mare material (after De Hon 1974; De Hon 1979; De Hon & Waskom 1976; Hörz et al. 1991) over the Oceanus Procellarum (P), and the Mare Frigoris (Fr), Fecunditatis (Fe), Humorum (H), Imbrium (I), Serenitatis (S), Tranquillitatis (T), Nectaris (N) and Crisium (C). The red stars indicate the locations of Apollo ("A") and Luna ("L") sampling sites. 92

Figure 36 The distribution of non-mare material in the top 5 m. In the first scenario the mare material is emplaced instantaneously (first column, a and b); in the second scenario, it is emplaced by continuous flooding with time (second column, c and d). (a) and (c) present the abundance of non-mare material that is laterally; (b) and (d) show the abundance of non-mare component that was vertically excavated from the beneath. The upper sub-plots of (e) and (f) present histograms of laterally and vertically transported non-mare abundance of the mare regions when the mare material is emplaced instantaneously, and their lower sub-plot the absolute differences of the percentage caused by the continual filling. 98

Figure 37 The fraction of laterally (a) and vertically (b) transported non-mare material with varying parameters concerning mare filling in the top 5 m. The results based on the

different studied parameters are indicated by four grey zones. For better comparison, the first zone shows the results based on the parameters described in section 2.2 (with mare thickness, H_{DeHon}; cessation time of mare filling, t_{end}; peak time of mare filling, 3.8 Ga). The second, third and fourth zone show the results for other values of mare thickness, cessation and peak time of mare filling, respectively (the parameters are summarized in the Table 8). The schematics above the grey zones illustrate the differences of the studied parameters. The non-mare distribution is shown as box-and-whisker plots. The inside red lines are the median value and the upper and lower boundaries of the boxes are the first and third quantile. The ends of the whiskers represent 99% of data. The black dots represent the mean values. 101

Figure 38 Averaged non-mare material abundance in the top 5 m based on multiple simulations. (a) Spatial distribution of the non-mare component. Red stars indicate the location of Apollo (A) and Luna (L) sampling sites. (b) Histogram of the non-mare component abundance in the top 5m by area over the mare regions. The sum of the bars' value is 100%. (c) Average distribution of non-mare component in the top 1 and 5 m with the distance from mare-highland contact. The black curves indicate the average values and the upper and lower bands of the plots (grey zones) are defined by the 95% confidence intervals from the Monte Carlo simulation results. (d) Non-mare material abundance at the Apollo and Luna sampling sites (Bence & Grove, 1978; Rhodes, 1977), and its distribution with the distance from the mare-highland boundary. The grey bars with slashes represent the chemical estimate of the lunar soil samples. The blue diamonds are the median abundance from Y. Huang et al. (2017). The red symbols are the results of this study where the points indicate the mean value. The box-and-whisker plots are presented for the better comparison with Huang et al.'s results, where the inside red lines are the median values and the upper and lower boundaries of the boxes are the first and third quantile. The red triangle and the red inverted triangle are the predicted non-mare fraction at A12 when the very early cessation time of mare filling (0.1 Ga after the basin formation) and when the formation of Copernicus Crater (0.8 Ga, 98 km in diameter) is considered, respectively (all the other parameters are the same as those in section 2.2). 103

Figure 39 The average vertically (a) and laterally (a) transported non-mare material in the top 1, 5, and 10 m over the mare regions when the different value of h_{min} is taken. 110

Figure 40 The spatial distribution of vertically transported non-mare component in the top 1, 5 and 10 m when the different values of h_{min} are taken. 111

Figure 41 The spatial distribution of laterally transported non-mare component in the top 1, 5 and 10 m when the different values of h_{min} are taken. 112

Figure 42 The spatial distributions of non-mare component in the top 5 m when different thickness of mare deposit is taken into account. 113

Figure 43 The spatial distributions of non-mare component in the top 5 m when the different cessation time of the major mare filling is taken into account. 113

Figure 44 The spatial distributions of non-mare component in the top 5 m when the younger peak time of mare eruption (3.3 Ga) is taken into account. 114
Figure 45 The difference of relative melt distribution of the near-surface compared with the result of Figure 24c when (a) the exponent of melt thickness distribution is typical value, but the exponent of ejecta thickness distribution is taken to be -2.5 (blue dots) and -3.5 (red dots); (b) the exponent of ejecta thickness distribution is typical value, but the exponent of melt thickness distribution is taken to be -1.8 (blue dots) and -2.2 (red dots). 116
Figure 46 Key results and outlook of this thesis. 117

List of Tables

Table 1 Lunar sample summary. 7

Table 2 Lithology (% of total weight) of Apollo samples 8

Table 3 Constants describing the curves plotted in Figure 11; they are fits of the form: $Vm = cDd$ 23

Table 4 Model age, size, and location of the three basins in simulation. 40

Table 5 Location, size and age of the included basins. 79

Table 6 Abundance of melt from basins in the top one meter, where the total volume of materials including both melt and un-melted component is 3.8×10^4 km^3. 80

Table 7 Abundance of melt with given age interval and its basin-sourced fraction (top one meter) over the Apollo 14-17 and Luna 20 landing region with 50 km in radii from the sampling sites, where the total volume of material both melt and un-melted component is 25 km^3 81

Table 8 Simulations with varying parameters concerning mare fillings. 98

Table 9 The cessation time of the main flooding among different mare regions. 99

Table 10 Non-mare fraction at the sampling sites. 105

Table 11 Statistics of non-mare fraction in the top 5 m when the difference parameters are taken. 114

Contents

1. Motivation 1
2. Introduction 3
2.1. Late-accretion record on the moon 3
2.2. Lunar samples 7
2.3. Impact processes 8
2.3.1. Cratering mechanics 9
2.3.2. Impact melt 12
2.3.3. Interpretations of basin ages 13
2.4. Mare volcanic flooding 15
2.4.1. Total volume and duration 15
2.4.2. Mare/non-mare components in lunar samples 16
3. Methods 18
3.1. Progress of model development 18
3.2. Model specification 20
3.3. Scaling laws 21
3.3.1. Distribution of ejecta thickness 21
3.3.2. Distribution of impact melt 22
4. Research paper I: Lateral diffusion of basin melt 25
4.1. Introduction 26
4.2. Model 27
4.2.1. Model steps 29
4.2.2. Reducing the problem to two dimensions 31
4.3. Results 34
4.3.1. Migration of impact melt 34
4.3.2. Realistic crater size distribution 38
4.3.3. Diffusion of basin melt 39
4.4. Discussion 43
4.4.1. Characteristics of basin melt diffusion 43

4.4.2. Comparison with radiometric dating 45
4.4.3. Other potential factors affecting the melt distribution 48
4.5. Conclusions 50
5. Research paper II: Spatial diffusion of basin melt and its implications for sample interpretation 52
5.1. Introduction 53
5.2. The model 54
5.3. Results 55
5.3.1. Timing of basin-forming events 55
5.3.2. Average melt component in the lunar near-surface layer 57
5.3.3. Present-day distribution of melt from basins formed between 4.2 and 3.8 Ga. 59
5.3.4. Basin-sourced melt abundances at Apollo and Luna sampling sites 61
5.4. Discussion 64
5.4.1. Implications for the interpretation of melt provenance at lunar landing sites .. 64
5.4.2. Implications for future basin-melt targeted sampling 66
5.4.3. Effects on model results of varying input parameters 67
5.4.4. Other notable uncertainties in the model's prediction of the distribution of basin melt 68
5.5. Conclusion 70
5.6. Supplementary material 71
5.6.1. Essence of the model 71
5.6.2. Characteristics of impact gardening 73
5.6.3. Filtering out inconsequential impact events 75
5.6.4. Effects on model results of varying input parameters 77
6. Research paper III: Evaluation of the non-mare component of mare soils 84
6.1. Introduction 86
6.1.1. Non-mare component in the lunar mare soil samples 86
6.1.2. Mare volcanic flooding 87
6.2. Model 89
6.2.1. Ejecta distribution 90

6.2.2. Mare volcanic filling 91
6.3. Results basin filling 95
6.3.1. Mixing of the laterally transported non-mare component 95
6.3.2. Mixing of vertically transported component 95
6.4. Continuous basin filling 96
6.4.1. Diffusion features of non-mare material 96
6.4.2. Magnitude of lateral versus vertical mixing 97
6.4.3. Varying parameters concerning mare filling 98
6.5. Spatial distribution of non-mare component 101
6.5.1. Overall features 101
6.5.2. Distribution with the distance from the mare-highland boundary 103
6.6. Non-mare concentration at sampling sites 104
6.7. Conclusions 108
6.8. Supplementary material 109
6.8.1. Effect of the different choice of h_{min} 109
6.8.2. Simulations results with the varying parameters concerning mare filling 112
7. Discussion 115
7.1. Sensitivity to the uncertainty in scaling laws 115
7.2. Key findings 116
7.3. Outlook 118
7.3.1. Refinements of the model 118
7.3.2. Application of the model 119
7.3.3. More constrains of radioisotopic data 120
8. Synthesis 122
9. Bibliography 123

1. Motivation

The Moon is the only body in space that has been directly sampled. These samples provide radioisotope ages which are able to pinpoint ancient impact events and thus establish some fixed time points in lunar bombardment history. However, the long-time impact cratering has occurred on the Moon. A great number of impact events repeatedly disrupted the surface, fragmenting the surface material, altering its composition, and redistributing it. The effect of such continual impact cratering is referred to as impact gardening in this thesis. The top kilometers of the lunar crust were fragmented by numerous large impacts that occurred during the early bombardment history. This chaotically mixed layer is termed megaregolith. The long-time impact gardening has mixed the material of different components resulting in the complicated composition of surface material. It makes the interpretation of the origin of the returned lunar samples uncertain since it is difficult to link any specific component to a particular impact event. This uncertainty hinders a deeper understanding of lunar bombardment history.

To trace back the origin of the surface material and thus to link its different components to particular impact events, this thesis aims to investigate the evolving distribution of surface material under continual impact mixing. An innovative approach (model) is developed to trace the dispersal of surface material which can quantitatively check the interpretations of the proposed origin of the returned samples. Different components of interest can be traced using this model. This thesis focuses on two major groups of components contained in the samples: impact melt/unheated (Papers I and II) and mare/non-mare material (Paper III).

Impact melts are the material heated to high temperatures caused by high-velocity impact events. The occurrence time of the impact event is recorded in the melt by resetting a radioisotopic system of low closure temperature. The differently-aged impact melts are, therefore, the key to tracing back the bombardment history. The estimate of melt distribution at the landing sites can help to interpret the origin of impact melts in the returned samples.

Most of the Apollo landing sites where samples were taken were located within mare regions. In the mare samples, it has been found to be dominant with the mare component but mixed with a significant amount of non-mare materials. The source of the also-present non-mare material is important to understand since it tells us the mechanism of material exchange between lunar mare and highland regions.

In view of the issues that hinder the sample interpenetrations most, this thesis addresses the following key questions:

Impact melt/unheated material: How is impact melt with different ages distributed on the lunar surface? What abundance of basin melt is identifiable at the surface and how much

of it is expected to be found in the collected lunar samples? How did late-forming impact basins bias the melt composition? Where could be fruitful locations to collect basin melts of interest?

Mare/non-mare material: What is the origin of the abundant "exotic" non-mare component found in the collected mare samples? Was it laterally transported from the distant highland region? Or was it vertically excavated from depth (underlying stratum)? What is the relative importance of vertical versus lateral mass transport on the Moon? How much "exotic" component can be expected over the regions that have not been sampled?

In order to answer these questions, the following steps are necessary:

(1) **Develop a numerical model to trace the evolving distribution of different components with the cumulative effects of impact gardening**: Using this model, both the lateral dispersal and mixing processes with depth are recorded, and hence the evolving features of material in different dimensions can be analyzed. This model is designed to be capable of investigating different target components.

(2) **Analyze the evolving distribution of impact melts**: For each impact event, the generation of impact melt is investigated including both the total volume and the distribution in the ejecta. This is the key to simulate the production of melts with different ages and of their re-melting history. Melts with different basin origins are traced from their formation to the present. It makes it possible to finally estimate the composition of the melt components at the different sampling sites. By comparing the model-predicted results with the distribution of radioisotopic ages of the collected samples, impact melt that is likely derived from basin-forming events could be inferred (i.e., the origin of the impact melts in the samples can be better understood).

(3) **Trace the diffusion of the mare and non-mare components:** Vertically- and laterally-transported components are recorded separately. Therefore, diffusion features of both components can be delineated, and their relative efficiencies can be compared. The average fraction of components with different origins over the mare surface and at the sampling sites can then be estimated. By comparing the calculated composition with that of the samples, geologic processes that may have disturbed the composition at the sampling sites could be further inferred.

2. Introduction

2.1. Late-accretion record on the moon

The terrestrial planets are thought to have formed by collisions among planetesimals (the fast accumulation of dust in the solar protoplanetary disk) which led to the formation of Moon- to Mars-sized planetary embryos. These embryos themselves collided to form the final four terrestrial planets (see review in Morbidelli, Lunine, et al., 2012). As for Earth, one of these collisions resulted in the formation of the Moon. The matter which was molten and partly vaporized during this collision was ejected into Earth orbit where it accumulated to form the Moon. There is a general consensus that the Moon-forming impact was the last major event in Earth's accretion, essentially defining the end of terrestrial planet formation (Canup & Asphaug, 2001). Therefore, the late growth history of the terrestrial planets includes the terminal giant impacts, culminating in the formation of the Earth's Moon, and the subsequent bombardment with leftover planetesimals. The latter is commonly termed as 'late accretion'. Understanding the late accretion history of the terrestrial planets is critical for understanding the geologic evolution of planetary surfaces.

Geological activity on the Earth has erased most evidence of the late accretion. On the Moon, there is no wind, atmosphere, water, nor life. In addition, the lunar surface has not been shaped by recent geological activity, because of its relatively cold and rigid crust (Hörz et al. 1991). The record of ancient bombardment on the Moon has thus been well-preserved until the present day, making it the best object to study the ancient accretion history. The traces of large-scale impact events that produced the giant basins are important clues to understanding the lunar formation history:

The stratigraphic system: The formation of some lunar basins has been used to establish a stratigraphic system for the Moon. The relative stratigraphic system is based on the deposition sequence of the ejecta blankets of large basins and craters. The most widely accepted system was developed by Wilhelms (1987), who divided the lunar history into five periods: the pre-Nectarian (oldest), Nectarian, Imbrian, Eratosthenian, and the Copernican System (youngest). Each period's base is defined by the impact event it is named after.

The age of impact craters is recorded in their generated melt. In order to derive an absolute lunar stratigraphy, it is crucial to properly link impact melts contained in the samples to these specific impact events, that is, to find the correct interpretation of which sample represents the actual timing of an impact cratering event. Because of the diverse interpretations and difficulties of linking measured ages of samples to specific key lunar impact events, there remains uncertainty in the chronostratigraphic systems (e.g., Baldwin 1987; Maurer et al. 1978; Neukum 1983; Wilhelms 1987).

The chronology system: Crater statistics models give fundamental insights into the collisional dynamics of the solar system by expressing both the mass frequency and time-integrated flux of impacting objects. It has been shown that lunar crater distributions conform to a continuous curve, the lunar production function (PF). A pervasive PF to describe the cumulative size-frequency distribution (SFD) of lunar craters was proposed by Neukum (Neukum, 1983; Neukum & Ivanov, 1994). It is an eleventh-degree polynomial fit to the cumulative number of craters (Figure 1 a): $\log_{10}(N) = a_0 + \sum_{n=1}^{11} a_n[\log_{10}(D)]^n$, where D is crater diameter in km, N is the number of craters with diameters $>D$ per km^2 per Ga; a_n are constant coefficients.

In order to establish the cratering chronology system (i.e., crater production rates through geologic time), one has to link the radiometric ages from the returned Apollo and Luna samples to crater counts of the surfaces where the samples originated (e.g., Neukum, 1983; Neukum & Ivanov, 1994; Stöffler & Ryder, 2001). For this purpose, crater counts associated with the Apollo 11, 12, 14, 15, 16, 17, and the Luna 16 and 24 landing sites were performed and correlated with the corresponding radiometric ages of these sites (e.g., Neukum, 1983; Strom and Neukum, 1988; Neukum and Ivanov, 1994; Stöffler and Ryder, 2001). The empirical chronology derived from Neukum and Ivanov (1994) and Neukum et al. (2001) is:

$$N_{\mathrm{cum}}(D \geq 1\,\mathrm{km}) = 5.44 \times 10^{-14}[\exp(6.93 \times t) - 1] + 8.38 \times 10^{-4}t.$$

It relates the number of craters ≥1 km in diameter per km^2 in an area with the crater accumulation time t in Ga (Figure 1b). However, it is an estimate with the first-order accuracy. Because the linkage of lunar sample ages to particular basin-forming events is still subject to discussion (Neukum & Ivanov, 1994; Spudis, 1993; Stöffler & Ryder, 2001; Wilhelms, 1987) the diverse interpretations of the measured isotopic ages of the returned samples have led to several more or less different chronologies (Hartmann et al., 2007; Le Feuvre & Wieczorek, 2011; Neukum, 1983).

Heavy bombardment history: Because there were many more planetesimals available to be swept up than there are now, it is currently believed that after the solidification of the lunar crust, the early moon was struck by a large number of meteorites and asteroids. This early impact history is termed “heavy bombardment” (see the review in Bottke & Norman, 2017). The knowledge of the period of heavy bombardment has significant implications for understanding planetary dynamics. It may have been linked to the late migration of the giant planets accompanied by a scattering of comets and asteroids from stable reservoirs (Tsiganis et al., 2005). However, the exact timing of the early bombardment remains unclear. Critical to study this period of history is to identify how many discrete impact events are represented in the age distribution of lunar melt rocks, and whether these events can be linked to specific lunar basins. The lack of a clear geological relationship between individual samples and impact

structures has hampered the interpretation of discrete events (Bottke & Norman, 2017; Haskin, 1998; Haskin et al., 1998; Norman et al., 2010).

There is a particularly intense debate over two possible scenarios. One is the classic "tail end" accretion related to the described chronology function. As seen from Figure 1 c, the impact rate calculated based on the time-derivative of the chronology function suggests that the bombardment declined monotonically since the formation of the Moon (Neukum et al., 2001; Neukum & Ivanov, 1994). Another is the "terminal cataclysm" scenario. It was first raised by Tera and co-workers. The existence of 4.5 Ga old "genesis rocks" had been predicted during preparations for Apollo missions. However, many lunar samples showed clustered ages of ~3.9 Ga, with a paucity before ~4.0 Ga (Tera et al., 1974). This was interpreted to be a late, heavy, inner-solar-system bombardment, ~3.9 Ga ago when many of the lunar multi-ring impact basins were created within intervals of ~150–200 Ma (Figure 1c). The "terminal cataclysm" scenario has been questioned in recent years, and the clustered isotopic ages are suggested to be related to the significant mixing of Imbrium ejecta of this age (Hartmann, 2003; Michael et al., 2018; Schaeffer & Schaeffer, 1977). To estimate the degree of the mixing of basins' ejecta, a more systematic study of the diffusion of basin melt is required to constrain the quantitative melt composition at these sampling sites.

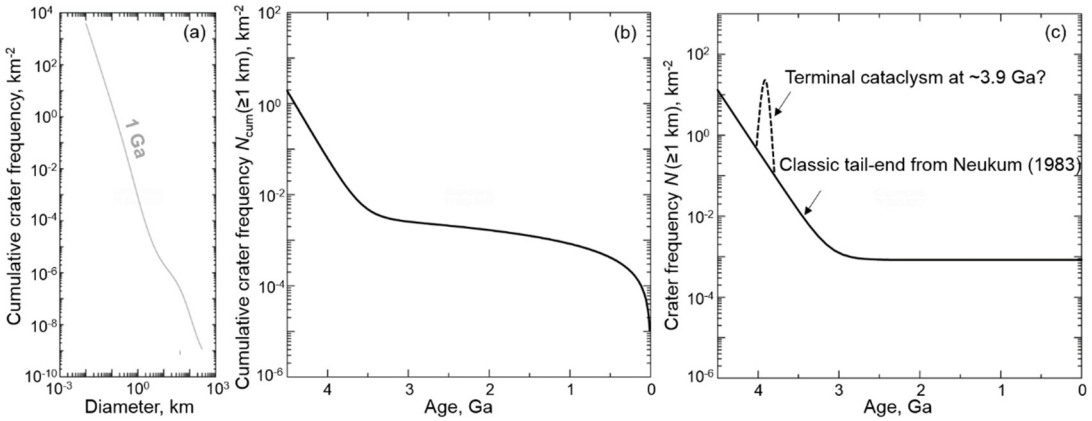

Figure 1 Lunar impact history. (a) Lunar production function (Neukum, 1983). (b) Lunar chronology function (Neukum, 1983). (c) Impact rate showing two debating scenarios of the early bombardment history (Bottke & Norman, 2017).

Aside from the highly debated scenarios of "tail end" and "terminal cataclysm", other opinions on the lunar impact flux have been raised as well (see the review in Zellner, 2017). In order to explain the saturated crater record in the lunar highlands, some investigators (Neukum et al., 1975; Tera et al., 1974), proposed that the Moon must have experienced some impacts prior to 3.85 Ga. Thus, an early intense bombardment may have occurred. In recent studies, Morbidelli, Marchi, et al. (2012) suggest that a "sawtooth pattern" can explain today's absence of asteroids in the E-Belt, which was disrupted as the gas giant planets migrated through resonances to their

current locations. The proposed various scenarios of the early bombardment history are summarized in Figure 2. It indicates that the early bombardment history still requires further study.

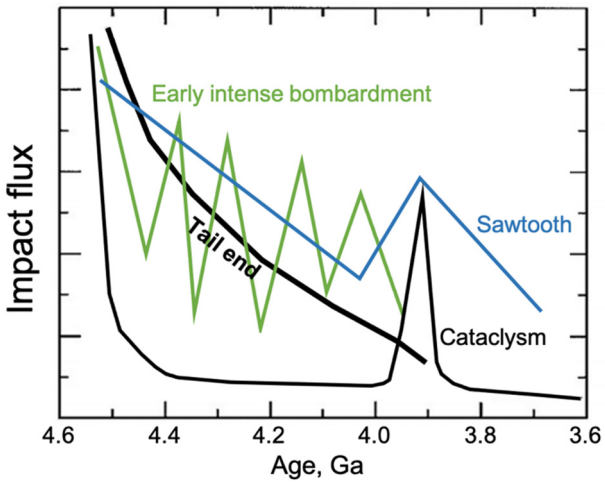

Figure 2 Summary of proposed various opinions on lunar impact flux (after Zellner, 2017).

2.2. Lunar samples

Among all terrestrial bodies, the Moon is the only one that has been systematically sampled. The lunar rocks available for detailed analysis include the meteorites that were found on Earth and the samples that were collected during the lunar exploration missions. They provide ground-truth references for numerous geologic investigations and experiments and are used for calibration of remote sensing data of the Moon (see the summary of lunar samples in Vaniman et al., 1991).

Six manned U.S. Apollo (1969–1972) and three automated U.S.S.R. Luna missions (1970–1976) brought samples from the lunar surface. Table 1 summarizes the landing times and locations of these missions. During the Apollo missions, 381.7 kg of samples were collected which far outweigh the 0.3 kg returned by the Luna robots, but Luna 16, 20, and 24 provided important new sample types from areas that were not visited by Apollo missions.

Table 1 Lunar sample summary.

Mission	Country	Landing time	Sample returned	Location
Apollo 11	U.S.	July 20, 1969	21.6 kg	Mare Tranquillitatis (0.674° N, 23.472° E)
Apollo 12		November 19, 1969	34.3 kg	Oceanus Procellarum (3.012° S, 23.422° W)
Apollo 14		February 5, 1971	42.3 kg	Fra Mauro (3.645° S, 17.471° W)
Apollo 15		July 30, 1971	77.3 kg	Hadley/Apennines (26.132° N, 3.634° E)
Apollo 16		April 20, 1972	95.7 kg	Descartes (8.973° S, 15.498° E)
Apollo 17		December 11, 1972	110.5 kg	Taurus-Littrow (20.191° N, 30.772° E)
Luna 16	U.S.S.R.	September 20, 1970	101 g	Mare Fecunditatis (0.683°S, 56.300°E)
Luna 20		February 21, 1972	30 g	Terra Apollonius (3.533°'N, 56.55°E)
Luna 24		August 18, 1976	170 g	Mare Crisium (12.714°N, 62.213°E)

The lithology of the Apollo samples with different grain sizes is presented in Table 2. The weight percentage of fine materials with grain sizes smaller than 10 mm among the total samples ranges from 17.0% to 54.6%, with an average percentage of 24.0%. Rocks with sizes larger than 10 cm constitute more than half of all the sample mass. Mare basalt is predominant (44–97%) in the samples collected from mare regions (Apollo 11, 12, 15, and 17). Samples

collected from highland regions (Apollo 14 and 16) also contain some mare basalt, but the weight fraction is smaller than 15%. In addition, impact cratering as a major geologic process on the Moon produced a certain amount of impact melt, samples of which account for about 10% of the total Apollo collections.

Table 2 Lithology (% of total weight) of Apollo samples

Missions**	Apollo 11	Apollo 12	*Apollo 14*	Apollo 15	*Apollo 16*	Apollo 17	Apollo total
Fines (<10 mm)	54.6	16.8	30.6	17.0	19.3	26.7	24.0
Rocks (>10 cm)	44.9	80.6	67.3	74.7	72.3	65.9	69.5
Impact melt*				(3.1)	(34.6)		(9.4)
Basalt*	(44.3)	(97.4)	(13.5)	(50.7)		(44.2)	(36.4)
others	0.5	2.6	2.1	8.3	8.4	7.4	6.5

* Numbers in parentheses represent percentages within a group.

** Missions located on the highlands are shown in italics.

Another source of lunar samples is lunar meteorites, which are solid pieces of debris launched from the Moon by large-scale impacts. Chemical studies have supported their lunar origin, where slight compositional differences indicate that they come from locations other than the nine sites sampled by the Apollo and Luna missions. Therefore, the lunar meteorites also provide information about the areas not sampled by the Apollo and Luna missions. In addition, impact events occur on the Moon randomly, and hence the launch locations of lunar meteorites represent localities randomly distributed over the lunar surface, being free from any sampling bias. As of August 2017, about 306 lunar meteorites have been discovered, perhaps representing more than 30 separate meteorite falls (i.e., many of the stones are paired fragments of the same meteoroid). The total mass is more than 190 kg. Most of the lunar meteorites are feldspathic regolith breccias or impact-melt breccias (Lucey et al., 2006).

2.3. Impact processes

Based on the albedo of surface material, the lunar surface is roughly divided into two major parts: darker mare areas and lighter highland areas. The maria are mostly composed of volcanic basalts, which are formed from rapid cooling and crystallization of molten rock from massive lava flows. They represent the products of mantle melting and therefore give insight into the nature, location, and evolution of interior melting, and the thermal evolution of the Moon (Head, 2001). The highlands are representative of the ancient lunar crust and have not been affected by volcanic flooding (Vaniman et al., 1991).

2.3.1. Cratering mechanics

The impacting bodies that enter the Earth/Moon system are derived from the asteroid belt and comets from the out solar system with a mass ranging over 35 orders of magnitude, from microscopic dust particles to huge (~10^{20} g) asteroids. The bodies possess high kinetic energy with a common velocity of ~15-20 km/sec and ~18 km/sec on average (Hörz et al., 1991). Upon impact, the high kinetic energy is converted into shock waves radiating from the impact point into the target and backward into the projectile. As the shock waves expand, they interact with the original target surface and set a large volume of target rock into motion, excavating the target and forming a transient impact crater. The formation process of an impact crater is complex and continuous. For convenience, it is usually divided into three distinct stages: contact/compression, excavation, and modification (the more detail is described in French, 1998; Gault et al., 1968; Melosh, 1989).

The contact/compression stage begins at the instant that the leading edge of the moving projectile contacts with the target surface (Figure 3a). The shock waves are transmitted into the target rocks losing energy rapidly as they travel away from the impact point (Figure 3b). The brief contact/compression stage (no more than a few seconds) grades immediately into a longer excavation stage (Figure 3c), during which the target rock is driven outward from the impact point as a consequence of the non-isentropic shock wave compression and subsequent release setting material into motion. The excavation stage results in a bowl-shaped depression with a structurally uplifted rim, which is called the transient crater (Figure 3d). The material ejected from the cavity forms an ejecta curtain. Then, the modification stage (Figure 3e) begins, during which the transient crater is modified by gravity. The majority of the ejected material deposits near the crater, forming ejecta blankets.

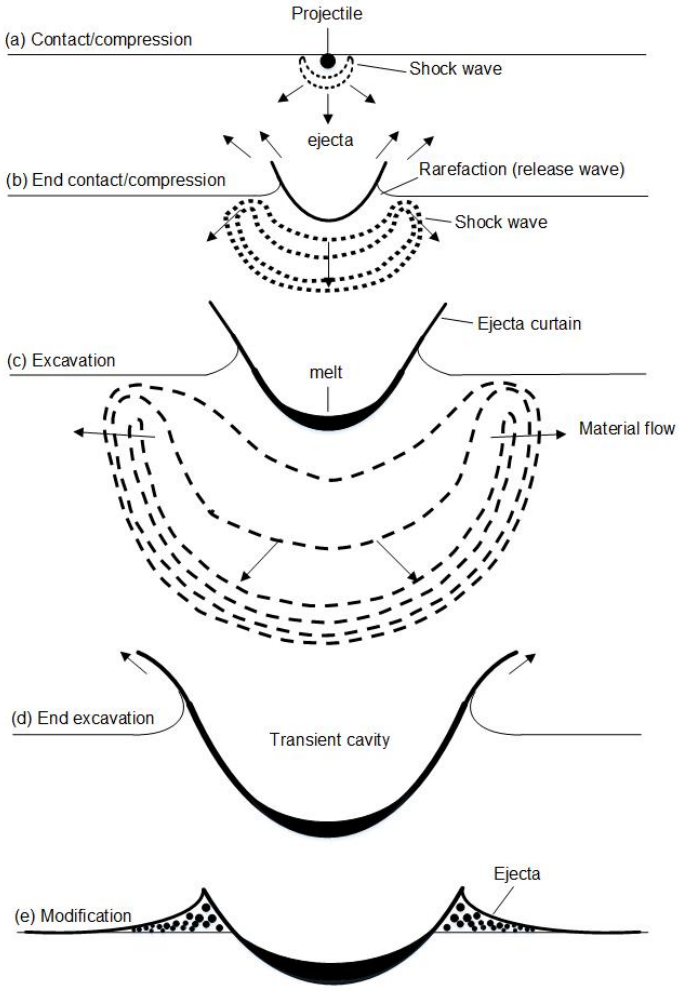

Figure 3 Series of cross-section diagrams showing progressive development of a small, bowl-shaped simple impact structure (after French 1998): (a) contact/compression stage; (b) start of excavation stage; (c) middle of excavation stage; (d) end of excavation stage; (e) start of modification stage. The generated high temperature melts part of the target material which is shown in black in (c)-(e).

The material ejected from crater cavities containing different components, such as impact melt and mare/non-mare material, displays various forms (McGetchin et al., 1973; Melosh, 1989). The ejecta deposit is thickest at the crater rim and gets thinner with increasing distance. Where the deposit is recognizably continuous near the crater rim is called the ejecta blanket. Ejecta beyond the ejecta blanket that is ~1-2 radius from crater center deposit discontinuously. At greater ranges, ejecta deposit becomes patchy, being marked with bright ejecta rays and secondary craters. As an example, Figure 4 presents a small, Copernican-aged crater on the Moon. The crater is young, and hence the features of the ejecta deposit, including the ejecta blanket, the discontinuous deposit, and ejecta rays, remain distinct.

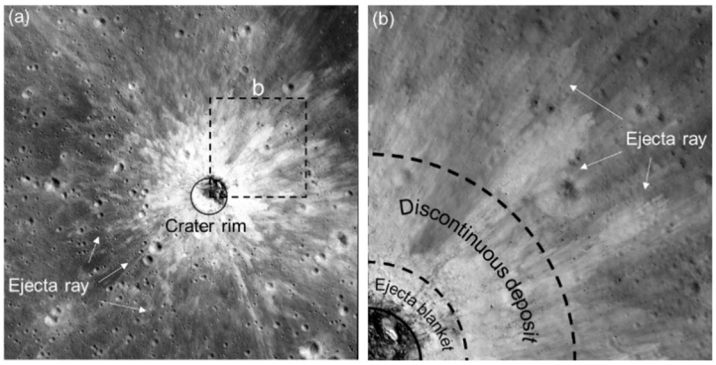

Figure 4 An example of impact ejecta on the Moon. (a) A small Copernican-aged crater (25.876°S, 136.081°E; ~270 m in diameter). The ejecta including continuous deposits (ejecta blanket), discontinuous deposits, and rays display high reflectance. (b) An enlarged view of the area outlined by the dashed square in (a).

The examination of the morphology of impact craters in different sizes shows that impact structures become more complex with increasing size (Hiesinger & Head, 2006), changing from bowl-shaped simple craters (e.g., Figure 3; Figure 5a) to craters with central peaks to basins with two or more rings (e.g., Figure 5b). The transition from simple to complex takes place on the Moon is 21 km (Pike, 1977). Craters larger than 300 km in diameter are more complex and are termed impact basins (e.g., Figure 5c). The projectiles forming lunar basins were rather large and the largest one which resulted in South Pole-Aitken basin (~2500 km diameter) was up to ~200 km in diameter (Wieczorek et al., 2012). These basins formed in the early formation history of the Moon and control much of the Moon's geology. For example, mare basalts are mainly confined in the topographic depressions of these basins' centers.

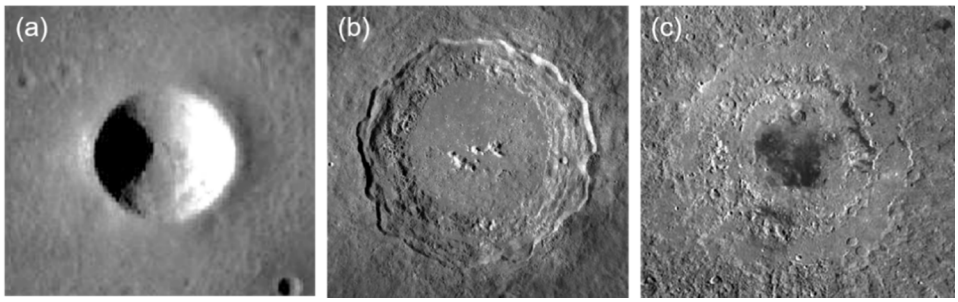

Figure 5 Different morphology of impact craters on the Moon. (a) Simple crater (Moltke, D = 6 m). (b) Central peak crater (Copernicus, D = 96 km). (c) Multi rim basin (Orientale basin, D = 327 km). D is the diameter of craters.

About 40 lunar basins have been recognized and a greater number, probably up to 90, was proposed (Fassett et al., 2012; Frey, 2011; Neumann et al., 2015; Wilhelms, 1987). The ejecta of basins is widely distributed which is an important marker in analyzing the geologic history of the Moon. Based on superposition relationships (younger craters form on top of older structures), a relative time sequence of the lunar basins has been constructed, and a good

overview of the Moon's geologic history has been established (see section 2.1 for further description).

2.3.2. Impact melt

A common shock-metamorphosed product of an impact event is impact melt. It is a homogenized mixture of the target lithologies and the compositions. Textural characteristics distinguish them from conventional igneous rocks (see a summary of melt features in French, 1998).

Impact-generated shock waves deposit some of their original energy as heat within the target rocks. Near the impact point, the thermal energy is sufficient to produce temperatures higher than the normal melting points of the target rocks and their constituent minerals. Therefore, when the shock wave has passed and the pressure returns to normal, spontaneous melting occurs almost instantaneously throughout a large volume of target rock. The shock waves also provide kinetic energy to accelerate the newly formed melt spreading it both within and outside the crater as small bodies of glass in breccias and as larger bodies of crystalline igneous rock of varying size, shape, and appearance (Cintala & Grieve, 1998; Dence et al., 1971; Grieve & Cintala, 1992). As an example, Figure 6 presents a giant swirl of impact melt to the west of the young crater Giordano Bruno.

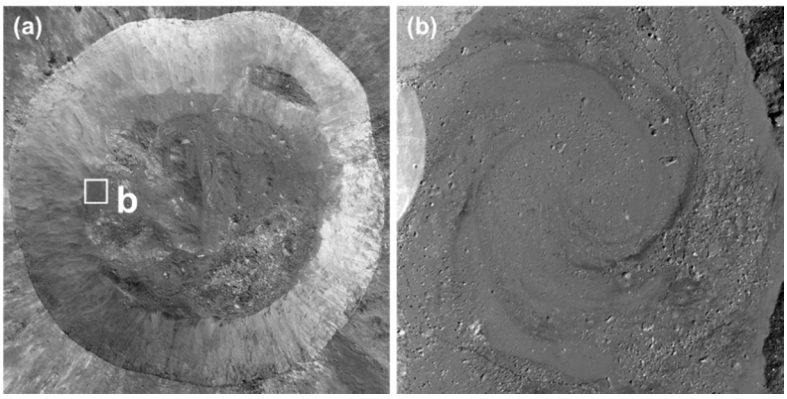

Figure 6 An example of impact melt pool on the Moon: The young crater Giordano Bruno (a; 21 km diameter) and a giant swirl of impact melt on the west of the crater floor (b) (Image credit: NASA/GSFC/ASU).

Impact melting that produces homogeneous rock, minerals, and glass, has reset isotopic clocks of a target material, allowing, in principle, unambiguous dating of impact events. Many decay systems are available for impact dating, such as Rb-Sr, K-Ar, Sm-Nd, and U-Pb. Since gases can be removed much more easily from minerals and rocks than solid nuclei, isotopic systems with gaseous daughter products are particularly sensitive to disturbances. Therefore, the K-Ar system and its associated ^{39}Ar-^{40}Ar dating technique are frequently used for impact dating (Flude et al., 2014; Jourdan et al., 2014; McDougall & Harrison, 1999; Wartho et al., 2014).

The K-Ar technique is the conventional approach to find the age of impact melt. It depends on the radioactive decay of isotopic potassium, ^{40}K, the half-life of which is more than a billion years, and thus it is possible to date the melt of impacts that happened billions of years ago. Over time, the radioactive isotope of potassium, ^{40}K, decays to an isotope of argon, ^{40}Ar. Argon is a noble gas and does not bond chemically to the minerals. In addition, argon is a large atom and cannot easily escape from a rock. So ^{40}Ar builds up, and any found inside a rock is very likely the result of radioactive decay of ^{40}K. If the rock is melted, the argon can escape. Thus, the dates obtained are related to the last heating of the rock, which is taken to have been caused only by impact in this thesis. Thus the absolute time of an impact is obtained (Flude et al., 2014; Jourdan et al., 2014; McDougall & Harrison, 1999; Wartho et al., 2014).

The decay of ^{40}K has multiple pathways. This information is typically expressed in terms of the decay constants. The constant of decay to ^{40}Ca, λ_β, is 4.962×10^{-10} a^{-1}; the constant of decay to ^{40}Ar, λ_{EC}, is 0.581×10^{-10} a^{-1}. The total decay constant (λ_{total}) is the sum of λ_β and λ_{EC}. By measuring the amount of ^{40}Ar in a rock, and the amount of ^{40}K which was available to produce it, one can calculate how long the ^{40}Ar has been building up, that is, the age of the impact melt:

$$t = \frac{1}{\lambda_{total}} \ln\left(\frac{\lambda_{total}}{\lambda_{EC}} \frac{^{40}\mathrm{Ar}}{^{40}\mathrm{K}} + 1\right)$$

where ^{40}Ar and ^{40}K are the measured amounts of ^{40}Ar and ^{40}K.

The conventional K-Ar dating process is technically difficult. It is usually carried out by analyzing potassium in one part of the sample and measuring argon in another part. The ^{39}Ar-^{40}Ar method can be done on the same small piece of a sample, analyzing for both gases in a mass spectrometer, and is more commonly applied to date the age of impact melt recently. This technique depends upon the fact that the ^{39}K can be bombarded with neutrons in a nuclear reactor to produce an amount of ^{39}Ar which is proportional to the potassium content of the sample. The age can be calculated by:

$$t = \frac{1}{\lambda_{total}} \ln\left(\mathrm{J} \frac{^{40}\mathrm{Ar}}{^{39}\mathrm{Ar}} + 1\right)$$

where the proportionality factor J is the neutron flux constant.

2.3.3. Interpretations of basin ages

Radioisotopic ages of impact melts have been determined on numerous lunar rocks collected at the Apollo and Luna landing sites. However, because of our inability to definitively link lunar samples with specific craters, especially the giant basins, the interpretation of the radioisotopic ages is still uncertain (Bottke & Norman, 2017; Stöffler, 2006).

The nearside of the Moon was extensively resurfaced by Imbrium ejecta, which would have significantly altered the composition of surface material at the sampling sites. This makes the interpretations of samples' origin complicated and the raised debate is still on-going. For example, Apollo 14 landed on hilly terrain, the Fra Mauro formation. The regional physiographic characteristics relate its formation to the Imbrium ejecta, but it is difficult to convincingly distinguish primary Imbrium ejecta from products of local smaller craters. Even more challenging is the interpretation of the Apollo 16 samples. The origin of Descartes Hills, one of the mission targets, is contentious. Based on remote sensing data and the samples collected from the rim of North Ray crater, the Descartes unit was found to consist predominantly of shock-lithified breccias with highly aluminous compositions and low concentrations of incompatible trace elements, which are more consistent with a derivation from the feldspathic crust surrounding the Nectaris basin rather than from the Procellarum-KREEP Terrain in which Imbrium is located. The subsequent detailed study of the Descartes breccias, however, showed that some lithic fragments are petrographically similar to basalt collected at the Apollo 14 landing site, appearing to have a more genetic relationship to Imbrium rather than Nectaris (Bottke & Norman, 2017).

Although radioisotopic ages with smaller uncertainty are available, the difficulty to link dated samples to specific impact events significantly hampers our understanding of the Moon. The formation of relatively young basins, such as Serenitatis, Imbrium, and Crisium, that retain clear rim structures on the lunar nearside bias the interpretation of samples most (Stöffler, 2006).

Age of Serenitatis basin: The Apollo 15 and 17 landing sites are close to the main rim of the Serenitatis basin, thus samples from both sites have been taken frequently to date the Serenitatis event. For instance, Apollo 17 samples were collected from massifs of the Taurus-Littrow region, a part of the Serenitatis eastern main rim. Most of the sampled boulders and large rocks are impact-melt breccias. Detailed analysis of the chemical composition provides a tightly constrained age of ~3.89 Ga (Dalrymple & Ryder 1996 and references therein). Isotopic dating of a few smaller fragments from the South Massifs inferred ages ranging between 3.86 and 3.93 Ga (Deutsch & Stöffler, 1987; Jessberger et al., 1977; Wilhelms, 1987). Although the ages appear well constrained to be around 3.9 Ga, it remains open because of the uncertainties in assigning unequivocally these impact melt samples to the Serenitatis event. Sometimes these rocks were even suggested to be derived from the Imbrium event.

Age of Imbrium basin: Apollo 14, 15, and 16 samples are believed to contain a mass of Imbrium ejecta (Spudis, 1993; Wilhelms, 1987). Apollo 14 sampled the continuous ejecta; Apollo 15 sampled on the main rim of the Imbrium basin, and Apollo 16 sampled on distal discontinuous ejecta. Due to the uncertainty of linking those samples to the Imbrium event, its formation time is also debated. There are two major proposals for the age of Imbrium basin. One is mainly

derived from the Apollo 14 samples, where the most frequently measured age of 3.85 Ga was suggested to be derived from Imbrium melt (Ryder, 1994; Spudis, 1993; Wilhelms, 1987). Another younger age of 3.77 Ga was derived from detailed Consortium studies of the Apollo 14 and 16 highland breccia samples based on the youngest radioisotopic ages (Stöffler, 2006).

Age of Crisium basin: The age of the Crisium basin is tentatively inferred from radioisotopic ages of a few collections from the Luna 20 regolith. These samples were collected from the southern ejecta deposits of Crisium basin (Spudis, 1993; Wilhelms, 1987). An age of ~3.9 Ga based on a sample of the KREEP-poor impact melt was proposed to be the formation time of the Crisium basin (Swindle et al., 1991). Similarly, it remains uncertain whether the dated lithic clasts actually represent Crisium melt.

2.4. Mare volcanic flooding

2.4.1. Total volume and duration

Basaltic lavas cover about 17% of the lunar surface and make up ~1% (1×10^7 km^3) of the volume of the lunar crust. Most of these basalts are exposed within the nearside basins and are largely concentrated in the interiors and margins of impact basins being particularly abundant in Nectarian and post-Nectarian age basins such as Nectaris, Humorum, Crisium, Serenitatis, and Imbrium. On the farside, most maria are found in the ancient South Pole-Aitken basin as patches within later craters and basins such as Planck and Apollo (Head, 1976).

A number of approaches have been used to estimate the thickness and the volume of mare deposits. Using a stratigraphic approach and the morphometry of pre-existing impact craters, De Hon and coworkers did a series of studies to determine thicknesses of the nearside maria (De Hon, 1979; De Hon & Waskom, 1976). They suggested that, for most areas, the average basaltic thickness was less than ~400 m, but for some local regions it was in excess of 1-2 km. The use of topographic data from unfilled craters and basins provided additional estimates of mare basalt thickness (Head, 1982), showing that the central parts of unmodified impact basins might contain lenses of basalt up to 6-8 km thick, but that most of the deposits in the basin were generally less than about 2 km thick. Another method to map the thickness of mare basalt is to use radar data. The Apollo Lunar Sounder Experiment (wavelengths between 2 and 60 m) transmitted radar pulses to the Moon and received reflected signals from both the surface and structures beneath the surface. The deepest subsurface interfaces could be the boundaries between the mare and underlying material. Within central Oceanus Procellarum, for example, a thick deposit decreased from ~1 km in the west (near the crater Grimaldi) to ~0.5 km in the east (near the crater Kepler) (Cooper et al., 1994).

Together with the measurements of the surface areas, the estimate of mare thicknesses can be used to constrain the volcanic flux (Head & Wilson, 1992; Hiesinger et al., 2011). Based on the returned lunar samples, the duration of mare volcanism was thought to range from about 3.9 Ga (Apollo 11 samples) to about 3.2 Ga (Apollo 12 samples). A flux with a peak flux prior to 3.5 Ga was proposed (Figure 7a). Using the age of the displaced uppermost mare deposits the peak of flux shifted towards younger ages (3-3.5 Ga) because older deposits were flooded by younger ones (Figure 7b). Later approaches relying on stratigraphic interpretations also yield an asymmetric flux curve but showed the volumetric significance of early mare deposits, displacing the distribution toward earlier times (~3.8 Ga, Figure 7c). Figure 7d displays a flux curve while accounting for probable volcanism in the period of early impact bombardment. Finally, a flux curve based on the combination of different approaches is shown in Figure 7e.

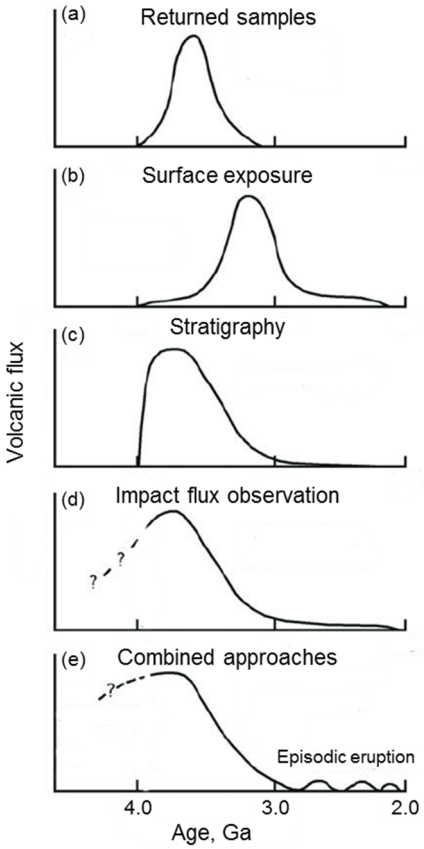

Figure 7 Different approaches to determining extent and flux of mare basalts (after Head and Wilson 1992): returned samples (A), Surface exposure of deposits (B), Stratigraphic assessment of volumes (C), accounting for probable volcanism in the period of early bombardment (D), flux on the basis of combined approaches (E) (after Head & Wilson, 1992; Hiesinger et al., 2011).

2.4.2. Mare/non-mare components in lunar samples

As summarized in Table 1, samples collected from mare regions are dominated by mare basalt, but a certain amount of highland anorthosite (i.e., of non-mare origin) was also found in those collections (Wood, 1970; Wood et al., 1970), especially those of fine soil materials. The average

non-mare abundance is about 20%, with the exception of a few Apollo 12/15/17 samples where the non-mare concentration is up to ~80% (Hubbard et al., 1971; Schonfeld & Meyer, 1972; Wood, 1970). These non-mare components are either laterally transported from the highlands being entrained in the ejecta of impact craters or are vertically excavated from the substrate underlying the surface mare deposit. Figure 8 displays the percentage of non-mare concentration in lunar soil samples and its distribution with the distance from the mare-highland boundary (Rhodes, 1977). The samples of Apollo 15/17, Apollo 12, Apollo 11, and Luna 16 were taken at <4 km, ~20 km, ~50 km, and ~110 km from their nearest mare/highland boundary, respectively. Apollo 15 and 17 sampling sites are close to the mare-highland boundary. Their non-mare abundance displays a trend of rapid decreasing beyond 4 km. This may indicate the low efficiency of lateral transport of material from the highlands so that the found non-mare components are mainly of local origin. However, in the samples collected far away from the mare-highland boundary, such as by Luna 16, the contamination by non-mare components is also significant with a weight fraction of ~0.2. It could be merely of local origin but may also suggest efficient lateral transport.

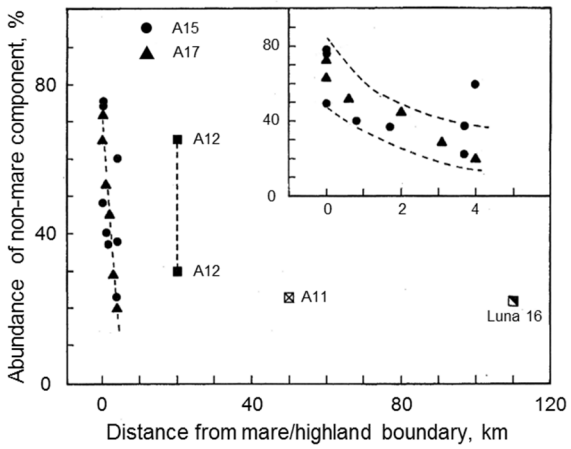

Figure 8 Percentage of chemically estimated non-mare components in lunar soil samples versus distance from a mare-highland boundary. Data for individual sampling stations at the Apollo 15 and 17 landing sites are shown in greater detail in the inset (Rhodes, 1977).

3. Methods

3.1. Progress of model development

Building a spatially-resolved numerical model is a feasible way to investigate the evolving distribution of different components of surface material. However, such a model is complicated.

There are a wide variety of material constituents. Although the returned samples were collected from a spatially limited region of the Moon, there are various rocks (e.g., pristine non-mare rock, breccias, and mare volcanic; Lucey et al., 2006) with multiple mineralogy (e.g., silicate, oxide, and phosphate minerals; Lucey et al., 2006). Even for one type of material, the constituents are complicated. Taking impact melts as an example, impact events occurring at different times produce melt with different ages. For a 100×100 km^2 area, using Neukum chronology function and production function it is calculated to be ~2×10^4 impact events larger than 1 km since 4.5 Ga (Neukum, 1983). If the product of each impact is traced, there would be more than ~2×10^4 different ages of melts. When a global surface and the smaller impact events are taken into account, far more products need to be traced. In addition, impact melt occurs in a variety of forms: small glassy objects around the crater; glassy or crystalline matrices of clast-bearing melt breccias in the crater-fill deposits; larger rocks that occur as sills within the crater-fill deposits. If the various forms of impact melts are traced as well, there would be at least three times more components to simulate.

The spatial distribution of different components is constantly changing with impact mixing. Laterally, each impact event can excavate a certain amount of material with different components and disperse it over a wide area. Some of it could be far away from the impact site. For example, Giordano Bruno is a 22-km lunar impact crater on the lunar far side that occurred <10 Ma ago (Morota et al., 2009). The ejecta ray of this young formation has not been significantly degraded and extends for over 150 km (larger than 10 times crater radii). The material compositions of the region covered by the ejecta would be altered. In the meanwhile, the volume of the disturbed old melt would be reduced by the reheating process of the other impacts. In addition, craters with different sizes do not display the same morphologies and ejecta patterns, so that the affected areas of each impact would not be identical.

It follows that the material components are getting more and more complicated with the occurrence of numerous impact events with respect to types, abundance, and spatial distribution. The model would be rather complicated if all these elements are considered at once. Therefore, in this thesis, the model was built step by step.

The study of Michael et al. (2018) lays the foundation for this thesis. They developed a surface-averaged (1D) model to study the evolution of impact melt with impact gardening. In their

model, all the generated impact melt is assumed to be uniformly deposited on a global surface. Only the statistical distribution of melt was obtained, where the spatial distribution with depth is approximate, and no lateral diffusion is recorded. In this thesis, their 1D model was first extended to two-dimensions (2D) focusing on the lateral diffusion features of surface material. With a better understanding of the material diffusion pattern, a more comprehensive three-dimensional (3D) model has been designed, presenting a more complete picture of the material diffusion over the global surface.

Besides impact gardening, mare volcanic filling also changes the composition of the material at the surface. But mare flooding occurred late, and the majority of the volcanic eruptions ceased before about 3.0 Ga covering only parts of the surface. Therefore, in this thesis, the impact mixing process was considered alone first, and the mare flooding process was involved in the model after the spatially-resolved model was well-developed. As shown in Figure 9, the results of the progressive development of the model have all been published:

Develop a 2D model (Paper I): The 1D model was first extended to 2D by tracing not only the distribution with depth but also the lateral diffusion (Chapter 4). The melt diffusion along the path of a great circle on the Moon is simulated. Considering the affinity with the sampling sites, a great circle passing through three mid- to late-forming lunar basins (Imbrium, Crisium, and Serenitatis) was chosen for modeling. The survival probability of basin melt occurrence at the Apollo and Luna sampling spots was calculated.

Develop a 3D model (Paper II): Then, a 3D model was further developed by extending the 2D model to include the complete lunar surface, where the global distribution of any melt of interest and the melt component at any locations of interest can be obtained (Chapter 5). The calculated melt component was compared with K-Ar ages of the Apollo and Luna samples.

Develop a 3D model with mare volcanic filling process (Paper III): Finally, this 3D model was refined by considering the volcanic eruptions over the lunar mare regions (Chapter 6), where both impact mixing and mare volcanic filling processes were taken into account. It was applied to investigate the diffusion of the non-mare material to help the interpretation of the source of the non-mare component found in mare soil samples.

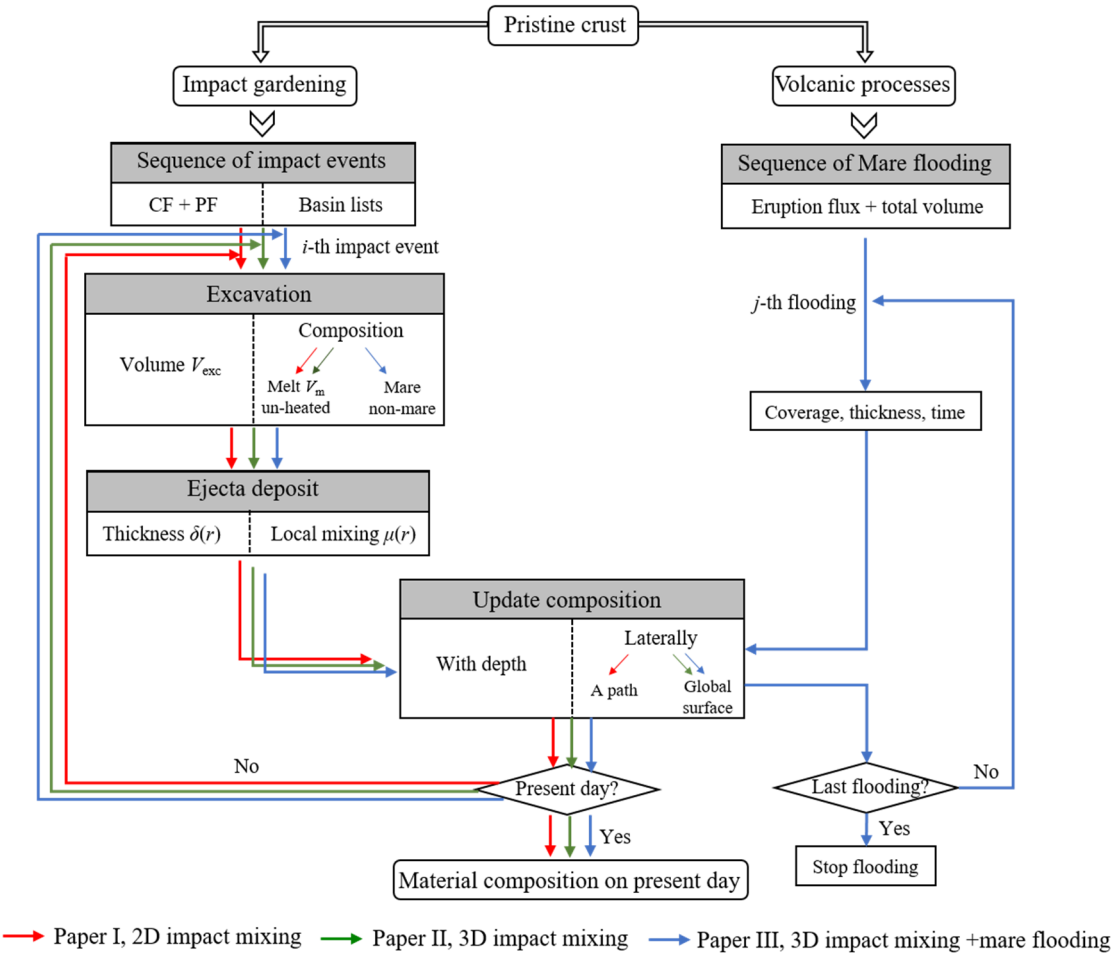

Figure 9 Progress of the model development and the specification of the model.

3.2. Model specification

To build a model tracing the material diffusion with impact mixing, there are three major aspects: the *sequence of impact events*, *impact cratering process, and material redistribution and record of material composition*. The specification of the designed model is shown in Figure 9.

Sequence of impact events: A huge number of impact craters have occurred since the lunar early period. To simulate the bombardment history of the Moon, the statistical distribution of the generated craters should conform to both the lunar chronology function (CF) and production function (PF), based on which impact rate can be calculated. Using the calculated impact rate, the total number of events and sequence of impact events are estimated. The occurrence locations of impacts are spatially random which is simulated using Monte Carlo method. The diameter of the crater formed is generated also using the Monte Carlo method in such a way that the size–frequency distribution statistically conforms to the portion of the PF.

Impact cratering process and material redistribution: For each crater produced, the maximum depth of excavation is calculated as a tenth of the transient crater diameter. The excavated

volume has a torus-like shape, which is estimated to occupy about 1/3 of the volume of a disc of excavation depth in thickness and crater size in diameter.

Record of material composition: The excavated material, together with the specific component, is redistributed after the occurrence of each impact event. The material composition of the affected zones both over the surface and with depth is recorded. After the occurrence of the youngest impact crater, the material composition on present-day is obtained.

Aiming to address various research issues (Paper I, II, and III), the model requires specific improvements. The detail of model essence for each specific research has been presented in all of the corresponding papers. The process of volcanic flooding that had regionally happened on the Moon is considered in the third stage of this study. The volcanic flooding events occur while the formations of cumulative impact gardening. This process will also influence the material composition but over the regional areas.

A complete 3D model has been developed in this thesis, but some parts still require to be improved in the future (see section 7.3 for the more systematic discussions). For example, some scaling laws involved in the model needs further studied (see section 3.3 and the discussion section of each paper), including the ejecta of giant basins and the distribution of impact melt. In addition, impact events smaller than a kilometer have not been taken into account due to their great number, which will also be considered in the future.

3.3. Scaling laws

The size range of impact craters that can be formed in laboratory experiments is limited, but the craters on the Moon show a wide range in size from <mm to hundreds of km. To investigate the craters on the Moon, scaling laws have been devised. They are on the basis of dimensional analysis and can relate initial conditions of an impact (e.g., characteristics of the impactor, the target, the impact velocity) with the properties of the resulting craters. By means of scaling laws, the behavior of small-scale laboratory cratering experiments can be extrapolated to the dimensions of larger craters on the Moon. The relationship between impactor properties and crater size is well-established and addressed in numerous studies using laboratory experiments and numerical modeling (Stöffler, 2006). The simulation of the impact cratering process in this thesis is on the basis of scaling laws. Two important parts of the impact process, the ejecta distribution, and melt production, that are less well-studied and require further discussion are presented in this subsection.

3.3.1. Distribution of ejecta thickness

The ejecta blanket thickness, δ, falls off as a power of the distance r from the crater center: $\delta(r) = f(R)(r/R)^{-3\pm1}$, where R is the radius of the final crater. A traditional description of

the ejecta blanket thickness (McGetchin et al., 1973) $\delta(r) = 0.14R^{0.74}(r/R)^{-3.0}$ is from a compilation of data mainly from explosion experiments. This scaling law was suggested to be applied only to continuous ejecta blankets (beyond about one crater radius, section 2.3). Numerical simulations of impact events, nevertheless, have indicated that the power law distribution of eject thickness can be extrapolated to a greater distance. Using the iSALE-2D Eulerian shock physics code, for example, Luther et al. (2018) did systematical studies on the distribution of the ejecta deposit where varying properties of both impactors and targets were considered. Figure 10 presents the distribution of the ejecta thickness with different impact velocities. The target material is nonporous, cohesionless, and has a coefficient of friction of 0.6. It was found that, within a distance of about ten times the crater radius, the distribution of ejecta thickness still follows a power-law, although the exponent varies (~3±0.5).

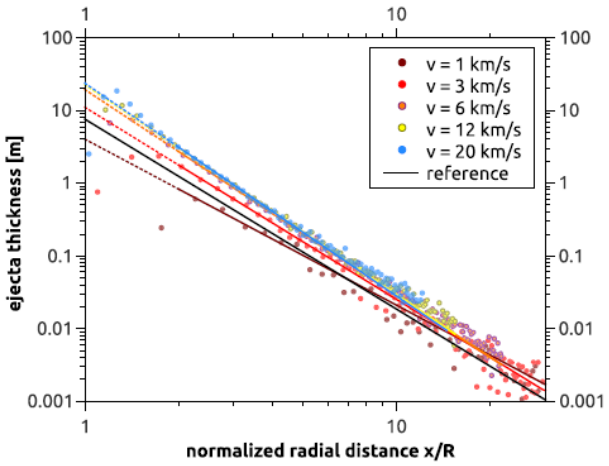

Figure 10 Calculated distribution of the ejecta thickness with different impact velocities using iSALE-2D numerical approach. The target material is nonporous, cohesionless, and has a coefficient of friction of 0.6 (Luther et al., 2018).

3.3.2. Distribution of impact melt

The standard representation of the melt volume V_m in impact craters is $V_m/V_p \sim (V_i^2/E_m)^{\mu}$, where V_p is the projectile volume, v_i is the projectile velocity and E_m is the internal energy of melting, μ is a constant factor (Stöffler, 2006). Cintala and Grieve (1998) employed a modified Murnaghan equation of state for both the target and projectile materials to investigate the volume of the impact melt, where the phase changes were determined by calculating the entropy at each state on the Hugoniot. Their results suggested that the volume of impact melt produced increases exponentially with crater diameter D: $V_m = cD^d$, where c and d are constants determined by a curve-fitting process from the cases of different types of projectiles impacting anorthosite targets in a lunar gravity field (Figure 11). As can be seen from Table 3, the value of c ranges from about 1.0×10^4 to ~2×10^4, and d is equal to 3.85.

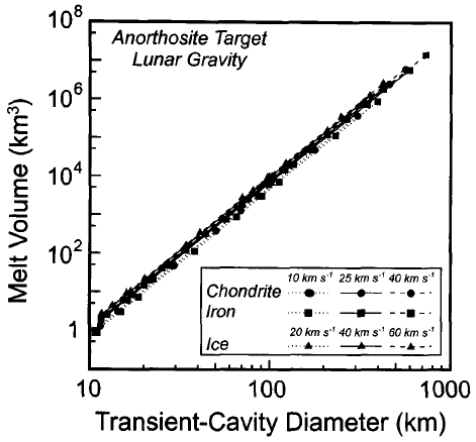

Figure 11 Comparison of melt volumes as a function of transient-cavity diameter where a wide range of projectile types and impact velocities was considered (Cintala & Grieve, 1998).

Table 3 Constants describing the curves plotted in Figure 11; they are fits of the form: $V_m = cD^d$.

	c	**d**
Chondrite		
10 km/s	1.08×10^{-4}	3.85
20 km/s	1.42×10^{-4}	3.85
40 km/s	1.67×10^{-4}	3.85
Iron		
10 km/s	0.91×10^{-4}	3.85
20 km/s	1.23×10^{-4}	3.85
40 km/s	1.46×10^{-4}	3.85
H_2O Ice		
10 km/s	1.55×10^{-4}	3.85
20 km/s	1.88×10^{-4}	3.85
40 km/s	2.08×10^{-4}	3.85

The distribution of impact melt in ejecta has not been well studied so far. In the framework of the TRR170 (see the section of "Structure of the dissertation") the generation, ejection, and deposition of impact melt have been studies by numerical models using the iSALE shock-physics code (pers. comm. Wünnemann et al.): Basalt projectiles with diameters (L) from 2.5 km to 10 km vertically impacting a homogeneous target (same material as projectiles) at various impact velocities (vi) from 12 to 18 km/s were simulated. The preliminary results show that the projectile diameter is the main factor influencing the melt distribution. Figure 12 shows the distribution of ejecta/melt thickness with the distance from the crater rim when various L and vi are considered. Note that impact melt is scattered in the ejecta. The equivalent thickness of impact melt is calculated based on its volume to better compare with the thickness of ejecta. It

can be seen that the thickness of impact melt in ejecta is also distributed following a power-law form: $\delta_m = a_m r^{b2}$. The factor a_m is dependent on the size of the projectiles; the factor b_2 is found to be constant with a value of about -2. These preliminary results were contributed to the first two publications of this thesis (Chapter 4 and Chapter 5).

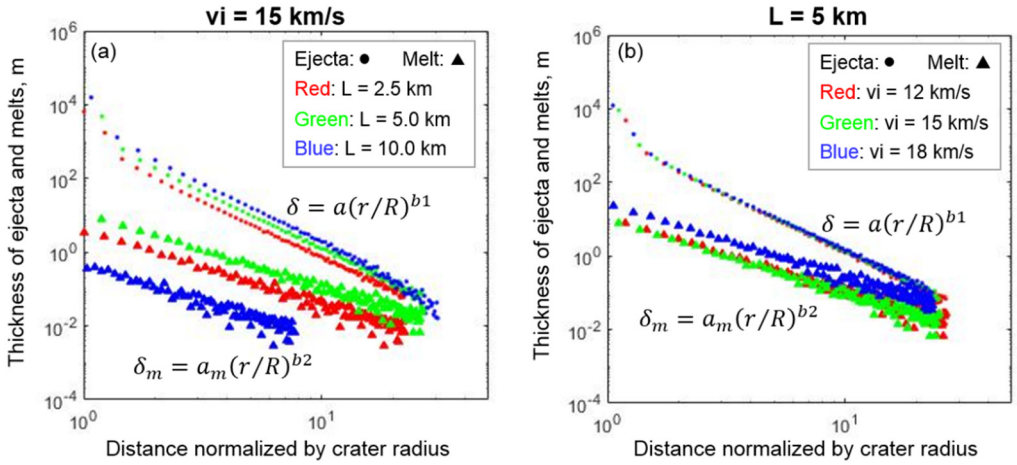

Figure 12 Thickness of ejecta and melt with the distance from crater center based on the simulations with various projectile sizes (a) and impact velocities (b). *vi* and *L* are the impact velocity and diameter of projectiles, respectively.

4. Research paper I: Lateral diffusion of basin melt

The following section has been published as: Tiantian Liu, Greg Michael, Juliane Engelmann, Kai Wünnemann, and Jürgen Oberst (2019), *Regolith mixing by impacts: Lateral diffusion of basin melt*, Icarus, 321, 691–704, doi: https://doi.org/10.1016/j.icarus.2018.12.026. The author contribution is explained in the section of "Structure of the dissertation". This paper presents the results using the 2D-model that is extended from the 1D-model.

Abstract

Impact cratering has been the primary process to alter the distribution of lunar highland material since the formation of a crust. This impact history is recorded in the radiogenic clocks of impact melts which are accessible for study on lunar samples and meteorites. However, primary impact melt is exposed to a long-time gardening process (i.e., re-melting, excavation, burial, and re-excavation) by subsequent impacts resulting in a complex spatial distribution of materials representing specific impact events. To investigate the diffusion behavior of impact melt, a model tracing the evolving distribution of melt laterally and with depth was built using a Monte Carlo approach. Given scaling laws concerning melt production and ejecta distribution, the size-frequency distribution of impact craters, and the rate function for crater formation, we examine the evolution of melt component occurrence of different ages. Three mid- to late-forming basins (Serenitatis, Crisium, and Imbrium) are chosen as a case study for the diffusion of melt from major basin-forming events. The survival probability of basin melt occurrence at the Apollo and Luna sampling spots is derived. It is expected to find abundant Imbrium and Crisium melt at the Apollo and Luna sampling sites, consistent with the K-Ar radiometric dates of highland samples; whereas the older Serenitatis melt was subjected to the later long-term gardening, strongly influenced by later local impacts, and thus is less abundant. Understanding the diffusion of impact melt is helpful for interpretation of radiometric ages of lunar samples and can be used to predict the distribution of differently-aged melts at future landing/sampling sites such as the Chinese Chang'E-4 (CE-4).

Keywords: Moon, surface, Regoliths, Impact processes, Cratering

4.1. Introduction

Impact cratering has been the primary process modifying the lunar surface since the formation of the lunar crust (Hörz et al., 1991). Shock compression generated by impact deposits part of the energy budget as heat in the target rocks during unloading. If the temperature excursion exceeds the normal melting points of the target rocks, the material becomes molten (French, 1998; Melosh, 1989; Stöffler et al., 2017). The subsequent dynamic processes of impact excavation leave the majority of the impact melt distributed along the crater wall, with the remainder being ejected outside the crater in the form of a mixed layer of melted and unheated materials (Melosh, 1989; Osinski & Pierazzo, 2012). The radiometric clocks, e.g. K-Ar, of melted materials are reset leaving a record in the affected rocks (e.g., suevitic impact breccia and melt lens), which can be deciphered by means of isotopic dating techniques from collected lunar samples or meteorites (Flude et al., 2014; McDougall & Harrison, 1999; Wilhelms, 1987). The radiometric dating of impact melt and its association to particular impact events on the Moon is key to our understanding of lunar chronology.

The impact melt emplaced by one event is gardened (i.e., re-melted, excavated, buried, and re-excavated) by later events which alter the original melt distribution both laterally and with depth, as well as diminishing its total presence by reheating. Previous studies, both by analytical and numerical methods, provide various scaling laws to determine the melt production during a single event (e.g., Ahrens & O'Keefe, 1977; Cintala & Grieve, 1998; Maher, 1988; O'Keefe & Ahrens, 1977; Pierazzo et al., 1997; Tonks & Melosh, 1993; Wünnemann et al., 2008). However, the cumulative effect of a long sequence of impacts that produces a megaregolith is complex and not well-studied. Recently, Michael et al. (2018) built a model to investigate such a long sequence of impact gardening using a Monte Carlo approach. The model considered melt abundances in an average sense over the lunar surface, attempting to illustrate the variation in abundance of differently aged melt components with depth. The obtained melt age histogram with several peaks resulting from basin events shows that a cataclysm is not required to reproduce the observations. However, that model was unable to address the variation of abundances with respect to a specific location on the lunar surface, which is the aim of this current work.

Lunar sample radiometric ages combined with their inferred origins tell us the ages of certain lunar terrains. These are essential constraints for diverse models regarding lunar bombardment history - a subject of enduring debate. The classic tail-end crater chronology models, where the impact flux declines exponentially over the first billion years of lunar history, was postulated by comparing the crater density over these terrains (Hartmann, 1970; Neukum, 1983; Neukum et al., 2001; Neukum & Ivanov, 1994). Based on the hypothesized dynamic evolution of the

Solar System or geochemical constrains from lunar samples, various models were proposed, such as cataclysm (Cohen, 2000b; Ryder, 2001; Tera et al., 1974), saw-tooth (Morbidelli, Marchi, et al., 2012; Morbidelli et al., 2018), and the smashing asteroids model (Turner et al., 1973). No matter what method they used, all the model results had to explain the sample ages. Major peaks in the radiometric ages obtained from the lunar samples are believed to be related to the adjacent giant basin-forming events (Haskin et al., 1998; Michael et al., 2018; Ryder et al., 1989), although many have argued that the 3.9 Ga peak is an indicator of a period of late heavy bombardment. The quantitative estimation of the abundance of basin melts and understanding of its gardening processes may be used to invert the observed melt components to gain new constraints on the impact rate function.

In addition, an understanding of the melt gardening process can be applied to estimate the expected abundances of basin melt components at potential sampling/landing sites for future missions. This year's Chinese Chang'E-4 (CE-4) mission will explore the farside of the Moon where no previous missions have landed (J. Huang et al., 2018; Wu et al., 2017). In particular, the South Pole-Aitken (SPA) basin was chosen as the potential landing region. SPA basin is one of the largest impact features in the Solar System and is the oldest observable feature. The probability of finding SPA melt at the potential sampling site can be calculated with an understanding of gardening process.

In section 4.2, we describe how we developed the model to simulate gardening process. We simplified the model to two dimensions (2D) due to the complexity of melt component during the cumulative gardening process. In section 3, the migration of impact melt and the influence of the crater size-frequency distribution (SFD) on melt distribution are presented. Three mid- to late-forming giant basin events (Serenitatis, Crisium and Imbrium) were chosen for the modelling to study the diffusion of these basins' melt. In section 4, the characteristics of basin melt diffusion are first presented (section 4.4.1). The abundance of basin melt at Apollo and Luna sampling sites is then estimated and compared with the K-Ar radiometric ages from highland samples in section 4.4.2. Combining the results from both sections 4.4.1 and 4.4.2, the abundance of basin melt components at the potential landing site of the future CE-4 lunar mission is estimated. Some feasible suggestions are provided for sampling the potentially present melt material (section 4.4.2). In section 4.4.3, other factors influencing the distribution of melt are discussed, which should be considered for future models.

4.2. Model

The high temperatures and pressures caused by hypervelocity impact events on the Moon result in the melting of a fraction of the target materials. Such thermal events reset the radiometric clocks of the melted materials. The potassium-argon (K-Ar) clock is widely used in dating

impact melt since it is easily reset by thermal events (Flude et al., 2014; Jourdan et al., 2014; McDougall & Harrison, 1999; Wartho et al., 2014). High temperatures allow the decay product, Ar, to escape from the mother rocks as gas, which resets the system. Resetting ages can then be calculated by measuring the ratio of Ar to K concentrations. It should be noted that, in this study, when we use the term 'melt', it should be understood here to include material which has been heated above the K-Ar reset threshold but has not reached the melting point. The K-Ar clock reset is the measurable property that we aim to trace with the model.

Once impact melt has been generated, it is gardened by subsequent impact events diminishing its abundance and spreading it more widely. A schematic of the gardening process is shown in Figure 13 where the target is shown to experience two impact events. During the first impact, when time is t_1, a fraction of the old unheated materials of the target (white color in Figure 13) is excavated and melted. The radiometric clock of the melted material, that is the melt age, is reset to t_1 shown as a red color in Figure 13a. Part of the generated melt stays within the crater, and the remainder is ejected in the form of a mixed layer consisting of the newly melted material and the old unheated material, that becomes the ejecta blanket shown in Figure 13b (Melosh, 1989). The thickness of the ejecta blanket decreases with distance from the crater center whereas the fraction of melt in the ejecta increases (Figure 13b, Melosh 1989). At time t_2, a subsequent impact event occurs. It penetrates the previous ejecta blanket and excavates material from both the previous layer and beneath, melting a fraction of both (blue color in Figure 13c). Partial ejecta materials overlay the previous deposits (arrow in Figure 13d) leading to a locally more complex melt component structure. As more impact events occur on the lunar surface, a complex spatial distribution of differently aged melt components develops.

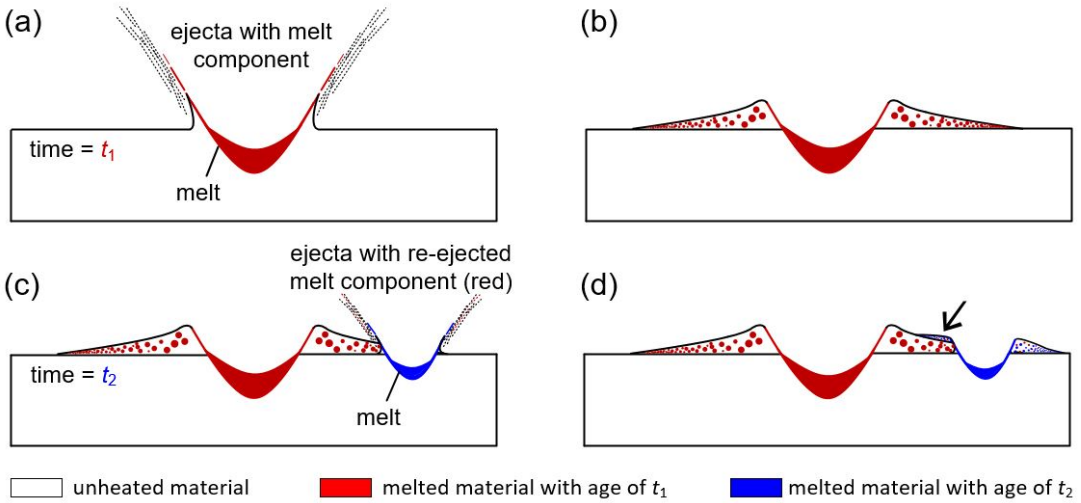

Figure 13 Schematic of the model where the white represents unheated material, red is the impact melt generated from the first impact event when time is t_1, and blue is the melt from the second impact at time t_2. The arrow in (d) points at the region of superposing ejecta.

4.2.1. Model steps

As seen from Figure 13, there are three key aspects which we considered when modelling the gardening process: the *distribution of impact events*, the *excavation processes*, and the *distribution of melted materials*.

Distribution of impact events: Due to the computational expense of the exponentially increasing number of simulated events as smaller impacts are included, a minimum crater diameter, D_{min}, is chosen. The maximum simulated diameter, D_{max}, is taken as 300 km, because this is the upper limit of the defined production function (PF) (Neukum, 1983). Unless noted otherwise, diameters here refer to the rim-to-rim distance of observed craters. By using the Monte Carlo method, the diameter of craters, D, is generated, in such a way that the SFD of the generated impact craters statistically conforms to the PF larger than D_{min} (Michael et al., 2016). The corresponding center of each impact crater is randomly distributed along a line. The average time to the next impact event larger than D_{min} in diameter, or impact rate, is calculated from the chronology function (CF) (Neukum, 1983), PF, and t (see Michael et al. 2018 for the detail).

Excavating processes: The excavation depth for each simulated crater, d_{exc}, is $D_t/10$ where D_t is the diameter of transient crater (Melosh, 1989). There are many scaling laws for D and D_t (Croft, 1985; Holsapple, 1993; Krüger et al., 2017; McKinnon et al., 1997; Melosh, 1989). We choose the standard ones in this study: for simple craters, $D_t = 0.8D$ (Melosh, 1989); and for complex craters, $D_t = (DD_Q^{0.13}/1.17)^{1/1.13}$ (McKinnon et al., 1997), where D_Q is the simple-complex transition diameter, and taken as 21 km (Pike, 1977). The corresponding volume of the excavated materials having a torus-like shape (grey zone in Figure 14) is estimated to be 1/3 of a disc with d_{exc} in thickness and D_t in diameter (zone filled with black slash in Figure 14): $V_{exc} = \pi R_t^3/15$, where R_t is the radius of impact craters and equal to half of D_t. The excavation unit is assumed to be a cuboid with 1/3 D_t in length and d_{exc} in thickness located at the crater center. For the conservation of mass, the volume of each penetrated layer is diminished.

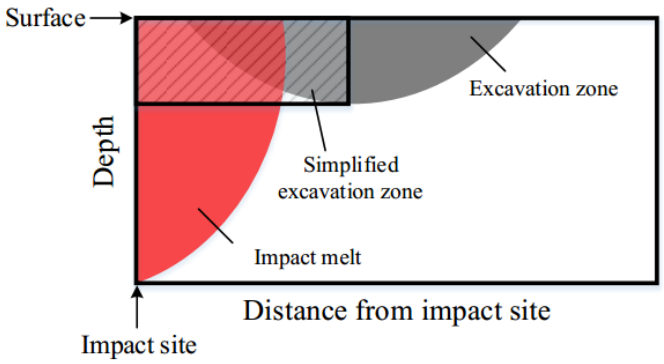

Figure 14 Schematic showing typical geometry of melting zone in iSALE modeling, with the impact-induced melt zone (red) and excavation zone in half space (grey, after Zhu et al. 2015). The calculation of V_{exc} in this study is on the basis of the simplified excavation zone shown as an area that filled with black slash.

Distribution of melt materials: The thickness of the ejecta layer decreases with distance from crater center, r: $\delta(r) = Ar^{-3}$ (Hörz et al., 1983; Shuvalov & Dypvik, 2013; Stöffler et al., 1975; Zhu et al., 2015), where A varies for craters with different D. To ensure conservation of mass, the integrated volume within five radii is taken to be exactly V_{exc}, based on which the variable A can be easily obtained for each differently-sized impact. The total volume of the generated impact melt with a reset age of the current model time is: $V_{melt} = cD_t^d$, where c and d are taken as 1.4×10^{-4} and 3.85, respectively (after Cintala & Grieve, 1998). The impact-induced melt zone during a single impact event is shown in Figure 14.

The distribution of material that experienced different degrees of shock pressure (including melt) is not well quantified and no scaling laws exist (Stöffler et al., 1975; Wünnemann et al., 2016). Recently, the linear relationship between the melt fraction in the proximal ejecta and the distance from crater center was found by means of numerical modelling using the iSALE shock-physics code (Wünnemann et al., 2006). In their model, basalt projectiles with diameters from 2.5 km to 10 km vertically impact a homogeneous target (same material as projectiles) at various impact velocities from 15 to 18 km/s, typical for the Moon. The transient crater radius of the generated impact crater ranges from 33 km to 107 km. By assuming a continual distribution of melt in the proximal ejecta, the thickness of the impact melt, δ_m, was obtained by multiplying the ejecta thickness with the melt proportion. It showed that the melt thickness decreases as a power law with increasing distance from the crater center. The exponent is approximately equal to -2: $\delta_m(r) = A_m r^{-2}$. A_m is recalculated for craters with different sizes to conserve V_{melt}, similarly to A described above, by taking the integrated melt volume within five radii to be exactly V_{melt}. The melt ratio, f_{melt}, at r is therefore equal to $\delta_m(r)/\delta(r)$. The amount of impact melt that is ejected from the crater depends on the transient crater size. According to Cintala & Grieve (1998), who combined different scaling relationships to estimate the ejected melt fraction, the amount of melt that remains inside the crater varies between 30% and 70% (assuming different scaling parameters, and crater sizes up to 400 km). In iSALE models for a projectile size range of 20 – 1000 m and an impact velocity of 20 km/s, only 80 – 90% of melt remain inside the crater. Therefore, we decided to use an intermediate value of 75%. Despite being a significant approximation, we believe this should be close enough to allow us to build up a qualitatively accurate view of the melt redistribution through multiple impacts. In addition, we treat the melt that is deposited inside the craters as a simple lens, although the exact distribution is likely more complex. About 85% of the ejected material is deposited within five radii from the crater center, the region that consists of a proximal ejecta blanket and a transition to a patchy discontinuous ejecta zone. We assume that the ejecta material in patchy transition zones is also continually distributed in a thin layer and trace the melt only out to five radii from the crater center.

Figure 15 shows the ejecta and melt distribution of craters with diameters of 300, 100, and 5 km (dashed lines). It shows that the equivalent thicknesses – the components are mixed – of both the ejecta and melt decreases dramatically with distance from the crater center, and that larger craters produce a thicker layer within the five radii range (Figure 15a and b). The melt fraction of the largest crater (black dashed line in Figure 15c) is obviously greater than that of the smaller ones, and the farther from the crater rims, the greater the difference in the fraction of melt. When near the crater rim, the percentage of melt for 300-km, 100-km, and 5-km craters is 6.1%, 2.7%, and 0.2%, respectively; at five radii away from the crater center, the percentage of melt for 300-km, 100-km, and 5-km craters is 28.7%, 12.6%, and 1.1%, respectively.

Iteration: If t is less than zero – the present day – another impact is generated, repeating the above steps.

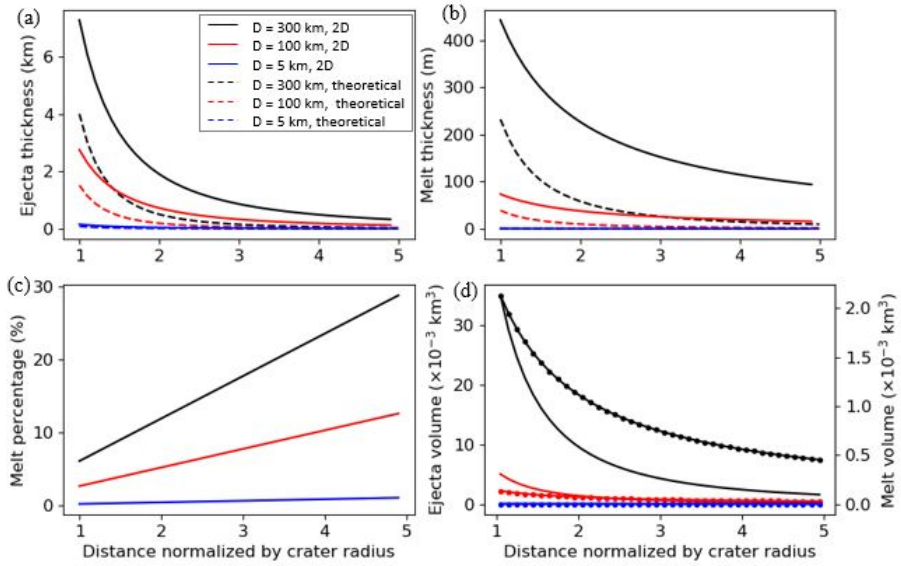

Figure 15 Distribution of ejecta and melt with increasing distance from the crater center, where black, red and blue are from craters with diameter as 300, 100, and 5 km, respectively. Dashed and solid lines are on the basis of theoretical and compressed 2D models, respectively. (a) Ejecta thickness distribution. (b) Melt thickness distribution (c) Melt percentage in ejecta. (d) Ejecta (solid lines, left y-axis) and melt volume (lines with dots, right y-axis) in a compressed 2D model taking the band width of 1 m.

4.2.2. Reducing the problem to two dimensions

Because of the complexity of tracking all the material during the cumulative gardening process, we reduce the problem to two dimensions (2D) in this study, so that the evolving distribution of the melt component with depth along a path is simulated. It is helpful for the analysis and understanding of simulation results and builds a bridge to a three-dimensional model in future work.

To investigate the lateral diffusion of melt, a narrow band is chosen for modelling. By dividing the surface into cells, the ejecta volume and the portion of unheated and melted materials are

recorded laterally and with depth, tracking the ages of the newly generated impact melts as current model time. The cell resolution is chosen as 2 km. The diffusion of melt is well-traced at such a resolution, while saving computational expense. D_{min} is thus taken as 5 km, the D_t of which is about twice the cell resolution. Therefore, the gardening trace of smallest simulated craters can also be well-recorded. The thickness of the ejecta layer and melt is multiplied by the overlying fraction when partial coverage of a cell occurs.

Only the material deposited along the band is traced. If we were to treat the model in three dimensions, the quantity of materials in the band would decrease on each impact because material is transported outside the band (Figure 16a). However, on the real lunar surface, the total mass of material on the band would be constant in the long term with the symmetrical return of material from outside the band. To conserve the mass in 2D model, we take instead that all the excavated materials on the band are transported along the band instead of spread radially (Figure 16). In addition, although after the concentric 'compression' the ejecta thickness becomes larger, we maintain the melt fraction in the ejecta (Figure 16c), ensuring that the main characteristics of the melt distribution remain unchanged.

This procedure may be considered as compensating the ejecta produced by craters outside the band that the model does not record. In our simulations, the band width, B, is taken to be much smaller than the crater size such that the locations at the same longitudinal sites of the band have the same distance to the impact center. We can easily obtain the total volume of the excavated materials beneath the band: $V_{exc\_band} = 2R_t^2B/15$. The volume of ejected material that is deposited along the band is $V_{ejecta\_band} = 2\bar{\delta}R_{ce}B$, where $\bar{\delta} = 3A/\left(25{R_t}^3\right)$ is the average ejecta thickness, and $R_{ce} = 4R_t$ is the radial length of the ejecta coverage. The lost volume after ejection is then equal to $V_{loss} = 7R_t^2B/75$. This lost material is added to the band for mass compensation. Such compensation is easy to realize for smaller craters on the lunar surface, because their high frequency of occurrence quickly leads to an average state with no net movement. For example, the lost volume of an impact with R_t in radius can be compensated by about $0.36R_t/B$ occurrences of a nearby impact with the same size. For larger craters, the lower impact frequency may mean that the average state is not so quickly attained, but we assume for the sake of the 2D model that this does occur.

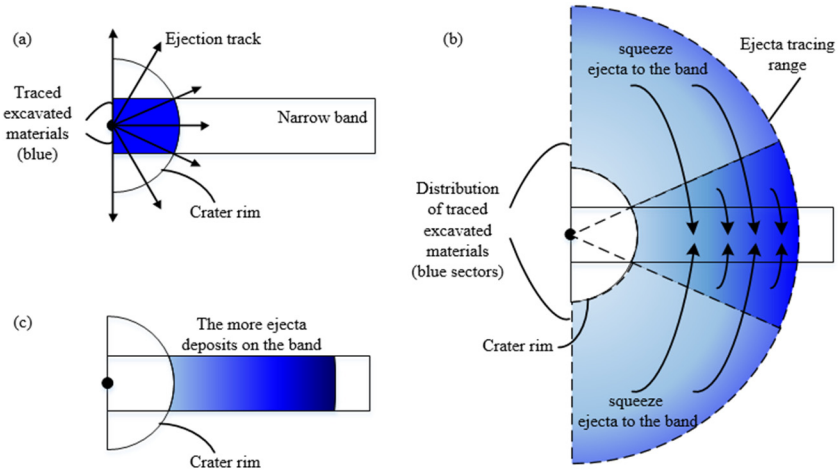

Figure 16 Schematic distribution of excavated materials for a crater half-space inside the band when reducing the problem to two dimensions. (a) The excavated material in the narrow band of the 2D model is traced (blue). This material would be radially distributed as indicated by the black arrows. (b) The excavated materials are distributed within five radii (semicircle outlined by dashed curves), where the farther locations receive less absolute melt quantity, but it nevertheless makes up a greater fraction of the ejecta there, indicated by the darker blue. To conserve the mass in 2D, the ejecta materials that would be deposited outside the band are added into it. (c) The band therefore possesses more ejecta material appearing the much darker blue. This compensates ejecta generated by craters outside the band that the model does not record, while maintaining a realistic average transport distance.

The compensation process is shown in Figure 16. As seen that the material that is distributed outside the band is compressed into it resulting in a local concentration of material shown as the deeper color in Figure 16c. Taking craters with 300, 100, and 5 km in D_t as an example, Figure 15 (solid lines) shows the distribution of ejecta and melt of craters after the concentric 'compression'. Both the ejecta and melt products are increased: the ejecta thickness is 3 km (1.3 km, 0.15 km) thicker at the crater rim, and 0.3 km (0.1 km, 0.006 km) thicker at five radii for 300-km (100-km, 5-km) crater; the melt thickness is 211 m (34 m, 0.16 m) thicker at the crater rim, and 84 m (12 m, 0.06 m) thicker at five radii for 300-km (100-km, 5-km) crater.

To investigate the transportation of melt from selected lunar basins, a great circle passing through the Imbrium, Crisium, and Serenitatis basins was chosen for modelling (Figure 17). Since here we focus on the basin melt components, the model time was started at the estimated formation time of the oldest Serenitatis basin (4.13 Ga, Table 4) instead of 4.5 Ga. Based on $N(20)$, the number of craters larger than 20 km, measured by Fassett et al. 2012, we can estimate plausible ages for these three basins (Michael et al., 2018). The ratio of $N(1)$ (the number of craters larger than 1 km) and $N(20)$ is first calculated using the PF, which is then applied to obtain the corresponding $N(1)$ values for each basin. By looking up these $N(1)$ values in the lunar chronology function (Neukum, 1983), the age of Serenitatis, Crisium, and Imbrium basin are then calculated to be 4.13, 4.09, and 3.88 Ga, respectively.

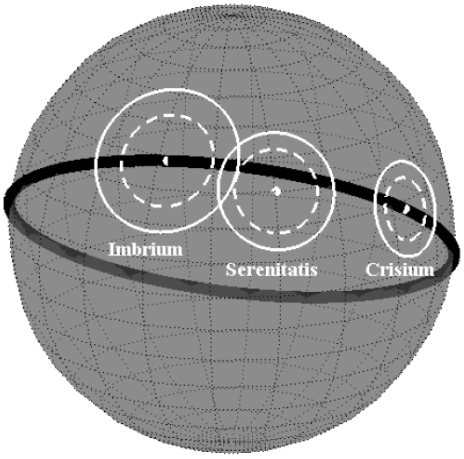

Figure 17 A band passing along the great circle through the mid- to late-forming Imbrium, Serenitatis, and Crisium basins, where the solid and dashed outlined circles indicate the rims of final and transient craters, respectively.

The number of layers in each cell becomes large as the simulation progresses, increasing the computational cost of tracing the differently aged melt (the same issue arose in the previous surface-averaged model, Michael et al. (2018)). The depth in each cell is, therefore, periodically simplified into a sequence of layers where the shallower layers are thinner to preserve a fine resolution of the melt distribution near the surface, with the deeper layers having a greater thickness to maintain a more averaged distribution. The stack of layers is amalgamated into simpler ones each time the number of layers exceeds a given threshold.

4.3. Results

Both the size and formation rate of the simulated craters affect the distribution and volume of melt components. To better explain the model, the migration of impact melt is first explored in this section by assuming a fixed crater size with a uniform impact rate. Further simulations were performed to understand how different factors affect the presence of melt individually. Therefore, a second model was run for a size–frequency distribution that conformed to the PF but still with a uniform impact rate. Finally, we investigated the diffusion features of the melt from three mid- to late-forming basins (Serenitatis, Crisium and Imbrium basin) and carried out the complete simulation considering a realistic impact rate (Neukum, 1983) and crater size distribution (PF) . The above three simulations all use the same model with different parameters.

4.3.1. Migration of impact melt

How does the melt evolve laterally and with depth under the influence of subsequent impacts? Impact events cause a redistribution of material leading to migration and burial. In the first instance, we consider a series of impacts with D_t fixed at 40 km.

Figure 18a1-a5 shows the evolving distribution of the melt from the first impact event when the 1000 km line segment experiences one, 30, 50, 100, and 150 impact events. The impact center of the first impact is set to be the midpoint of the great circle (Figure 18a1). In Figure 18b1-b5, we introduce the same data with a logarithmic depth scale to show more detail near the surface, noting that units of color at greater depth now represent a relatively larger volume. As seen from Figure 18b1, when just formed, the majority of the melt stays within the crater; the remainder is ejected outside the crater where more distant locations receive a higher fraction of melt in the ejecta layer.

With an increasing number of subsequent impact events, the melt from the first impact becomes buried. As seen in Figure 18a3 and b3, the deepest melt is located at ~7 km, after 150 impact events have occurred, which is about seven times the depth of the initial crater (~1 km). The buried melt can also be re-excavated to the surface exposing it to the further gardening. For example, melt buried at ~1 km depth after 30 impact events (Figure 18b2) is re-excavated to the shallow surface leading to the abundant melt assembled between ~150 – 150 km indicated by the red regions it the top ~0.1 km in Figure 18b3.

The later impacts spread the melt further through the ejection process. Almost all the 1000 km path segment contains at least a minor component of the first impact's melt after 150 impacts (Figure 18a5 and b5), but the abundance varies: Figure 18b5 indicates that the uppermost layer (top ten meters) with a melt fraction larger than 0.01 extends about 380 km around the initial concentration region (i.e., center part of the path in Figure 18b1); more distant locations have very low concentrations (10^{-5} or less shown as grey color in Figure 18, indicating regions that have at least some admixture of melt).

The melt is also depleted through gardening because of the re-melting by later impacts. The distribution of the melt volume of the first impact is shown in Figure 18c1-c5. Initially, there is 6.6×10^{-3} km^3 deposited over the narrow band (chosen as 1 m in width), which is ~0.003% of the total volume for a crater with D_t at 40 km (206.1 km^3). The majority of it remains inside the crater generating a pronounced peak; this peak still remains after 50 impact events. After 100 impacts have occurred, ~13% of the total melt is depleted (Figure 18c4), and the melt that was initially deposited inside the crater has been transported over a wider range indicated by the broader flatter peak. The final 50 impacts re-melted (depleted) an additional 3% of the melt (Figure 18c4), continuing to spread the melt distribution.

The distributions of the total generated impact melt from all the impacts are shown in Figure 18d1-d5. More and more impact melt (from 0.007 km^3 to 0.655 km^3) is generated with the increasing number of impact events, but the local diversity is quite strong. After 150 impact

events, each location is covered with at least 5×10^{-4} km^3 melt. The surface layer experiencing continual gardening accumulates melt with various ages.

To summarize, we see that the existing melt is depleted by re-melting, partially transported away from its initial location by excavation, buried more deeply by overlaying ejecta from subsequent impacts, and buried melt is sometimes re-excavated to the surface where it is subject to further gardening.

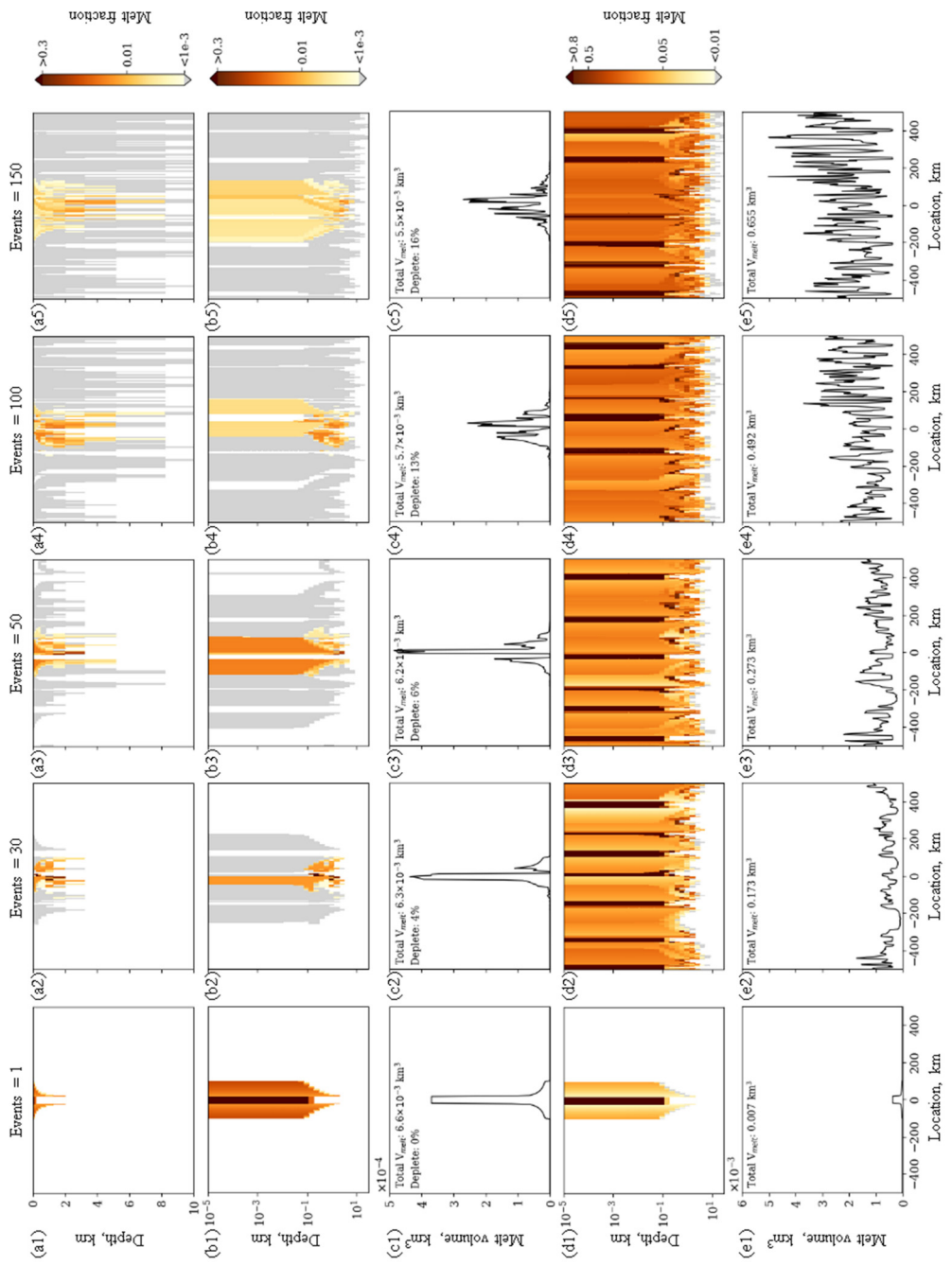

Figure 18 Evolving distribution of impact melt after one (first column), 30 (second column), 50 (third column), 100 (fourth column) and 150 (last column) impact events, where D_t is fixed to be 40 km. Both a1-a5 (linear depth) and b1-b5 (logarithmic depth) show the spatial distribution of the impact melt from the first impact event. The latter better displays the melt distribution at the near surface. The distribution of total melt volume of the first impact event (c1-c5) indicates that the generated impact melt is depleted by the re-melting process of subsequent impact events. The melt that was transported farthest has the smallest volume. The total melt volume distribution is shown in e1-e5. More and more impact melt is generated with the increasing number of impact events, but the local diversity is quite strong. In a1-a5, b1-b5, and d1-d5, depth is referenced to the surface boundary, and thus shows no topography. Note that all the calculations concerning melt volume are based on a band of 1 m in width.

4.3.2. Realistic crater size distribution

The situation where the SFD of craters statistically conforms to the PF and the impact rate is uniform is simulated to study the influence of crater size on impact melt distribution. The path length is chosen as 2000 km, the approximate ejecta coverage of the theoretical maximum crater diameter (i.e., D_{max}). One hundred and fifty impact events are simulated with diameters ranging from 5.1 to 247.6 km. The spatial distribution of the impact craters is shown in Figure 19a, where the different colors are applied to better distinguish the impact positions. The point size shows the scale of the impact craters, where the bigger points represent larger crater sizes. Note that the smallest craters are exaggerated to make them visible. The impact events are randomly distributed along the path. Because of the shape of the PF, there are many more small craters than large ones: there are 114 (76%) small craters with diameter smaller than 30 km, and only 3 (2%) craters larger than 150 km. The small-scaled impacts have a small gardening range and shallow gardening depth suggesting a light effect on the existing melt, which could, therefore, be considered as *local gardening*.

Emplaced melt can be depleted because of later impacts, but it can also be preserved if it remains buried. For example, Figure 19b shows the spatial distribution of melt from the 142nd impact (impact 'b'). It is located at -769 km on the path with a diameter of 50.0 km and followed by the big impact 'b_{next}' (the 150th), that occurred close to impact 'b' at -641 km on the path. The impact locations of both events are denoted by black arrows in Figure 19a. The impact 'b_{next}' is large (66.7 km). Its thick ejecta blanket covers the majority of the impact 'b' melt, and buries it to deeper than 200 m. Only the remaining unburied melt (at ~800 km on the path) is subjected to further gardening. The distribution of the melt volume of impact 'b' (Figure 19e) shows that almost all the produced melt by impact 'b' is preserved until the present day.

The melt generated by the small-scaled impacts is more easily depleted than that of larger impacts, for example the impacts 'c' and 'd' (black arrows in Figure 19a). The early impact 'c' with a diameter of 232.3 km is much bigger than the recent impact 'd' (14.8 km in diameter). The spatial distributions of the generated melt (Figure 19c and d) suggest that the melt of early impact 'c' (the 29th impact) is extensively gardened, while that of the young melt of impact 'd' (the 118th impact) experiences less gardening. However, as seen from the distribution of melt volume, only 6.5% of the total generated melt of impact 'c' is depleted until the present day (Figure 19f). In contrast, the melt of the recent small impact 'd' decreases by 24.8% (Figure 19g).

To summarize, the small-scaled impacts garden the surface within a narrow range at shallow depth, which may be characterized as *local gardening*. The fate of the impact melt not only depends on the age, but also the burial depth that may protect it from further gardening.

Furthermore, large-scale impacts generate a greater volume of melt, a considerable fraction of which is expected to survive to the present day; the melt from small impacts, however, is much more easily transported and diminished.

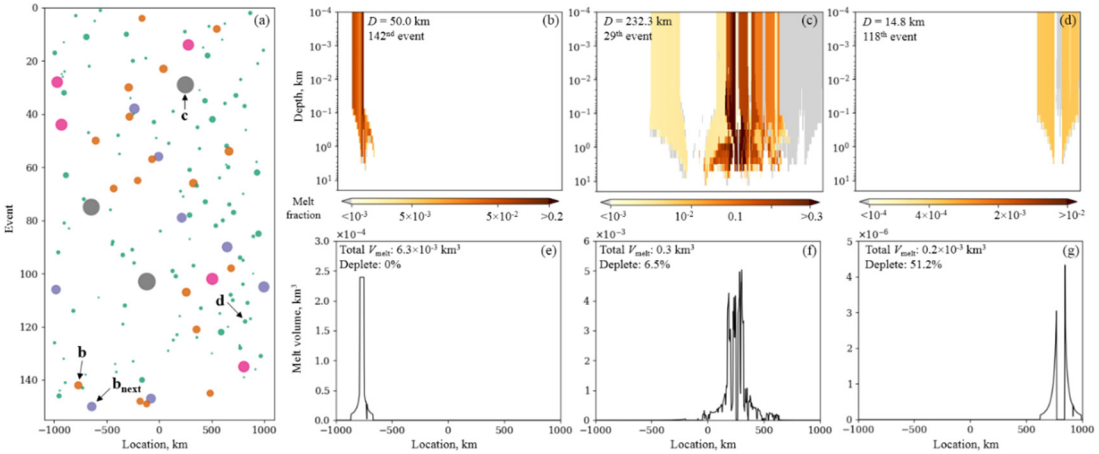

Figure 19 (a) Spatial distribution of impact craters, where bigger points represent the larger impact craters (but not to scale), and different colors are applied to better distinguish the impact positions. (b), (c), and (d) show the spatial distribution of melt from impact 'b', 'c', and 'd', respectively, the impact location of which is denoted by the arrows in (a). b_{next} in (a) points out the location of the impact that occurred after impact 'b'. The distribution of melt volume of impact 'b', 'c', and 'd' is shown in (e), (f), and (g), respectively. Note that all the calculations concerning melt volume are based on a chosen band width of 1 m.

4.3.3. Diffusion of basin melt

Because of the exponential increase of the melt volume with increasing crater size (Figure 15), giant basin-forming events produce an overwhelmingly greater volume of melt than smaller impacts with the ejecta covering a much wider area and a thicker melt lens. Because of the importance of the identification of basin melt to the lunar chronology system and thus to our understanding of lunar geological history, the migration of basin material through impacts is of special interest.

The evolving distribution of melt from basin-forming events was simulated in a third model run where the impact rate matches the CF and the crater SFD statistically conforms to the PF (Neukum, 1983). The mid- to late-forming Serenitatis, Crisium, and Imbrium basins were chosen for modeling. Their great size results in an extensive gardening range and the generated melt is very likely to survive in the near surface due to their relatively late occurrence. It should be noted that since the relationship between D and D_t mentioned in section 3.4.1 cannot be extrapolated to the basin size (e.g., Melosh et al. 2017), the D_t values of basins in this study adopt the results from Wieczorek & Phillips (1999) where the diameter of excavation cavities is obtained by using a crustal thickness model (Table 4). D and D_t of basins are shown in Figure 17 (Table 4). We chose a great circle which passes through these three basins (Figure 17), and

the center of Imbrium basin is set as the midpoint of the circle. The path length is 10920 km, the circumference of the Moon.

Table 4 Model age, size, and location of the three basins in simulation.

Basin	$N(20)$[1]	$N(20)e$[1]	Age (Ga)[2]	D_t (km)[3]	d (km)[4]
Serenitatis	155	60	4.13	657 (582)[5]	865
Crisium	113	11	4.09	487	2049
Imbrium	30	5	3.88	744	0

1 Fassett et al. 2012; 2 Spudis 1993; 2 The plausible ages of basins are estimated based on $N(20)$ from Fassett et al. 2012; 3 Wieczorek & Phillips 1999; 4 Distance from Imbrium basin center;5 (582 km) is the length that Serenitatis basin cross the great circle.

The traditional tail-end impact rate (i.e., the impact flux declines exponentially over the first billion years of lunar history) is applied in this simulation (Figure 20a, Neukum, 1983). The number of impacts occurring along the path is calculated as the square root of the number of impacts that would theoretically occur in a flat square area with edge length equal to the path length. Including the three basin events, we simulate 390 impacts that occur along the band. It can be seen in Figure 20a that the impact rate before ~3.0 Ga is much higher than that in the later period: 347 (89%) events occur between 3.80 and 4.13 Ga; 38 (10%) events happen between 3.0 and 3.8 Ga; only 5 (1%) during the last 3.0 Ga. As before, the small impacts predominate: 293 (75%) craters with diameter smaller than 30 km, and only 11 (3%) craters larger than 150 km. The distribution of impact locations is shown in Figure 20b. To better distinguish the early dense impacts, only those which occur before 3.6 Ga are shown. The three basin events are indicated with arrows.

We assume that 75% of the melt from Serenitatis, Crisium, and Imbrium basin is retained within each cavity, generating the 31, 18, and 39 km thick melt lens, respectively. The ejecta range is 2910, 2435, and 3720 km, respectively, much greater than for the smaller craters in the above simulations. Those impacts are so small compared with the basin-forming events that the mixing could be considered as *local gardening*.

The present-day distribution of impact melt with depth for three basins is shown in Figure 20c-e. The initially generated melt is depleted and redistributed by the subsequent impact events: the smaller impacts mainly locally garden the near-surface materials, but the giant basin-forming events can significantly alter the existing basin melt reservoirs. As can be seen, Serenitatis melt in the near surface is almost non-existent with a melt fraction smaller than

~0.005. Some of it is even smaller than 0.001 denoted by the grey color in Figure 20c, the west and east part of which is mainly re-distributed by the subsequent Imbrium and Crisium event, respectively. The ejecta materials from both Crisium and Imbrium basins cover the remaining melt of Serenitatis basin burying its melt to a greater depth. Some of the buried melt was re-excavated to the surface where it was subject to further gardening, such as the melt at ~400 km along the path (arrow in Figure 20c). The Crisium basin melt at the near surface is also significantly depleted and irregularly distributed, where the ejecta in the west is buried by Imbrium ejecta, and the eastern part is mainly gardened by smaller impacts. Without the excavation by other basin events, most of the Crisium melt still lies around the impact center, with only a few relatively large cratering events bringing a portion of it to the surface, like the melt at ~1300 km on the path (arrow in Figure 20d). The relatively young Imbrium cavity melt distribution was not dramatically altered although several depleted patches appear in its ejecta blanket. The subsequent smaller impacts producing less melt and smaller ejecta blankets only depleted and buried a small part of the Imbrium melt, so that the Imbrium melt is still abundantly distributed in the near surface.

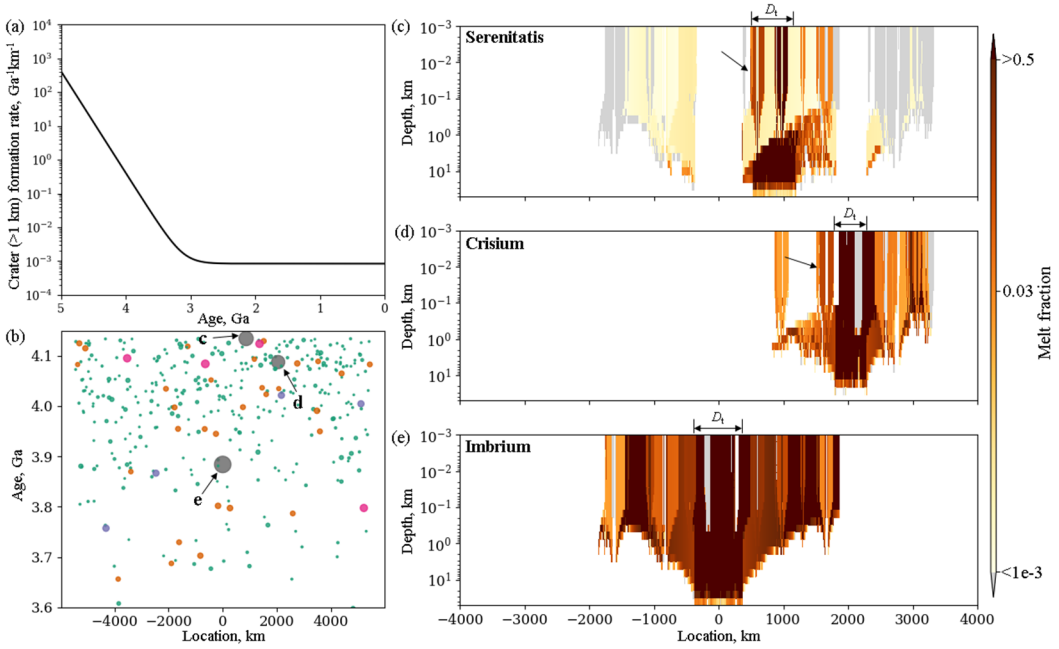

Figure 20 (a) Exponential decay rate function for crater size-frequency over time (Neukum, 1983). (b) Spatial distribution of impact centers. The locations of Imbrium, Crisium, and Imbrium basin are denoted by the arrows. (c) to (e) show the present-day distribution of impact melt of Serenitatis, Crisium, and Imbrium basin, respectively. The D_t of each basin is marked on top of each figure. Depth is referenced to surface boundary, and thus shows no topography. The arrows in (c) and (e) denote the re-excavated Serenitatis and Crisium melt, respectively.

The distribution of average melt fraction with depth is shown in Figure 21a where the melt of Imbrium, Crisium, and Serenitatis basins is shown in blue, green, and red, respectively. As seen that the largest and relatively young Imbrium melt remains dominant; the burial of Imbrium

and Crisium ejecta blanket results in the least Serenitatis melt at the shallow ~1 km depth. The majority of Serenitatis melt is deposited at greater depths with a comparable fraction of Imbrium melt. In addition, after the formation of the Imbrium basin, the last giant impact event, the average contribution of the three basins to melt in the near surface was confirmed. The subsequent smaller craters can only diminish a small part of basin melt, and thus the average presence of basin melt is almost unchanged in the near surface shown as flat curves in Figure 21a.

The lateral distribution of melt volume is shown in Figure 21b. Because abundant melt stored within their cavities, the giant basin-forming events leave a clear signature on present day as denoted by the arrows in Figure 9b. The lesser-scaled gardening makes the distribution of the basin melt patchy. In addition, smaller impacts with diverse size randomly garden the surface producing various amounts of melt along the great circle leading to the fluctuations in Figure 21b. This makes it difficult to estimate the fraction of basin melt at specific sites, such as Apollo and Luna sampling sites, because every instance of the random bombardment in the model will produce a statistically different outcome.

The distribution of the differently-aged melt (Figure 21c) also reflects the overwhelmingly large quantity of basin melt (three prominent peaks indicated by arrows). In addition, the earlier more intense bombardment results in the higher abundance of melt older than 3.5 Ga. The recent lower impact rate generates much less melt, but the majority of it could survive until the present day because of the small probability of being gardened.

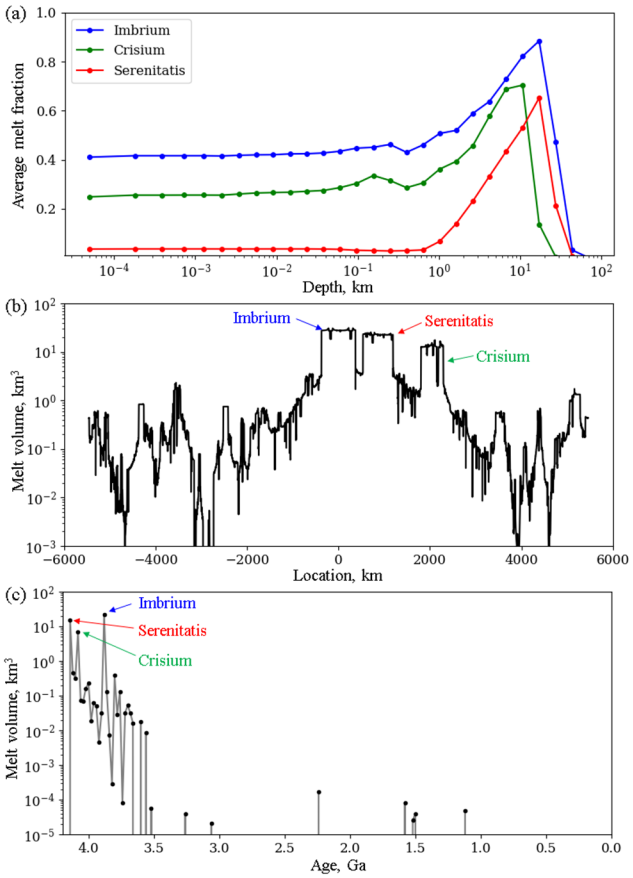

Figure 21 (a) The distributions of melt fraction with depth, where the red, green, and blue indicate the melt from Serenitatis, Crisium, and Imbrium basins, respectively. The dots on curves indicate the thickness of the simplified stack layers. (b) The local distribution of melt volume. The arrows point out the peak values caused by the three basins. (c) The distributions of melt volume with age. The arrows point out the melt generated by the three basins. Note that all the calculations concerning melt volume are based on a chosen band width of 1 m.

4.4. Discussion

4.4.1. Characteristics of basin melt diffusion

Lunar highland rocks contain evidence (e.g., K-Ar system) of impact events on an ancient lunar curst, through which geochemists are able to trace the early lunar bombardment history. Tera et al. (1974) found the clustering of radiometric dates around 3.9–4.0 Ga based on the lunar highland samples, the cause of which has been debated for decades (e.g., Baldwin, 1974; Bottke et al., 2012; Chapman et al., 2007; Cohen, 2000; Hartmann, 2003; Morbidelli, Marchi, et al., 2012). Tera et al. (1974) suggested that it resulted from an intense bombardment episode on the Moon, called the terminal cataclysm. Michael et al. (2018) investigated whether or not a lunar terminal cataclysm occurred by reanalyzing the radiometric dating of lunar highland rocks and building a numerical surface-averaged impact gardening model. Their simulation results suggested that the cataclysm, if it occurred, should generate a rather intensive peak, which is inconsistent with the relative plot of summarized radiometric ages. The clustered ages were

more likely caused by the contamination of Imbrium ejecta at the sampling sites. The results on transportation and mixing of basin melt obtained in this study are intended to further refine our understanding of how this process might occur.

Impact melt is laterally transported away from its source if there are sufficient later impacts as described in section 4.1. The melt from small impacts, with relatively small volume, is easily depleted before it is transported very far. In contrast, the large quantity of melt generated by large impacts, especially that of the giant basin events, can migrate significant distances. Figure 22a-c shows the averaged fraction (sum of the average melt fraction of each layer that is weighted by the ratio of its layer thickness to the total depth) of melt from Serenitatis, Crisium, and Imbrium basin, respectively, in the near surface along the great circle defining the modeled area. The thinner surface layer, where Apollo and Luna samples were collected and the *in situ* drill tube experiments were performed (McKay et al., 1991; Vaniman et al., 1991), is chosen to investigate the scenario of the melt distribution. The collected samples in the topmost surface have been subjected to extensive impact gardening. The melt distribution range of Serenitatis basin is about two times larger than its initial state because of the re-excavation by the subsequent Crisium and Imbrium basin events (Figure 20). Without transportation by the giant basin events, the melt distribution range of both the Crisium and Imbrium basins, nevertheless, has not been significantly altered. This suggests that local gardening by smaller impacts is not able to spread a significant part of the basin melt to more distant locations, although it can result in a local enrichment zone in the surface fine layer if the basin melt is freshly excavated. The lateral transportation efficiency of the impact melt by smaller impacts is, therefore, not high if only the proximal ejecta process (five radii in this study) is considered. Studies on the mixing zone at mare/highland contacts also support the low transportation efficiency of surficial materials, where the narrow mixing area has been interpreted as the result of the local mixing (continuous ejecta) rather than distal ejecta deposition (e.g., Y. Huang et al., 2017; Li & Mustard, 2000, 2005). The melt materials in the distal ejecta, that our model did not trace, may indeed be transported very far, but their fraction is small (usually <15% of the total ejecta material). In addition, it is heterogeneously distributed. The majority of distal ejecta is concentrated in patchy rays which can be easily observed through high-resolution images if it is young. This has helped to find plausible source of distal materials in the collected samples. For example, the abundant highland materials of Apollo 15 samples were thought to be correlated with Aristillus and Autolycus craters based on their bright ray trace (Carr et al., 1971; LSPET, 1972; Spudis and Ryder, 1985).

Looking at the distribution with depth, existing impact melt can both be buried to greater depth and/or re-excavated to the near surface as described in section 4.3.1. As seen from Figure 20, the local gardening by the smaller impact events after the formation of basins strongly mixed

the basin melt in the surface layers resulting in an irregular distribution which has significant consequences for scooped samples at the landing sites. For the younger Imbrium basin, the melt is depleted by local gardening. For an older basin like Serenitatis, the distribution is more complicated, because the majority of the melt is deeply buried by the subsequent Imbrium and Crisium basin events. When subsequent lesser-scaled impacts are big enough, a portion of the buried melt could be re-excavated to the surface, augmenting the local melt fraction and generating an enrichment zone like the area at ~400 km in Figure 20c and ~1300 km in Figure 20d. In addition, the melt at deep depth, where the smaller impacts are not able to excavate, is shielded from the gardening process.

4.4.2. Comparison with radiometric dating

In general, the remaining basin melt at the present day is distributed in/around the center of the impact. As seen from Figure 20, the majority of basin melt is distributed inside the original cavities. Although the old Serenitatis melt is buried, local gardening within the basin still has a high probability of excavating the melt beneath, resulting in a melt enrichment zone. For the melt in the ejecta, the low lateral transportation efficiency (described in section 434.4.1) protects it from long-distance migration. Basin melt is, therefore, spread within proximal range if no basin-scaled gardening occurs.

The small distance between the basins and the sampling sites (Apollo 14-17 and Luna 20) provided a high probability of finding components of basin melt in the collected samples. The arrows in Figure 22a-c point out the relative positions between the sampling sites and the center of each basin (each sampling site has two probable values of melt fraction indicated by arrows, because there are two sites on the path that have the same distance to a particular location). Our simulation results show that the materials collected at the Apollo and Luna sampling locations could contain the basin melt to different degrees, where the older basin generally remains the least abundant melt in the surficial layer: Imbrium melt could be expected at Apollo 14-17 sampling sites with a fraction of about 0.6, 0.3, 0.5 and 0.4, respectively; Crisium melt would be expected at Luna 20 and Apollo 17 sampling sites with a similar fraction about 0.05; and Serenitatis melt would be present at all the Apollo and Luna sampling sites but the less abundance where the fraction is about 0.002, 0.018, 0.00, 0.018, and 0.0016 for Apollo 14-17 and Luna 20 sampling sites, respectively.

To compare with the radiometric age results, Figure 22d presents the relative age probability plots for K-Ar ages of highland rock from Apollo and Luna samples from the data of Michael et al. (2018). There are 25, 8, 41, 36 and 7 determinations of impact melt breccias for Apollo 14, 15, 16, and Lunar 20 highland samples, respectively: the Apollo 14 plot shows a prominent bulge centered at ~3.85 Ga with four secondary peaks at 3.80, 3.85, 3.89, and 3.95 Ga and one

additional minor peak at 4.10 Ga; the Apollo 15 plot shows only one peak at 3.87 Ga; the Apollo 16 plot shows one prominent peak at 3.87 Ga with three additional peaks at 3.67, 3.89 and 4.20 Ga; the Apollo 17 plot shows a prominent peak at 3.88 Ga with three smaller peaks at 3.98, 4.05, and 4.13 Ga; Luna 20 plot shows four comparable small peaks at 3.75, 3.88, 3.98 and 4.10 Ga. The small number of age determinations suggests the secondary peaks may be within the statistical noise and the most meaningful feature is probably the prominent bulge.

The prominent peak around 3.88 Ga seen in the Apollo samples is consistent with the simulated results that predict a high fraction of Imbrium melt at these sites. For Crisium melt, only Apollo 17 and Luna 20 sampling sites are located in its ejecta range, and the others are too far to mix with its melt. Figure 22d shows that there is no obvious peak around 4.09 Ga from the Luna 20 and Apollo 17 samples, but both sites are very likely to collect samples in this age with the relative probability of ~0.2 and ~0.5, respectively. It is consistent with the predicted smaller fraction of Crisium melt comparing with predicted abundant Imbrium melt described above. Therefore, if the basin ages used in this study are close to the true values, the distribution of radiometric ages could be a consequence of the mixing of basin melt. For Serenitatis melt, the radiometric ages differ from the simulated results in that we expect very little to no Serenitatis melt in the near-surface. The radiometric results show no presence of a peak at 4.13 Ga at the Apollo 14 and 15 sampling sites. However, one small peak around 4.13 Ga is seen in the Apollo 17 radiometric sample ages. Since the majority of Serenitatis melt is buried to greater depth by the Imbrium and Crisium basin events, its distribution in the near-surface layer depends on the gardening by smaller impacts that could re-excavated buried Serenitatis melt, if big enough, forming local melt-enriched zones. Nevertheless, the occurrence locations of smaller impacts are random such that a single simulation will not necessarily match the real abundances at any specific site. That is to say, the predicted melt abundance for the older basins in the shallow surface has lower accuracy. In addition, the heavy gardening that the Serenitatis melt has suffered since formation may have pulverized the melt materials to such a fine grain size that it has not been possible to identify its age with the current radiometric techniques.

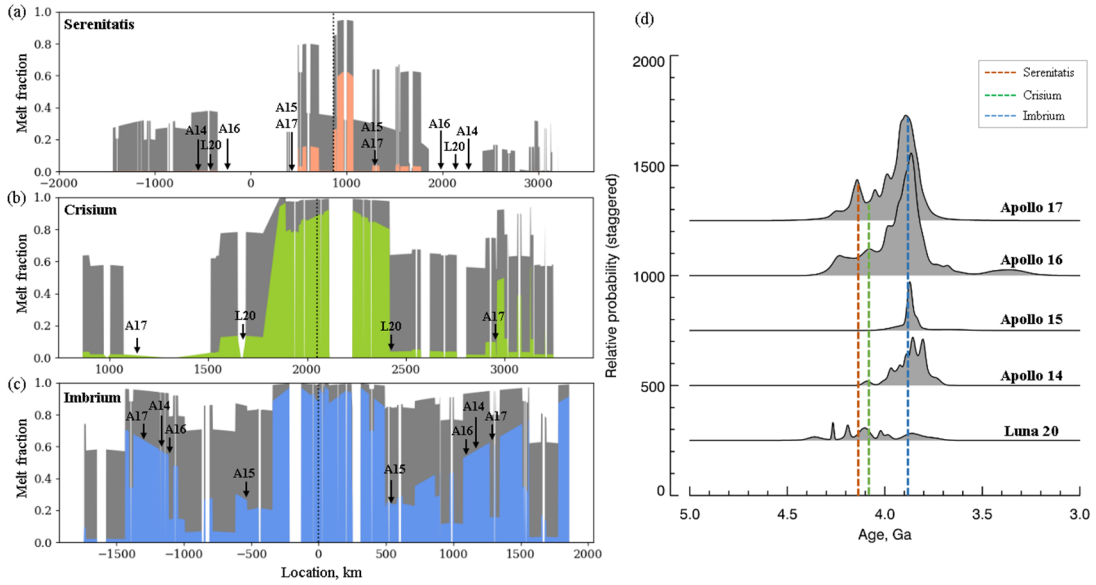

Figure 22 Average fraction of melt from Serenitatis basin (a), Crisium basin (b), and Imbrium basin (c) in the top 0.1 m (the first stack layer). The black dashed lines indicate the center of each basin. The figures are plotted twice: the red, green, and blue shaded plots are Serenitatis, Crisium, and Imbrium melt in linear scale; the grey shaded plots are the same data in logarithmic scale to show the small values. The arrows in (a) to (c) point out the relative distances between the Apollo and Luna sampling sites and the center of each basin, where 'A' and 'L' mean 'Apollo' and 'Luna', respectively. (d) Relative age probability plots of the K-Ar ages of lunar highland rocks for the Apollo and Luna returned samples, where Apollo 14, 15, 16, and Lunar 20 highland samples have 25, 8, 41, 36 and 7 determinations, respectively (after Michael et al. 2018). The red, green, and blue dashed lines indicate the calculated possible formation times of Serenitatis (4.13 Ga), Crisium (4.09 Ga), and Imbrium (3.88 Ga) basins, respectively. Implications for the choice of future sampling sites

Basin impact melt, that tells us about the process of giant basin-forming events and the formation time of basins (Spudis & Sliz, 2017), is a prime target for future robotic or human sample return missions (Cohen et al., 2018; Ryder et al., 1989). If melt materials of more certain basin origin (like a basin melt sheet) were sampled, the age could provide a strong calibration point for the lunar chronology system (van der Bogert et al., 2018). It is thus a critical objective for lunar exploration.

Both the relative position to a basin center and the scooping depth of a sample influence the expected melt volume abundance. Figure 20 suggests that the area within or around the basin center provides the greatest probability of survival of basin melt. Without a strong disturbance by subsequent basin-scaled gardening, abundant basin melt could be collected in the surficial regolith layer (the average thickness is 5 – 6 m in the maria regions; 10 – 15 m in the highlands regions; e.g., Fa & Jin 2010; Fa et al. 2014; McKay et al. 1991; Shkuratov 2001). Nevertheless, scooped samples from the surficial layer are affected by the local smaller impact events. For the abundant young basin melt, local gardening decreases the content. In contrast, for more scarce older basin melt, local gardening may produce some enriched zones. Extended gardening in the topmost surface may also pulverize the melt materials resulting in a fragment size too

small to perform radiometric dating for current radiometric dating techniques. In addition, the melt sheet that originally covered the entire basin floor is often buried beneath extensive mare basalt that was not considered in this study, although some residue might be patchily exposed near the topographically-high mare-highland boundary of basin interior (Spudis & Sliz, 2017). All the above point towards the low probability of collecting old basin melt from the shallow surface.

Pure basin melt has a larger probability of being present at greater depths within basins as shown in Figure 20. We may expect that higher melt abundances could be sampled from low-lying outcrops within a basin, such as on the degraded walls of later-forming craters. Y.-H. Huang et al. (2018) also suggests a deeper sampling depth by building a model to investigate the gardening process of lunar glass spherules, one of the melt products. They suggest that a shallow surface sample is more likely to yield young melt, and the old melt materials in the topmost layer could be much diluted by younger deposits, while shielding them at greater depth.

The Chinese CE-4 mission this year will explore the SPA basin. The U.S. National Research Council (2007) identified that CE-4 mission can address the existence of the SPA melt (J. Huang et al., 2018; Wu et al., 2017), considered the oldest on the Moon (Petro & Pieters, 2004). The melt materials could, therefore, have been buried and depleted by the subsequent impact events, especially in the shallow surface available for sampling. The aim should be to explore material from as deep as possible where the buried SPA melt could be have been shielded from intensive gardening: such materials might be found in the low-lying outcrops or near the rim of a later-formed nearby big impact crater, like Apollo basin and Von Kármán crater (J. Huang et al., 2018; M. A. Ivanov et al., 2018): the selected potential landing sites, where SPA melt material was likely re-excavated during formation.

4.4.3. Other potential factors affecting the melt distribution

Impact angle: Previous analytical studies found the relationship between the volume of generated impact melt and the crater diameter used in this study: $V_{melt} = cD_t^d$ (Ahrens & O'Keefe, 1977; Cintala & Grieve, 1998; Maher, 1988; Pierazzo et al., 1997). Nevertheless, these results were based on the assumption of a vertical impact trajectory. With the development of computer performance, three-dimensional numerical simulations have been run to investigate the effect of the impact angle. Using hydrocode modeling, Pierazzo & Melosh (2000) found that more impact melt is generated with increasing impact angle (angle between the surface and impact trajectory). Abramov et al. (2012), making use of classic impact experiments, analytical studies, and numerical hydrocode simulations suggest that the volume of impact melt produced by a vertical impact is ~1.6 times more than that from the most probable oblique impact (45°) on the Moon. However, as described in section 3.1, excavation and burial play more important roles

in melt diffusion by dominating the transportation range and deposition depth. The probable over-estimated melt volume would not significantly change the features of the melt diffusion, although it could change the absolute abundances.

Scaling of crater diameter: There are various scaling laws for D and D_t especially for complex craters, because of the collapse of transient craters during modification stage and hence the indirect measurement of transient crater size (Melosh, 1989). For example, based on observations of ejecta at terrestrial and lunar craters, Croft (1985) derived an empirical relationship of $(D/D_t) = (D/D_Q)^{0.15}$. By combining a geometric model with the model of Holsapple (1993), Krüger et al. (2017) concluded that $D_t = 0.2799D^{1.1}$. Thus, different crater sizes are obtained using different scaling laws, leading to the difference in calculated melt production.

The calculation of the basin melt uses the same scaling laws as for smaller impacts in this study. However, the formation of giant basin events is more complicated, and these scaling laws might not be validly extrapolated to the basin size. Firstly, the hotter Moon during the formation of basins provides the higher internal energy resulting in the more abundant of generated melt (Abramov et al., 2012; Zhu et al., 2017). In addition, it was found that the giant impacts are affected by the target body's surface curvature, and the produced melt has no clear relationship with the basin size (Schultz and Crawford 2016). Furthermore, the terrains (i.e., multi-rings) formed during the late modification stage of cratering make the melt spatial distribution more complicated. The present-day distribution of the melt from basins obtained in this study thus likely represents a lower limit.

The transient cavity size of basins remains poorly understood because of their complicated formation conditions and great scale. In this study, we use the measurements of Wieczorek and Phillips (1999) to obtain the total melt volume of basins. However, there have been diverse estimates of transient cavities of lunar basins (Hikida & Wieczorek, 2007; Potter, Kring, et al., 2012; Potts & von Frese, 2003). For example, Hikida and Wieczorek (2007) estimated the excavation cavity diameters of 718, 560, and 895 km for Serenitatis, Crisium and Imbrium basins, respectively, which are 10%–20% larger than values used here. The corresponding volumes of melts are thus 1.4–2.0 times larger than values used in the paper. To figure out the potential bias caused by the measurements of basins' D_t, we tried simulations with 1.5 times greater size of basin transient diameter. The greater size results in a larger ejecta coverage and a thicker melt lens within basins, but the overall pattern of basin melt diffusion is similar to that in Figure 20c-e.

Emplacement of ejecta: On the real lunar surface, the ejected materials would mix with local materials during emplacement. This results in a lower fraction of newly-generated melt at

shallow depths, because otherwise more deeply-seated materials would be excavated to the surface. However, the overall picture of the pattern of evolving melt would not change. In order not to make model overly difficult to follow, we did not include this local mixing process in this work. We take the impact melt to form as a simple disc-like lens in a crater, which is a simplification. More realistically, we expect some of the hotter material to penetrate and mix into the fragmented material beneath the crater floor.

4.5. Conclusions

We investigate the mixing behavior of impact melt that is exposed to cumulative impact gardening. Once formed, the melt could be depleted by re-melting, spread to more distant locations by excavation, and buried by the overlaying ejecta of subsequent impacts. Large-scaled impacts producing significant volume of melt may easily leave a trace in the near-surface material until the present day. High-frequency smaller impacts, the melt of which is more easily depleted, change the local melt component in the near-surface.

To investigate the evolving distribution of the melt from giant basin events, three mid- to late-forming basins, namely Serenitatis, Crisium, and Imbrium basins were chosen for modeling. Plausible ages for the three basins were calculated to be 4.13, 4.09, and 3.88 Ga, respectively. There is abundant melt of the relatively young Imbrium and Crisium in the near surface, but local gardening by smaller impacts regionally diminishes the melt abundance; there is less Serenitatis melt in the near surface because of the burial of Imbrium and Crisium ejecta, but later impact events may build local melt-enriched zones by re-excavating the underlying melt.

The survival probability of basin melt at the Apollo and Luna sampling sites is quantitatively assessed in this study. The relatively young Imbrium melt might be abundant at Apollo 14-17 sampling sites with a fraction ranging from 0.3 to 0.6; Crisium melt could be found at Luna 20 and Apollo 17 sampling sites with a similar fraction about 0.05, each. The relatively old Serenitatis melt was exposed to heavy subsequent gardening, and its abundance should be much less or zero at these sampling sites. The observed prominent peak around 3.88 Ga, the lower values around 4.09 Ga, and the general absence around 4.13 Ga in the K-Ar isotopic ages from Apollo and Luna highland samples are consistent with our simulation results. We may therefore conclude that, particularly for the case of Imbrium, the clustered radiometric ages around 3.9–4.0 Ga for Apollo and Luna highland samples supports a sample bias, rather than the cataclysm scenario.

Our simulation results may be applied to predict the expected sampling of differently-aged melt in future sampling work. The area within a basin should possess a high fraction of basin melt, particularly for younger basins. The shallow surface might originally have abundant basin melt, but it could be strongly affected by the local impacts, buried by mare flooding, and diluted by

younger melt. Besides, the pulverized materials with fine grain size may be difficult to date using the current radiometric techniques. Pure basin melt is expected at greater depths within basins, which may be re-excavated by the more recent large impacts. This year's Chinese CE-4 mission that will land on lunar farside with a rover, should preferentially investigate deep-lying material. SPA melt might be found on the low-lying outcrops or near the rim of a later-formed large impact crater within a basin, such as Apollo or Von Kármán.

In the future, we intend to extend the model to consider ejecta movement in three dimensions to obtain a better view of the coverage and the abundance of basin melt in the present day. The abundance of differently-aged melt at some specific locations, especially sampling sites, is expected to be better estimated. It is expected to find new constraints on the impact rate function, and hence improve our understanding of the lunar bombardment history.

Acknowledgements: We gratefully acknowledge Carolyn van der Bogert and Tomokatsu Morota for their careful reviews of the manuscript and discussions with Alexander Basilevsky, Menghua Zhu, Robert Luther, Csilla Orgel and Natalia Artemieva. This work was supported by German Research Foundation (DFG) SFB TRR-170-1 TP A4. This is TRR-170 contribution 57.

5. Research paper II: Spatial diffusion of basin melt and its implications for sample interpretation

The following section has been published as: Tiantian Liu, Greg Michael, Kai Wünnemann, Harry Becker, and Jürgen Oberst (2019), *Lunar megaregolith mixing by impacts: spatial diffusion of basin melt and its implications for sample interpretation*, Icarus, 339, 113609, doi: https://doi.org/10.1016/j.icarus.2019.113609. The author contribution is explained in the section of "Structure of the dissertation". This paper presents the results using the 3D-model that is extended from the 2D-model.

Abstract

The formation ages of lunar impact basins are critical to understanding the late accretion history of the inner solar system. Furthermore, the correct interpretation of the provenance and isotopic dates of basin-derived impact melt ('basin melt') is essential for the calibration of lunar chronology function. However, abundances of basin melt in the lunar near-surface are not well understood. Basin melt has been gardened by a long sequence of subsequent impact events, altering its abundance and size distribution. We developed a numerical model to investigate this process by means of the Monte Carlo method in a spatially resolved model. The fraction of melt in ejecta was tracked globally and at the Apollo 14-17 and Luna 20 sampling sites and was compared with K-Ar age distributions of lunar impact melt breccias. It was found that melt produced by the very large SPA basin as well as the relatively late-forming Imbrium basin should be dominant in the near-surface (top one meter). The simulation shows that the melt component at the Apollo 14-17 and Luna 20 sites is strongly affected by nearby mid- to late-forming basins. Imbrium melt should be abundant in Apollo 14-17 samples; Crisium melt is the most significant component of basin-sourced melt in Luna 20 samples; all the Apollo 14-17 and Luna 20 samples could include melt from Serenitatis and the SPA basin; Nectaris melt should occur in Apollo 16, Apollo 17 and Luna 20 samples; and Orientale melt has no significant mixing in the Apollo 14-17 and Luna 20 sampling sites. In general, besides a prominent age peak at 3.9 Ga (related to the Imbrium basin), the model predicts pronounced abundance peaks of older basin melt (>3.9 Ga) which tend to be absent from distributions of K-Ar ages of impactites from landing sites. The diffusion characteristics of basin melt suggest that for future sampling aimed at collecting early basin melt, the re-excavation zones of late impact craters larger than tens of kilometer in diameter inside basins may provide the highest abundances of melt from early basins.

Keywords: Moon, surface; Regoliths; Impact processes; Cratering

5.1. Introduction

The lunar surface preserves a record of impacts in the inner solar system. Having a rigid crust and no atmosphere, its crater population is the best preserved among the solar system's planetary bodies, providing an essential record of late accretion in the inner solar system. Nevertheless, knowledge of the impact rate between 4.5 and 3.7 Ga, which may be related to different impactor populations, remains contested. Based on radioisotope ages (U-Pb system) of lunar samples that show clustered ages at ~3.9 Ga, Tera et al. (1974) suggested that there may have been an impact spike in the early lunar history ('lunar cataclysm'). This hypothesis was later further substantiated after larger numbers of K-Ar ages on impact rocks became available (Fernandes et al., 2013; Michael et al., 2018). The Nice model (Gomes et al., 2005; Morbidelli, Marchi, et al., 2012), which suggested that late migration of the giant planets could have destabilized part of the asteroid belt injecting projectiles into the inner solar system, was developed as a possible mechanism that might explain the occurrence of an impact spike. In contrast, based on studies of crater size-frequency distributions of surfaces in basins, Neukum (1983) and Hartmann (1995) argued that the Moon was hit only by one impactor population (the collisional remnants of planetesimals). In their view, the impact flux decayed monotonically and the dominant isotope ages of ~3.9 Ga just reflect sampling bias caused by the mixing of Imbrium ejecta.

The lunar basins can be used to constrain the impact rate in its early history if their ages are known. All lunar basins, including the youngest Orientale basin, formed before ~3.8 Ga by hypervelocity impact events. If the age of melt rocks that originate from a particular basin event can be determined reliably (e.g., by the K-Ar or other chronometers), it provides a calibration point for the lunar cratering chronology (Hiesinger & Head, 2006). Basin melt also provides information on the regional chemical makeup of the crust, possibly providing clues to the lunar differentiation history. In addition, determining the distribution of basin melt is significant for lunar exploration, being a prime target for future robotic or human sample return missions (Ryder et al., 1989).

Melt from a specific basin is affected by the long-term gardening processes by later impact events. Its volume and composition are changed by re-melting, and its spatial distribution is altered by entrainment in younger ejecta materials (Michael et al., 2018; Liu et al. 2019, the characteristics of melt evolving distribution are described in supplementary section 2). The lunar meteorites and the lunar highland rocks collected by the Apollo and Luna missions have provided some information on the abundance of impact melt both in an average sense and at specific sites. However, there remains a considerable level of ambiguity in the interpretation of the origin of lunar meteorites and returned samples (Spudis et al., 2011).

In this study, we developed a numerical model to investigate the diffusion of basin melt by impact gardening. We use "diffusion" to describe the movement of impact melt down its concentration gradient by repeated impact events. The aim is to provide a picture of the potential distribution of basin melt by using a new modeling approach, and thus provide clues for the interpretation of returned samples regarding which age distributions of basin melt should be expected at previous and future landing sites. These data may also be used to assess interpretations of isotopic age distributions in the literature and in future studies.

In section 5.2, we present the structure of the model. In section 5.3, the melt component in the near-surface both on a global scale and at specific sampling sites is estimated and compared with distribution patterns of K-Ar ages. The spatial distribution of melt from three mid- to late-basins (Serenitatis, Crisium and Imbrium) in variable proximity to lunar landing sites is also examined. In section 5.4, we describe the implications for the interpretation of collected lunar samples and discuss sources of uncertainties in the model.

5.2. The model

This paper is the third in a series investigating the cumulative melt diffusion by impact gardening. Michael et al. (2018) presented the surface-averaged model, where the volume of un-heated material and melt with different ages at different depth was traced. On this basis, Liu et al. (2019) investigated the diffusion behavior along a lateral path as well as by depth. Then, not only the distribution with depth, but also the lateral distribution along a path of a great circle was further recorded. This work extends the previous models, providing a more complete understanding of the melt evolving characteristics in three spatial dimensions, where the volume of unheated material and melt with different ages at all the depth over the global surface will be traced. We outline the main elements of the model here where we focus in particular on the new components of the model. Further detail is given in the Supplementary Material. In addition, in this model we do not consider the maria, because mare deposits cover parts of surface and occurred late, and hence would not significantly affect basin melt redistribution.

We used the Monte Carlo method to simulate the impact gardening process over the history of the observable surface of the Moon. The size-frequency distribution of generated craters conforms to the production function (PF) of Neukum (1983). The occurrence time of impacts was calculated combining the chronology function (CF) and PF (Neukum, 1983). The minimum crater diameter considered was chosen as 5 km. The transient crater size, D_t, was calculated based on scaling laws (McKinnon et al., 1997; Melosh, 1989). The volume of the generated melt markedly increases with D_t according to a power law (Cintala & Grieve, 1998). The thicknesses of both ejecta and melt decrease with distance from crater center (r in km) following a power law, but the fraction (i.e., concentration) of melt in the ejecta linearly increases with

distance (Liu et al., 2019; Melosh, 1989). We note that our model considers the re-melting of the excavated material for individual impact events, but the possible resetting of the K-Ar clock in hot ejecta blankets was not incorporated because the detailed behavior of the K-Ar system in feldspars from impactites is poorly understood. (See Liu et al. 2019 and supplementary section 5.6 for details).

Materials ejected from craters have high kinetic energy resulting in mixing with local materials on re-impact. The degree of mixing is expected to increase with distance from the ejection point. We considered such local mixing in this new model. Oberbeck et al. (1975) proposed a mixing ratio of local material to ejecta, $\mu = 0.0183r^{0.87}$. However, these values, particularly at larger scales, were suggested to be overestimated in comparison with laboratory cratering experiments (Peter H Schultz & Gault, 1985). The value of μ was thus modified by roughly half when μ is larger than 5.0: $\mu' = \mu/2 + 2.5$ (Petro & Pieters, 2006).

The model used point sets on a sphere to record the material component. The locations of these points were calculated based on the Fibonacci Lattice (González, 2010) to make them uniformly distributed on the surface. Each point was related to a cell. For each impact event, the points within tracing ranges (five radii of transient craters) will be found first. In each of these points, the melt volume, the total volume including both melt and un-melted component, and the thickness of ejecta (and melt lens within craters) will be recorded. When projecting the point set onto a plane, we used a Voronoi diagram (i.e., Thiessen polygon) to represent the cell of each point.

Because of the increasing number of deposition layers as the simulation progresses, the layer sequence was periodically simplified to one: 0.2×1.9^a m, where a = 0, 1, …, 20. While simplifying, all the material within set layers will be mixed together leading to a more average composition. The shallower layers are thinner to preserve a fine resolution of the melt component in the near surface; deeper layers are thicker yielding a more averaged composition.

5.3. Results

Lunar meteorites and the immediate source of current lunar samples are from the near-surface down to a few or tens of meters. Understanding the source and age distribution of the melt component in the surface layer is critical to our understanding of the lunar chronology, and key in the selection of future sampling sites. This study therefore focuses on the distribution of impact melt in the near-surface (top one meter).

5.3.1. Timing of basin-forming events

To investigate the melt distribution of the lunar impact basins, a model was created using both the known sizes and positions of the basins and randomly distributed craters smaller than 300

km. Thirty basin-forming events, the crater populations of which were reinvestigated using the buffered non-sparseness correction technique, are included in our simulations (Orgel et al., 2018). The buffered non-sparseness correction technique takes crater obliteration into account for the superposed crater densities, providing more accurate measurements of the occurrence times of basins (Riedel et al., 2018). Neumann et al. (2015) present a more complete list of lunar basins where some potential large lunar basins, such as Aestuum, Lamont, and Hertzsprung basins, are not included in the list in Orgel et al. (2018). The occurrence times of these basins, however, have not been calculated. They are therefore not included in this model. The erased structures of these basins indicate their early formation times. The consequences of excluding these basins are discussed in section 5.3.3.

Since the scaling laws used to calculate transient crater diameter (D_t, supplementary section 5.6.1) do not extrapolate well to basin sizes, we adopt the D_t values of 11 basins from Wieczorek & Phillips (1999) where the transient basin size was determined using gravity models. The D_t of the other basins was interpolated. The locations of the basins showing D_t and age is presented in Figure 23, and Table 4 presents the age, location and size of all the included basins.

It should be mentioned that the formation times of basins included in the simulations are taken as a plausible configuration of impact times and are not claimed as being in any way 'well known'. Our goal is to address the question "What are the consequences of such a configuration of impacts for the sample record?" and to use the comparison with the actual record of isotopic ages to inform our understanding of both the period and the process of basin melt migration into lunar impactite samples. The influence of an alternative sequence of basins will be discussed in section 5.4.3.

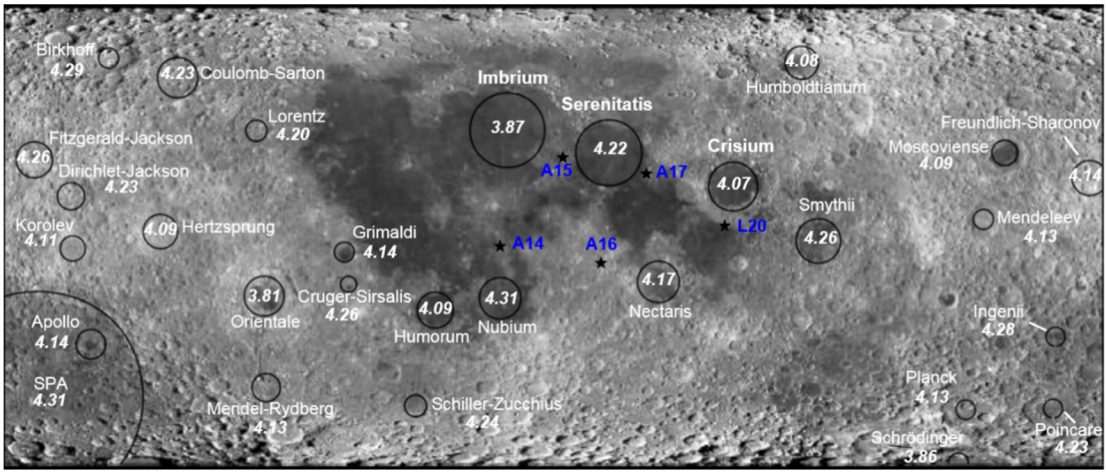

Figure 23 Map of basins. Circles mark the estimated transient cavities of 30 basins, and the numbers indicate their estimated ages (Orgel et al., 2018). Filled stars mark the locations of Apollo 14-17 (A14-17) and Luna 20 (L20) sampling sites. The background image is Lunar Reconnaissance Orbiter Camera (LROC) Wide Angle Camera (WAC) mosaic (<75° in latitude) (Robinson et al., 2010). The ages are based on recent work by Orgel et al. (2018).

Simulated impacts start slightly before the estimated formation time of the SPA basin at 4.31 Ga. In one simulation run there were 162517 impact events in total, including basin-forming events. Many older impacts have no significant influence on the present near-surface, since the majority of their melt was buried deeply by the ejecta of younger impacts. We improved the efficiency of the model by filtering out those impacts which we are certain to have negligible contributions to the near-surface melt abundance (the filtering procedure is described in supplementary section 3). After the filtering, 29176 impacts remain, while 133341 have been removed. As a consequence, the time for one run is decreased from five days to four hours. Of those removed, 96.9% are smaller than 30 km. Because of the greater impact flux during the early period, the majority of craters filtered out were old (Figure 30b), with 99.97 % being older than 3.5 Ga. The difference of the relative expected melt component at different depths is smaller than ~0.02, indicating that the features of melt component distribution are well-preserved by the filtering procedure.

5.3.2. Average melt component in the lunar near-surface layer

If lunar meteorites provide a spatially stochastic sample of lunar highland materials, the statistical radioisotope age record of melt-bearing impact rocks among lunar meteorites could reflect the average distribution of the melt component. We estimated the fraction of impact melt in the top one meter for comparison with the radioisotope age record (Figure 24).

The predicted distribution of melt with different ages is shown in Figure 24c. Basins are the main contributors of melt older than ~3.8 Ga. As indicated by the dashed arrows in Figure 24, the largest, SPA basin (~2500 km) is predicted to provide the most abundant melt in the near-surface; The late-forming Imbrium basin (~1320 km) is the second largest contributor of melt. Other basin events also left distinct traces: the melt of the youngest Orientale basin (3.81 Ga) is ~0.4× as abundant as Imbrium melt leading to the secondary peak at 3.81 Ga; several basins forming between 4.10 and 4.25 Ga generate a bulge during this period. To predict the contribution of basin-sourced melt, Table 6 presents volumes of melt from basins and smaller impacts. In general, younger basins leave more melt in the near-surface today.

We expect that there would have been basin-forming impacts prior to those which we are able to observe today (e.g., Neumann et al. 2015; Zhu et al. 2019). It can be expected that impacts occurring in the period between crustal solidification and the time of the presently observable oldest surfaces would leave a melt component, which could persist within the crust until now. These early impact events would heat and alter more crust material and the generated melt ought to leave a trace from depth up to the surface until the present day (see Michael et al. 2018). We recognize, however, that this material could be highly comminuted by impact

gardening and partially re-melted by younger impacts near the surface, which may leave it unrecognizable there (see further discussion in section 5.4.1).

During the last 3.0 Ga, the impact rate was lower and remains constant, melt diffusion is thus generally constant and the melt production is much less. Such a lower impact rate leads to a lesser amount of older melt being re-melted. Therefore, in the near-surface, younger impacts leave comparable quantities of melt to older basins, as indicated by relatively large impacts seen as random peaks in Figure 24c, such as those at 0.4 and 3.3 Ga.

Fernandes et al. (2013) compiled published K-Ar data and calculated the relative probability of $^{40}Ar/^{39}Ar$ impact ages from lunar meteorites, where 65 samples were included and the age was corrected for monitor age and decay-constant. Their plot is shown in Figure 24b. It is seen that, in the radioisotope age record of impact melt breccias in lunar meteorites (Figure 24b), there is abundant melt older than 3.5 Ga as expected, but less than expected with ages >3.8 Ga. In addition, in the distribution of isotopic dates (Figure 24b), the presence of melt from later impact events is more significant. The possible cause of these differences will be discussed in section 5.4.1.

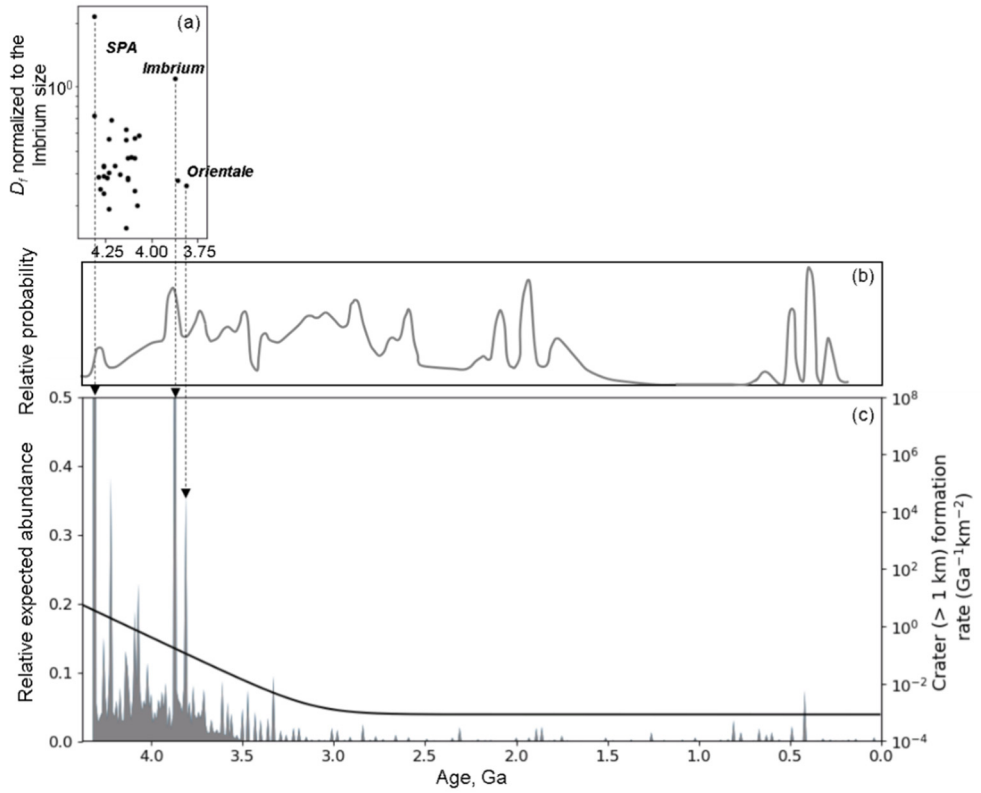

Figure 24 (a) Size distribution of basins normalized to the diameter of Imbrium basin. The formation times of SPA and Imbrium basin from Orgel et al. (2018) are $\mu 4.31^{+0.019}_{-0.021}$ $\mu 3.87^{+0.035}_{-0.046}$ Ga, respectively. (b) Relative probability plot of $^{40}Ar/^{39}Ar$ from 65 impact melt clasts in lunar meteorites (after Fernandes et al. 2013). The vertical scale is linear. The peak near 3.8 Ga is commonly interpreted to reflect the age of the Imbrium impact. (c) Fraction of melt component (i.e., relative melt abundance among all the generated melt) in the top one meter of lunar near-surface (left scale). The expected melt generated by SPA, Imbrium and Orientale basins are indicated by three vertical arrows. To show the small melt quantity from smaller impacts, melt fractions have been normalized to the absolute melt fraction derived from the second most abundant melt reservoir, the Imbrium basin (i.e., its relative abundance is equal to 1.0). The crater formation rate (right scale) shows that the high impact rate in the early lunar history is accompanied by a greater melt production. Note that if melt fractions were normalized to SPA melt fractions, the relative quantity of other melt fractions would be so small that specific distribution features are easily masked. Thus, the relative abundance of SPA melt fraction exceeds 1.0, and the exact value is not presented.

5.3.3. Present-day distribution of melt from basins formed between 4.2 and 3.8 Ga

Due to the weaker gardening after 3.0 Ga, abundant melt of basins formed between 4.2 and 3.8 Ga (mid- to late-forming basins) could survive in the near surface, and is thus very likely to be sampled. As representative examples, we present the global near-surface melt distribution of the Serenitatis, Crisium and Imbrium basins (Figure 25).

Besides the mare-related volcanism, which is not taken into account in this model, the only process that can significantly modify the distribution of basin melt is gardening by other basin-scale impact events. Smaller impact events can only re-melt small portions of older melt.

Because nearly no disturbance by younger basin forming impacts occurred, Imbrium melt is well-preserved and predominant in the near surface (Figure 25a). Imbrium ejecta covered the northwest part of Crisium ejecta, decreasing the abundance of Crisium melt in the near surface. Serenitatis is located between the Imbrium and Crisium basins (Figure 23). The excavation zones of both the Imbrium and Crisium basin exhumed the earlier Serenitatis ejecta. In the model, both the Crisium and the Imbrium ejecta entrained Serenitatis melt, transporting it to more distant locations. Therefore, the coverage of Serenitatis melt is almost equal to the merged zone of both Crisium and Imbrium ejecta (the main coverage by Imbrium and Crisium melt is outlined by a dashed curve in Figure 25). Nevertheless, the quantity of entrained Serenitatis melt is low. The average melt fraction from Imbrium is about ten times larger than from Serenitatis and double that of Crisium.

Subsequent smaller impact events garden the basin melt locally, making the distribution patchy. They diminish or even remove the melt from the excavation zones. The fraction of the basin melt entrained in the ejecta of smaller impacts depends on their scale and location. If an impact event is large enough to excavate older basin melt, it can form melt-enriched zones in the near-surface, especially if it excavates melt from the basin interior or the melt near the rim of the basin. Two regions enriched in Serenitatis melt are indicated by the black arrows in Figure 25c. Most smaller impacts occur on the ejecta areas of basins, excavating only a limited amount of basin melt and distributing it further, slightly reducing the proportion of basin melt in the near-surface. These zones are shown as faded red and yellow in Figure 25 a and b.

The results have some important implications for future sampling aimed at collecting the melt from these three basins. Within the range of several basin radii from Imbrium's center it is very likely to find its melt. Crisium melt could also be abundant but will be mixed with that of Imbrium within the Imbrium ejecta field. To limit the influence from the Imbrium basin, it would be better to collect samples from the eastern part of Crisium basin. Sampling Serenitatis melt without an admixture from other basins is difficult. It is the most widespread, but due to its low probability of preservation at the surface, re-excavation zones may be the best candidates for samples possessing a higher fraction of its melt. It should be noted that, most of regions within the basins were flooded by mare basalts, but if impact events penetrated mare basalts and excavated underlying impact melt, this basin melt should be the most abundant component in the ejecta, besides mare basalt.

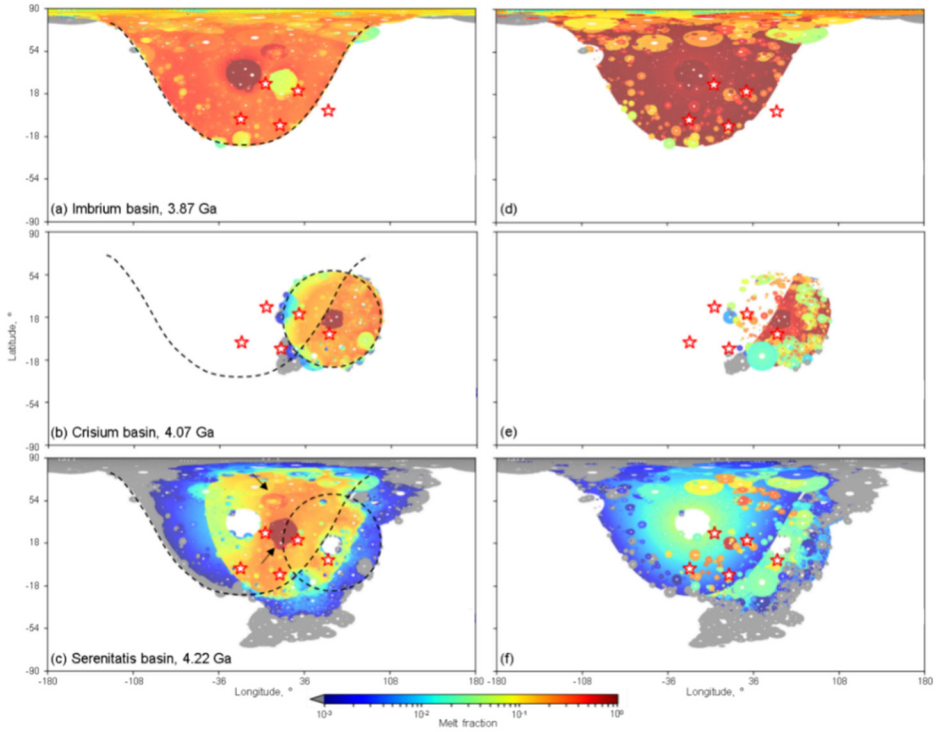

Figure 25 The global present-day distribution of melt from Imbrium (a), Crisium (b), and (c) Serenitatis basin in the near-surface (top five meters). Warmer colors indicate higher melt fractions (i.e., fraction of basin melt among all impact melt). Red stars indicate Apollo 14-17 and Luna 20 sampling sites. The main coverage of Imbrium and Crisium ejecta is indicated by the dashed regions. The black arrows in (c) indicate re-excavation zones of Serenitatis melt. (d)-(f) are the expected Imbrium, Crisium and Serenitatis melt abundances without local mixing processes.

5.3.4. Basin-sourced melt abundances at Apollo and Luna sampling sites

Without knowledge of their source, the context of lunar samples is difficult to evaluate. We calculated the probable fraction of basin-sourced melt in the near-surface at Apollo 14-17 and Luna 20 landing sites. These simulation results can be helpful for the interpretation of sample data and radioisotope ages in future work (Figure 26a-e). The volumes of melt from basins and smaller impacts are shown in Table 7. Note that, since no mare basalt or other late volcanic deposits are taken into account in this study, the following discussions concerning the fractions of basin melt do not consider admixtures of mare basalt which were found to be abundant in some returned samples (e.g., Shervais et al. 1985).

The melt component at these sites is strongly influenced by the ejecta of the youngest and closest basin. As seen from Figure 25, the Apollo 14-17 sampling sites were covered by Imbrium ejecta, and the Luna 20 samples were extensively mixed with Crisium ejecta. Therefore, impact melt components in the Apollo 14-17 samples are expected to be dominated by Imbrium melt. The fraction of Imbrium melt is expected to be ~1.0 in the melt with ages of 3.87 Ga (Table 6), which is suggested by its high relative abundance at 3.87 Ga in Figure 26 a-d highlighted by red color. Luna 20 samples would contain abundant Crisium melt with a

fraction of 0.92 in the melt with an age of 4.07 Ga (Table 6), indicated by the pronounced peak with this age (Figure 26e) highlighted by green color. Since both Imbrium and Crisium excavated the older Serenitatis material, all the Apollo 14-17 and Luna 20 samples should be mixed with at least some Serenitatis melt. Although the volume is small, Serenitatis melt is still the major contributor in melt with an age of 4.22 Ga (Table 6). Traces of the nearby older basin events should also be found in impactites collected near the surface, but their contribution would be small due to dilution by the later events. For example, Nectaris melt could be found at the Apollo 16-17 and Luna 20 landing sites (4.17 Ga in Figure 26c), but its quantity is small. The melt of the youngest Orientale basin has no significant mixing in the Apollo 14-17 and Luna 20 sampling sites.

Not all large peaks in the melt age distribution were derived from basins. Younger melt generated by smaller impacts (i.e., non-basin) also leaves traces, as those younger melts have experienced less gardening. Taking Luna 20 as an example, according to its location, the high quantity of melt at 3.87 Ga (Figure 26e) is derived from smaller impacts at this time, rather than a basin forming event. For the Apollo 14 sampling site, the model predicts only the peaks at 4.31 Ga, 4.22 Ga, 4.10 Ga and 3.87 Ga to be caused by basin forming events. Smaller impacts are randomly distributed over the lunar surface, and thus the simulation will not exactly match what is found at a specific site. The expected peaks caused by younger impacts are therefore different from some sample ages. This might also be the case for the record from lunar meteorites (Figure 24, Fernandes et al. 2013).

Michael et al. (2018) aggregated 117 K-Ar age measurements of Apollo 14-17 and Luna 20 impact melt breccias in highland rocks. The relative probability of K-Ar ages is plotted above each histogram in Figure 26. By comparing the expected melt abundance with the distribution of K-Ar radioisotopic ages, the issue of whether the peaks displayed in the radioisotopic ages is related to the basin forming events could be further evaluated.

Note that the recently proposed age of the Imbrium basin derived from U-Pb dates of phosphates in breccias from the Apollo 14 landing site is 3.9±0.02 Ga (Snape et al., 2016). Crisium age was proposed to be 3.95-3.85 Ga (Stöffler, 2006). The apparent age of the Imbrium basin (3.87 Ga) and Crisium basin (4.07 Ga) from crater size-frequency distribution (CSFD) and the Neukum (1983) chronology function, may be slightly inaccurate because of a combination of factors. Earlier decay constants used to calculate ^{40}K-^{40}Ar ages and ^{87}Rb-^{87}Sr ages during the 1970s and early 1980s are slightly different from recent determinations (Jourdan, 2012; Naumenko-Dèzes et al., 2018; Rotenberg et al., 2012). Furthermore, uncertainties of ages of neutron fluence monitors used in Ar-Ar dating and uncritical use of data from disturbed isochrons and complex Ar release spectra are additional biases on presumed basin ages that use isotopic dates and such biases also affect age distributions such as Figure

24 and Figure 26 (see Fernandes et al., 2013; Jourdan, 2012; Jourdan et al., 2009; Norman et al., 2010). In the following, we will use the 3.87 Ga age as representing the age of Imbrium, even though the true age may be 30-50 Ma older. The reasoning is that both age distributions (Figure 24 and Figure 26) and the impactor flux and basin ages used as a basis for our model were affected by the biases mentioned above.

We note that all isotopic age distributions from landing sites of the present study reveal the Imbrium peak of 3.87 Ga. However, additional 'age' peaks near 3.87 Ga are also sometimes present and may either result from smaller impact events or may reflect the presence of disturbed age spectra in the distributions. Both the Apollo 17 and Luna 20 sampling sites are expected to possess abundant Crisium melt (green histograms of 4.07 Ga in Figure 26), but the distribution of radioisotope ages does not display the corresponding peaks, and only few ages occur near 4.1Ga. If the proposed Crisium age of 3.95-3.85 Ga is taken (Stöffler, 2006), which is indicated by the semitransparent-green bars in Figure 26, the simulation results would be consistent with the radioisotopic dates shown as the peak of ~3.9 Ga. It may suggest that the melt of ~3.9 Ga in the Apollo 17 and Luna 20 samples could be mainly derived from the Crisium melt. If so, then the formation time of Crisium basin is more likely to be ~3.9 Ga which is close to the age of Imbrium basin, and the overlapping of semitransparent-red and green bars at ~3.9 Ga (Figure 26d) indicates that Apollo 17 samples may be a mixture of both Imbrium and Crisium melt.

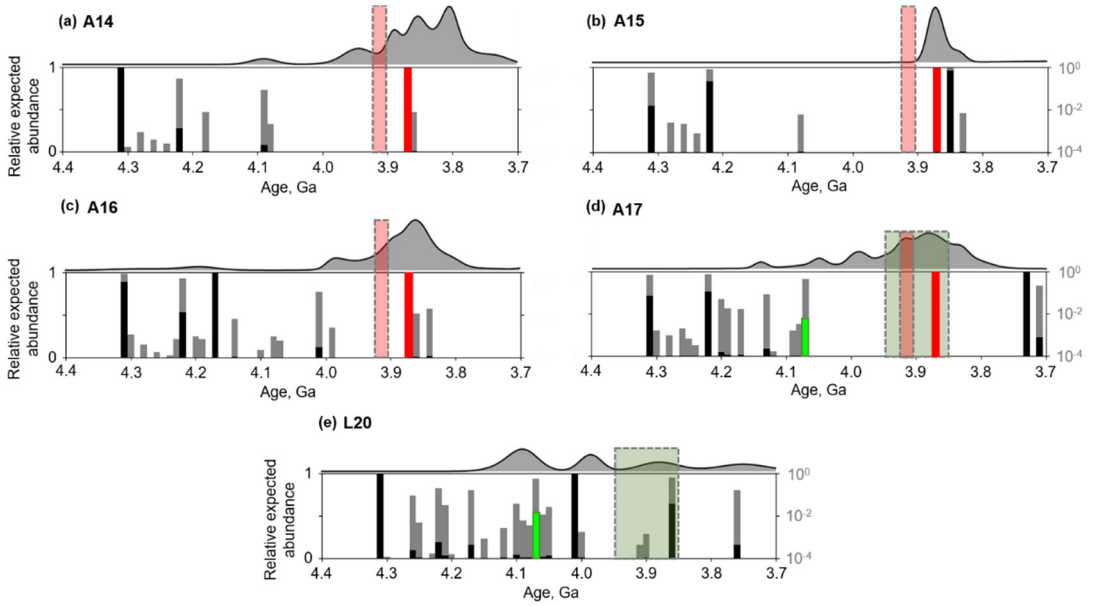

Figure 26 Relative distribution of K-Ar dates obtained on impact melt breccias at the Apollo 14-17 and Luna 20 sampling sites from samples (upper diagrams, Michael et al. 2018) in comparison with relative melt abundances at the Apollo 14-17 and Luna 20 sampling sites based on simulations (lower histograms; relative abundance among all the generated melt). The simulation data reflect melt abundances over a radius of 50 km at each landing site in the top 1 m of the near-surface. Model histograms are shown in black (absolute scale, left) and in grey (logarithmic scale, right). In the black histograms, the peaks caused by Imbrium (3.87 Ga) and Crisium (4.07 Ga) melt are highlighted by red and green color, respectively. Both ages were calculated based on the Neukum (1983) crater chronology and decay constants of that time, which are also the basis of the impactor flux used in our model (see text for further explanation). Note that Pb-Pb ages of phosphates suggest that the true age of the Imbrium basin is probably 3.92±0.02 Ga (the semitransparent-red bar, Snape et al., 2016). Stöffler (2006) suggested that Crisium-derived melt was 3.95-3.85 Ga (the semitransparent-green bars). Overall, the abundance of Imbrian 'ages' near 3.87 Ga at the Apollo landing sites agree with predictions from the model, whereas older K-Ar ages are much less common or do not occur (Apollo 15).

5.4. Discussion

5.4.1. Implications for the interpretation of melt provenance at lunar landing sites

The model predicts less young melt and more older melt (>~3.8 Ga) than implied by the K-Ar age distributions (Figure 24 and Figure 26). In addition, some of the expected peak values of melt abundance show different ages compared to the K-Ar age peaks. The main assumption in comparisons between age peaks in the model and published K-Ar ages is that the latter represents a statistical measure of the abundance of melt rock at the particular landing site and also globally. However, this assumption is not certain, and may be incorrect. A second assumption is that the model ages of basins are correct, but they could be inaccurate due to the inherent uncertainties in the lunar chronology function.

The radioisotope age distributions show prevalent younger melt rock. Many previous studies have investigated plausible causes of the apparent deficient of the old melt rock (Chapman et al., 2007; Cohen, 2000a; Hartmann, 1975; Zellner, 2017). It could be caused by the complete or partial Ar loss of older melt rocks and mineral clasts due to heating and shock, whereas inheritance of Ar from undigested older feldspar clasts in melt rocks might yield apparent ages that cannot be related to specific events (Korotev, 1994; Norman et al., 2006; Norman & Nemchin, 2014). Older clasts in melt breccias and their minerals may have been contaminated by younger (Imbrian) KREEP rich impact melt which may influence Ar budgets. In addition, older melt clasts may be less abundant than predicted because they were digested in large impact melt sheets or incorporated in warm ejecta blankets and all previously accumulated radiogenic Ar was lost because of degassing (Fernandes et al., 2013; Norman et al., 2006, 2010). Furthermore, as the grain size of melt rocks decreases with time due to gardening, older melt is more likely to survive near the surface in the form of tiny clasts or fine-grained minerals in breccia matrices. The larger clasts of melt rocks from younger basin forming impacts such as Imbrium may have been preferably chosen for dating, and thus young ages show up more frequently.

A significant number of published ^{40}Ar-^{39}Ar ages on lunar melt rocks or feldspars are based on perturbed age spectra, most of which do not satisfy current statistical tests for a point-like geological event (at least ~70% of the age spectrum (Cassata et al., 2009). Such samples may yield apparent dates that are shifted towards younger or older dates by tens and even hundreds of millions of years. A review of the geochronology of impact melt breccias by Grange et al. (2010) suggests that, when using strict data filtering (Jourdan et al., 2009), only a few tens of ^{40}Ar/^{39}Ar data of almost 300 sample analyses yield well-behaved and reliable age spectra (e.g. ^{40}Ar/^{39}Ar plateau ages given by Norman et al. 2006, Norman et al. 2010, and Fernandez et al. 2013). A better understanding of the chronology of major basin-forming impacts would require a much more systematic study of a larger number of samples, both from existing collections and from sample sets brought back by future missions.

Although a comparison of detailed aspects of the age distributions with the model results are difficult (e.g. the number of recorded impact events or ages of specific basins, Niihara et al., 2019; Norman et al., 2006) some robust general features may help to advance interpretations in future studies. According to our results, basin ejecta from the late-formed Imbrium and also the Crisium basin, should be the most significant components which should show up in the distribution in the K-Ar ages. In case of Imbrium, K-Ar ages near 3.87 Ga are common and match the model (Figure 26). For Crisium, a model age of 4.07 Ga could reflect data from some Apollo landing sites, whereas data from Luna 20 (which is closer to Crisium than the Apollo landing sites and relatively far away from Imbrium) would be more supportive of a relatively

young age (3.85-3.95 Ga; Stöffler, 2006). Both the model of ejecta ages and isotope age distributions at landing sites may be affected by locally produced impact melt from small impacts (see Figure 24 and Figure 26). Such biases may be evaluated by multi-chronometer studies of samples, combined with petrological and geochemical information. A key result of the data in Figure 26 is the absence (Apollo 15) or rarity of > 4.1 Ga old impact melt (i.e., melt from basins such as Serenitatis and South Pole Aitken) among isotope ages which is in contrast to the predicted minor abundance of such melt at the landing sites. As discussed above, this could reflect efficient loss of Ar from old melt clasts by younger heating events, biases during sampling of melt breccias, for instance if ancient melt rocks have a small grain size, or inaccuracies in our model.

5.4.2. Implications for future basin-melt targeted sampling

Linking the lunar samples to specific basins is a critical step in understanding the lunar history. Other than Imbrium, there is little consensus on which melt rocks or clasts retrieved from the Apollo and Luna missions were derived from specific basin events (Stöffler, 2006).

Theoretically, the best locations to collect basin melt would be the basin floor where the majority of melt is deposited after basin formation. However, old basins were mostly later filled with mare basalt, burying the impact melt by up to several kilometers.

Later impacts that are larger than tens of kilometer in diameter with excavation depths of several kilometers are likely to penetrate the mare basalt cover and form regional domains enriched with older melt rocks. Such impact craters are even more promising when located near the basin rim, because of the higher melt abundance there. For example, although the majority of Serenitatis melt was buried, the model predicts that there are still some regions in the near-surface possessing a large fraction of Serenitatis melt as indicated by arrows in Figure 25c. The potential for excavation of deeper ejecta blankets by young impacts has been also discussed in geochronological and geochemical studies of impactites from the Apollo 16 landing site. For instance, recent data support arguments that the 50 Ma old North Ray Crater excavated deeper stratigraphic ejecta units that were mainly derived from the Imbrium impact (Norman et al., 2010, 2016). Clast proportions, age distributions and geochemical characteristics in the deep units are different from the more shallow Cayley Plains Formation in that area, which is also interpreted to be Imbrium-derived (Norman et al., 2010).

The SPA region is also one of hot targets of future lunar missions (e.g., oft-suggested MoonRise mission). Figure 27 presents the predicted melt composition inside the SPA cavity (top one meter). Among all the generated impact melt older than 3.8 Ga, the SPA melt could be far more than those of later-formed impact events. In addition to the SPA melt, impact melts of Pointcare and Apollo basins would be the most prominent components regarding to the giant basin

forming events. In addition, due to the high impact flux in the early history, the impact melt of smaller impact events could also leave significant abundance until now, which would make the interpretation of surface material difficult.

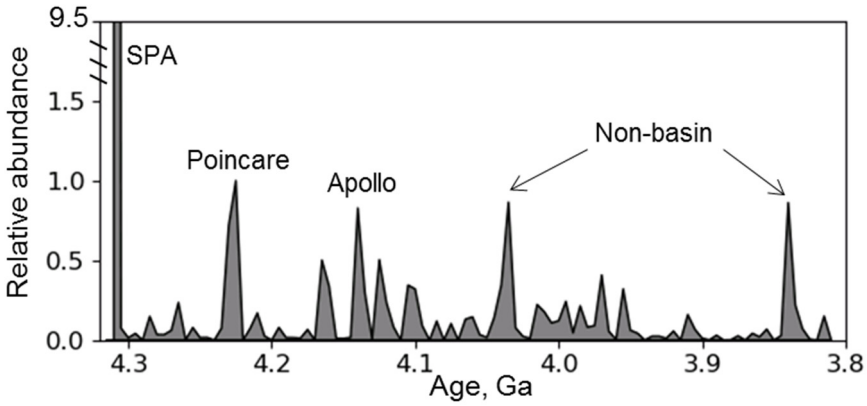

Figure 27 Predicted melt component in the top one meter within the SPA region.

5.4.3. Effects on model results of varying input parameters

To estimate the sensitivity of the model, here, we describe the effects of varying input parameters. For each tested parameter, we keep the other values as previously.

i. Melt produced in individual impacts

The scaling law applied to calculate the total volume of generated melt of individual impacts is derived from observations and numerical models for materials heated above melting point after release from shocked state (Cintala & Grieve, 1998). However, the K-Ar closure temperature of feldspars is significantly lower than the solidus temperature of basic lunar rocks, although the applicability of the closure temperature concept in rapid heating and cooling processes during impacts is uncertain. Therefore, the term “melt” used here should be regarded as “hot ejecta” that include all material heated above the K-Ar closure temperature of lunar rocks (Liu et al., 2019). The total volume of “hot ejecta” could be greater than of the estimate for “melt”. To check its influence, simulations with slightly (two times) and significantly (ten times) more melt production in each impact were performed. We found that (Figure 31 in supplementary material), in the top 500 m, when the melt of individual impact is two times more, the difference of relative melt fraction is generally smaller than 0.05, which results in ~15% difference of melt fraction compared with the result shown in Figure 24. When the melt of individual impact is ten times more, in the top ten meters, the difference of relative melt fraction compared with the result shown in Figure 24 is generally smaller than 0.1; at greater depth, the difference is larger, but is generally smaller than 0.2 compared with the result shown in Figure 24. In both cases, however, old basin melt, predominantly remains in the near-surface: it is not erased by later events

ii. Ejected melt volume

Only a minor portion of the generated impact melt would be ejected outside the craters. In this model, 75% of generated melt stays within the crater, with 25% being ejected. Simulations with instead 20% and 30% ejected melt of individual impacts were performed. The results (Figure 33 in supplementary material) show that, in the top 500 m, the difference of relative melt fraction is <~0.02, which results in ~10% difference compared with the result shown in Figure 24a.

iii. Sequence of basins

Although the sequence of lunar basins is roughly known, some basins display inconsistent sequences based on different measurement techniques (Fassett et al., 2012; Orgel et al., 2018; Stöffler, 2006). For example, in the past, the Nectaris basin was suggested to be older than Serenitatis basin, which contrasts with the results of Orgel et al. (2018). To test the influence of an alternative age sequence of basins, we assumed that Serenitatis formed after the Nectaris basin, the ages of other basins remaining unchanged. The simulation result shows that (Figure 34) the difference of the fraction of Serenitatis melt in the near surface in these different age models for Serenitatis and Nectaris is generally smaller than ~0.01. The major difference is the absent of Serenitatis melt surrounding the Nectaris basin since ejecta from the "early-formed" basin is unable to garden the "later-formed" Serenitatis melt. Therefore, given the general sequence of lunar basins, especially those formed during the mid- to late- period, the distribution of basin melt in the near surface would not be significantly changed but the melt abundance of early-formed basins surrounding the later-formed basins might be altered.

5.4.4. Other notable uncertainties in the model's prediction of the distribution of basin melt

The transient cavity sizes of basins are not well constrained, the estimates being diverse (Hikida & Wieczorek, 2007; Miljković et al., 2016; Potter, Kring, et al., 2012; Potts & von Frese, 2003). For example, the D_t of Imbrium basin has been estimated to be 744 km (Wieczorek & Phillips 1999) and 895 km (Hikida & Wieczorek 2007). However, although it would change the absolute abundances, the structure of the distribution of basin melt would not be changed (Liu et al., 2019).

In addition, the early Moon, during which time most basins were formed, is thought to have been much hotter than at later times (Laneuville et al., 2013). The higher internal energy leads to higher melt production since a warmer target requires less energy to melt (Zhu et al., 2017). The distribution of melt in the ejecta is also affected by the thermal state of the Moon. For a warmer target, Zhu et al. (2017) found that in a basin-forming impact, the melt fraction in ejecta material is almost constant with distance at ~20%. Therefore, on the younger Moon there might

be more basin melt near the surface leading to probably even more prominent abundance of these old basin melt in the near-surface (Liu et al., 2019). In addition, for the largest SPA basins, some ejecta may be lost close to five radii because of the high launch velocity.

The efficiency of melt diffusion is significantly influenced by the degree of mixing with local material during ejecta emplacement. As seen from Figure 25 d-f, without the consideration of this mixing process, the Imbrium melt in the near-surface would be much more abundant. In the western part of the Crisium basin, melt abundance would be reduced due to the coverage by Imbrium ejecta. The fraction of remaining Serenitatis melt would strongly decrease because of the coverage by both Crisium and Imbrium ejecta. Nevertheless, quantitative investigation of the entrainment of local material by ejecta needs to be further studied (Hörz et al., 1983; Zhu & Wünnemann, 2013).

Impacts forming craters smaller than 5 km in radii are not taken into account in this model. We expect that the gardening by these smaller impacts would reset the age of a component of the material and mix it to a more homogeneous state. We expect the older basin-derived components to remain essentially the same, minus this younger component.

Furthermore, our model did not take into account distal regions beyond five radii. Such processes lead to regional, melt-enriched areas (Hubbard et al., 1971). However, these processes are more sporadic and the volume is small. In addition, most impacts on the Moon occur with an oblique incidence angle. While resulting craters remain mostly near-circular (except for very shallow impact angles), the ejecta distribution can deviate more strongly from concentric symmetry: the ejecta of small craters are asymmetric only at distances where continuous ejecta blankets do not exist whereas the ejecta of large basins are asymmetric even near the crater rim (Shuvalov, 2011). Given the large number of the smaller impacts, the asymmetry distribution of ejecta will be averaged out, but the oblique impact angle may significantly affect the ejecta distribution of certain basins.

The formation process of the SPA basin is still not fully understood. The large melt volume, resulting from the higher internal energy, may have led to the formation of a deep and broad melt pool within the basin (Potter, Collins, et al., 2012). Our model may underestimate the global distribution of SPA melt, but SPA melt in the near surface should still be predominant on average (but not at landing sites close to Imbrium). However, melts with ages of 4.3 Ga are rare among landing site samples and possible reasons have been identified in the previous discussion. The lack of evidence for SPA melt could imply that there may have been more old basin-forming events that have not been identified.

5.5. Conclusion

The formation time of lunar basins is crucial for the study of late accretion in the inner solar system. To quantitatively understand the spatial diffusion of basin- and crater-derived impact melt, we developed a numerical model to simulate the long-term impact gardening process for a given impact flux scenario. The abundance and presence of impact melt with different ages, both globally and at specific Apollo and Luna sampling sites, were estimated and compared with K-Ar age distributions of impact melt breccias. Combined with the spatial distribution of basins, the probable distribution of basin-derived impact melt was discussed.

On a global basis, the estimated melt component in the near-surface shows, not unexpectedly, that impact melt from the SPA basin should be highly abundant. But very few melt rocks with isotopic ages of 4.3 Ga have been found among lunar samples. Imbrium-derived melt is also dominant in the near surface due to its late formation time and large size and here model and isotopic ages tend to match. Impact melt generated by the other basins was subject to cumulative gardening and thus the remainder in the near surface was significantly diluted, although melt from these basins is still quite abundant at depth. Older basin melt, especially from basins before 3.8 Ga, may have survived in the lunar meteorites, but the expected small fragments, resulting from long-term pulverization, make it difficult to investigate such impact melt clasts. In contrast, because of the low impact rate during the last 3 Ga, the melt of smaller impacts is more easily preserved and the clasts may still be intact, making the occurrence of young impactites more likely among lunar meteorites.

The estimated melt abundances at the Apollo 14-17 and Luna 20 sampling sites suggests that the regional impact melt component is closely related to the nearby basins (and occasionally nearby craters). Most of the collected samples at the Apollo 14-17 sites are likely to have been mixed with Imbrium melt, as suggested by previous radioisotope dating and geochemical studies. The model predicts that the modelled melt with an apparent model age of 3.87 Ga (based on the Neukum, 1983, chronology function), which appears to correspond to Pb-Pb phosphate ages of ~3.9 Ga (Snape et al., 2016), is almost all derived from the Imbrium basin. This result suggests that the K-Ar ages of impact melt breccias near 3.9 Ga in Apollo 14-17 samples represent the mixing of Imbrium melt with un-heated ejecta. In addition, the simulation results indicate that the formation time of Crisium basin could be close to Imbrium basin with the age of ~3.9 Ga as suggested by Stöffler (2006), and the impact melt of ~3.9 Ga in the Apollo 17 samples could be a mixture of both Imbrium and Crisium ejecta. The Luna 20 sampling site is close to the Crisium basin. We estimated the fraction of Crisium melt in the melt of 4.07 Ga (the CSFD model age of Crisium basin; or ~3.9 Ga, assuming the radioisotope age is correct) to be ~0.9.

All the Apollo 14-17 and Luna 20 samples should contain components of Serenitatis melt, but may not be mixed with the ejecta of the youngest Orientale basin. The melt of older surrounding basins, including SPA melt, also should occur, however, the content has been diluted by gardening. The Apollo 14, 16, 17 samples may also contain Humorum, Nectaris and Smythii melt, respectively. Little other basin-sourced melt is expected in the Apollo 15 samples than Imbrium, Serenitatis and SPA melt, however, only Imbrian K-Ar ages do occur. Luna 20 samples may contain Smythii and Nectaris melt. Other peaks observed in the K-Ar age distributions more likely derive from smaller-scale impact events or reflect disturbed Ar-Ar systematics.

Acknowledgments: We acknowledge discussions about cratering processes and formation of impact melt with Menghua Zhu, Lukas Manske, and Robert Luther. We thank Wilhelm Zuschneid for proof-reading and many helpful suggestions. This work was supported by German Research Foundation (DFG) CRC TRR 170, subproject A4. This is TRR 170 contribution 82.

5.6. Supplementary material

In this supplementary file, we present detailed description of the model structure, the characteristics of melt diffusion, the filtering procedure of inconsequential impact events, and effects from the varying input parameters. In addition, the involved basins are presented in Table 5 and the calculated volume of basin-sourced melt in the near-surface globally and at Apollo 14-17 and Luna 20 landing sites is also summarized (Table 6 and Table 7).

5.6.1. Essence of the model

We use the Monte Carlo method to simulate the impact gardening process. The size-frequency distribution of generated craters conforms to the production function (PF). The occurrence time of impacts is calculated combining the chronology function (CF) and PF (Neukum, 1983). The minimum crater diameter considered is chosen as 5 km.

In the model, an excavation depth, d_{exc}, is approximated to one third of the transient crater depth, d_t, which corresponds one tenth of the transient crater diameter (D_t). The transient crater diameter is related to the morphology of the final crater: for simple craters, $D_t = 0.8D$ (Melosh, 1989), where D is the rim-to-rim distance of final craters; for complex craters, $D_t = (D\mathrm{D_Q}^{-0.13}/1.17)^{1/1.13}$ (McKinnon et al., 1997), where $\mathrm{D_Q}$ is the simple-complex transition diameter, and taken as 21 km (Pike, 1977). The volume of the excavated materials, V_{exc}, is estimated to be 1/3 of a disc with d_{exc} in thickness and D_t in diameter. The total volume of the generated impact melt with a reset age as the current model time is: $V_{melt} = 1.4\times10^{-4}D_t^{3.85}$ (Cintala & Grieve, 1998). About 75% of V_{melt} stays inside the crater, and about 25% of V_{melt} is ejected (Liu et al., 2019).

The majority of excavated materials deposit within 2-3 radii of transient craters from crater center in the form of ejecta blankets, which are followed by patchy zones spanning about three radii. Continual ejecta blankets and patchy zones encompass most of the total ejecta (about 85%). Therefore, we only trace the melt within five radii of transient craters. To conserve mass, the remaining 15% ejecta materials are also taken to be deposited within this range. In the model we assume the ejecta materials within the five radii from the crater center form a continuous layer. The thickness of ejecta layers, δ, decreases with distance from crater center, r, (Melosh, 1989):

$$\delta(r) = Ar^{-3} \quad (1)$$

where A (km^4) varies for differently-sized craters to conserve mass and is calculated by taking the integrated volume within five radii exactly to be V_{exc}. The thickness of melt, δ_m, also decreases with r but with the shallower slope (Liu et al. 2019):

$$\delta_m(r) = A_m r^{-2} \quad (2)$$

Note, melt in the ejecta does not occur as a distinct layer, actually, but is distributed over the entire thickness of the ejecta layer. $\delta_m(r)/\delta(r)$ represents the melt content in the ejecta layer (i.e., the fraction of impact melt) at a given distance r. Similar to A, A_m (km^3) also varies for differently-sized craters and is estimated by taking the integrated volume within five radii exactly to be the melt volume that is ejected from the cavity.

To record the evolving melt component, the model uses point sets that are nearly uniformly distributed on a sphere. This simplifies the calculation of the integrated ejecta volume over the spherical body and avoids the bias caused by the surface curvature. Assuming a total of N points on the lunar surface, the spheroidal coordinates of the i-th point (x_i, y_i, z_i) can be obtained using the Fibonacci Lattice (González, 2010):

$$\begin{cases} z_i = R(2i-1)/N - R \\ x_i = \sqrt{R^2 - {z_i}^2}\cos(2\pi i \emptyset) \\ y_i = \sqrt{R^2 - {z_i}^2}\sin(2\pi i \emptyset) \end{cases} \quad (3)$$

where R is the radius of the Moon and $\emptyset = \left(\sqrt{5}-1\right)/2 \approx 0.618$, the golden ratio. As an example, Figure 28 presents an example of 1000 points distributed over the lunar surface.

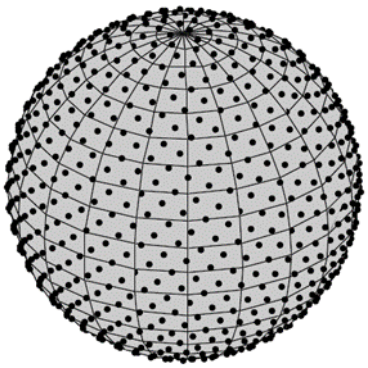

Figure 28 Example of 1000 points that are evenly distributed on a sphere using a Fibonacci lattice.

Each point is related to a cell for which the melt composition is tracked. For each impact event, we first determine the points that are covered by the ejecta (i.e., five radii). Then the fraction of ejecta, *f*, deposited in each cell is calculated. To conserve the total mass, the sum of all the fractional values is ensured to be 1. Therefore, the ejecta volume that falls on the *i*-th cell, V_{ei}, is the product of V_{exc} and f_i, where f_i is the fraction of V_{exc} in the *i*-th cell. In order to preserve the melt fraction in ejecta, the equivalent distance from the impact center, l_i', is estimated based on the integrated volume (eq.1) over two nearest points, *i* and *i*+1:

$$l'_{i+1} = 2\pi A l'_i / (2\pi A - V_{ei} l'_i) \quad (4)$$

For the nearest point to the crater center, l_i' (i=1) is equal to Rt; for the other points, l_i' (*i*>1) can be determined iteratively by substituting li-1' into eq.4. The melt volume, V_{mi}, and the average ejecta thickness, δ_i', stored in the i-th point are calculated using the integral of eq.1 and eq.2:

$$V_{mi} = 2\pi A_m (\ln(l'_{i+1}) - \ln(l'_i)) \quad (5)$$

$$\delta'_i = \frac{A\left(l'^{-2}_{i+1} - l'^{-2}_i\right)}{2(l'_{i+1} - l'_i)} \quad (6)$$

When projecting the point sets onto a plane, we use a Voronoi diagram (i.e., Thiessen polygon) to represent the area of each cell. In a Voronoi diagram, a plane is partitioned from a set of generating points into convex polygons such that each polygon contains exactly one generating point and every location within a given polygon is closer to its generating point than to any other.

5.6.2. Characteristics of impact gardening

Once melt is generated on the lunar surface, it is exposed to the long-term gardening processes by later impact events. It can be depleted by re-melting, transported to farther places by excavating, and buried by younger ejecta materials. Buried melt can also be re-excavated to the

surface if subsequent impact events are large enough. Figure 29a-f shows the migration of the melt generated by the first impact in a sequence where all the impact events have the same D_t of 50 km.

Initial distribution: As seen from the inset figure of Figure 29a, when just formed, a large amount of the melt stays inside the crater and the majority of the ejected melt deposits within about two radii from the crater center generating a melt-enriched zone. More distant locations possess much less melt.

Transportation: Through subsequent impacts (Figure 29b-f), the melt is transported to more distant places. When the melt has been gardened 10, 30, 50, 100 and 150 times, the coverage of the melt becomes about 2.5, 6.5, 11, 24, and 32 times larger than the original (Figure 29a). The majority of the melt remains in/around the original melt-enriched zone. Farther from the impact center, the redistributed melt quickly diminishes in concentration, falling to a fraction less than 10^{-3}.

Depletion: Re-melting depletes the presence of older melt. During each gardening event, the volume of the re-melted material is equal to the volume of the newly generated melt of the impact event. 25% of the re-melted melt would be ejected; and the remainder would stay within the cavity. Figure 29g shows the total remaining melt from the first impact after the gardening sequence. The arrows labeled as “a”, “b”, “c”, “d”, “e” and “f” point out the melt volume of Figure 29 a to f, respectively. After 195 gardening events, 2.6% of the melt has been re-melted. The majority of the depletion is caused by the first 30 impacts when most of them gardened the melt-rich area: the first ten and 30 impacts re-melted about 1.0% and 2.1% of the total melt, respectively. After the melt was distributed over a larger area, more later impact events occurred in areas that contain only a small fraction of the melt of the first impact (grey areas in Figure 29 b-f), causing less re-melting. The rate of depletion thus slows, as shown by the two terraces in Figure 29g. For example, the last 90 impacts that occurred outside the melt-enriched zone, only reduce the melt by ~0.05 km^3. If an impact occurs in the melt-enriched area, the remaining total melt would decrease more substantially, as seen around the 75^{th} event in Figure 29g.

Burial: As more ejecta are emplaced, the melt from the first impact becomes more deeply buried. Figure 29h shows the variation of melt volume with depth as gardening proceeds. At the beginning, about 6% of the melt occurs in the upper 50 m; after the first 30 impact events, there is 4% more melt buried below 50 m, indicated by the ‘P’ in Figure 29h. After 150 gardening events, the fraction of melt buried deeper than 500 m increases from 38% to 73%.

Re-excavation: The buried melt can be re-excavated enriching the near-surface. As seen from Figure 29h, some later impact events dug out more deeply buried melt increasing the abundance at the surface indicated by the “V” in Figure 29h. The ten gardening events after “P” re-excavate

~10 km^3 melt to the upper 50 m. Some melt-vacant zones resulting from the excavation process, like "va" in Figure 29b, were refilled indicated by "rf" in Figure 29c. At about the 160th impact, another sequence of re-excavation event occur.

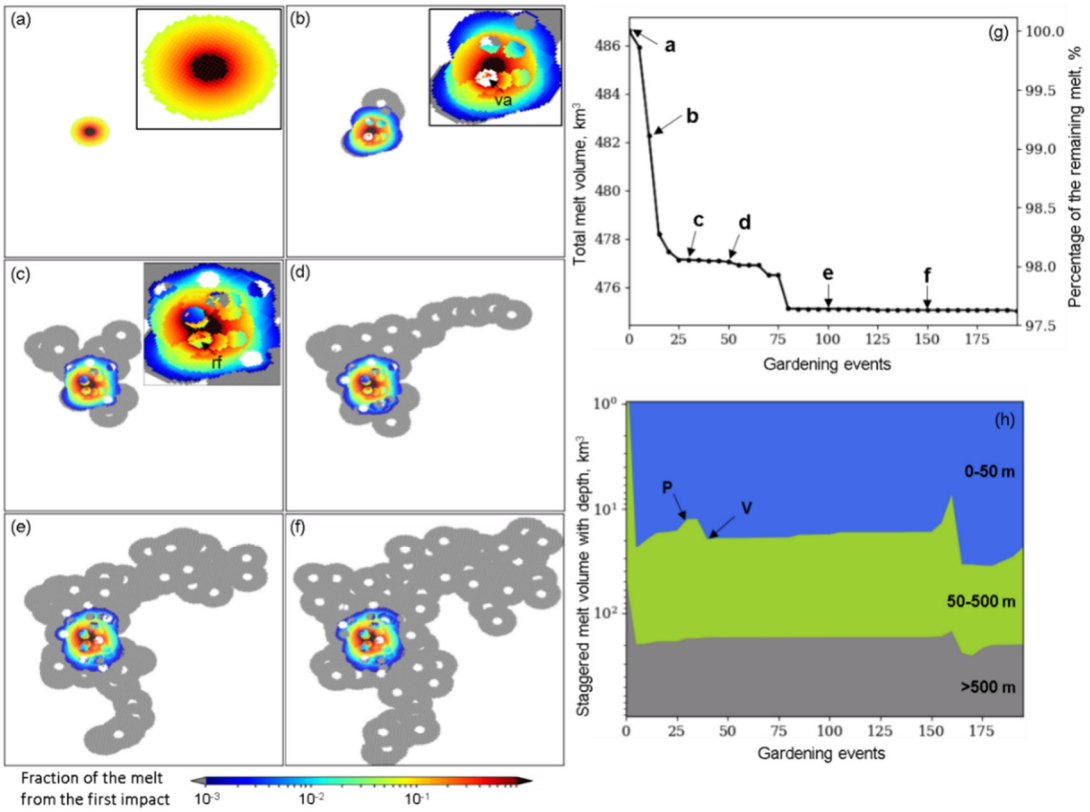

Figure 29 The migration of the melt generated by the first impact event, where the Dt of all the simulated craters is 50 km. Panels (a) to (f) show the spatial distribution of melt of the first impact after it was gardened by 0, 10, 30, 50, 100 and 150 impact events. Warmer colors indicate a higher melt volume, and grey areas indicate a melt fraction of less than 10-3. The initial distribution of melt from the first impact is shown in detail in the inset of (a). The melt is distributed over a larger area by the impact gardening, but the majority is still located close to where it formed. The melt vacant zone "va" in the inset of (b) results from the excavation process. The melt is redistributed over "va" indicated by "rf" in the inset of (c). (g) The decreasing total volume of melt from the first impact (left scale) and the percentage of the remaining quantity (right scale). The arrows indicate the total melt volume at the stages (a) to (f). (h) The evolving melt abundance with depth, where blue, green, and grey colors represent the top 50 m, 50-500 m, and deeper than 500 m, respectively. If the melt-enriched region is gardened, especially the cavity of the first crater, the melt abundance of the top layer can decrease, such as at the time labeled "P". The mark "V" indicates a re-excavation event bringing buried melt back to the surface.

5.6.3. Filtering out inconsequential impact events

Many older impacts have no significant influence on the present near-surface, since the majority of their melt was buried by the ejecta of younger impacts and thus deeply seated. We can improve the efficiency of the model by filtering out those impacts which we are certain make negligible contribution to the near-surface melt abundance.

Inconsequential impacts can be filtered out based on their formation times, locations and sizes. The youngest impact is first considered. If older markedly smaller craters are located beneath its ejecta, they can be neglected. This procedure is repeated for all craters which survived the previous filtering step, until no more craters can be removed. Figure 30 shows the schematic of the filtering process. Before filtering, there are eight craters with different sizes, where the small craters are more frequent. The numbers indicate the formation sequence of the craters, starting with the oldest. The youngest crater "8" is considered first. The older and smaller craters located beneath its ejecta are filtered out (craters "6" and "7" in Figure 30a). Then, the 2nd youngest crater "5" of the remaining craters ("8", "5", "4", "3", "2", and "1") is considered. Its greater size results in larger ejecta blanket. More older craters are buried (i.e., craters "1", "3" and "4" in Figure 30b). Then the 3rd youngest remaining crater "2" is considered. Its ejecta blanket does not cover any craters, and hence no older crater is filtered (Figure 30c). After filtering, only craters "2", "5" and "8" are deemed to have significant influence on the melt component of the near surface (Figure 30d).

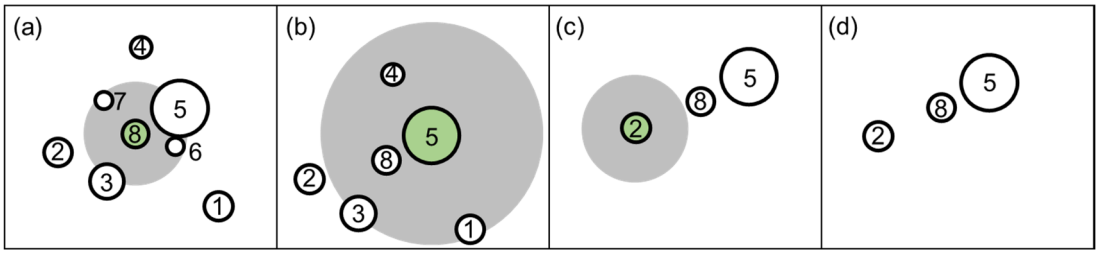

Figure 30 Schematic example of the filtering method to remove inconsequential gardening events. The considered impact is highlighted in green; its continual ejecta region in grey. Filtering steps (a) to (d).

The filtering procedure is related to the considered size of removed craters, and the rational results must not alter the distribution of the melt component significantly. Removing craters much smaller than the considered impact results in more remaining impact events and preserves the melt distribution but weakens the function of filtering procedure. On the opposite, if all impacts that are smaller than considered impact and located inside the ejecta region are removed, the melt composition in the near surface would be significantly different. The rational value of the ratio of Dt of considered crater to that of the remaining craters is found to be one-tenth. Figure 31 illustrates the effects of filtering on the size and age distribution of craters and the corresponding difference of the melt component. Of the 162517 impact craters, 29176 remain after filtering, while 133341 have been removed. Of the removed craters, 96.9% are smaller than 30 km and no crater is larger than 100 km (Figure 31a). Because of the greater impact flux during the early period, the vast filtered craters were old (Figure 31b), where 99.97 % of the removed craters were older than 3.5 Ga. Figure 31c shows the absolute difference of the relative expected melt component at different depths after filtering. The difference is smaller than ~0.02

and decreases with decreasing age and increasing depth. The small difference indicates that the features of melt component distribution are well-preserved by the filtering procedure.

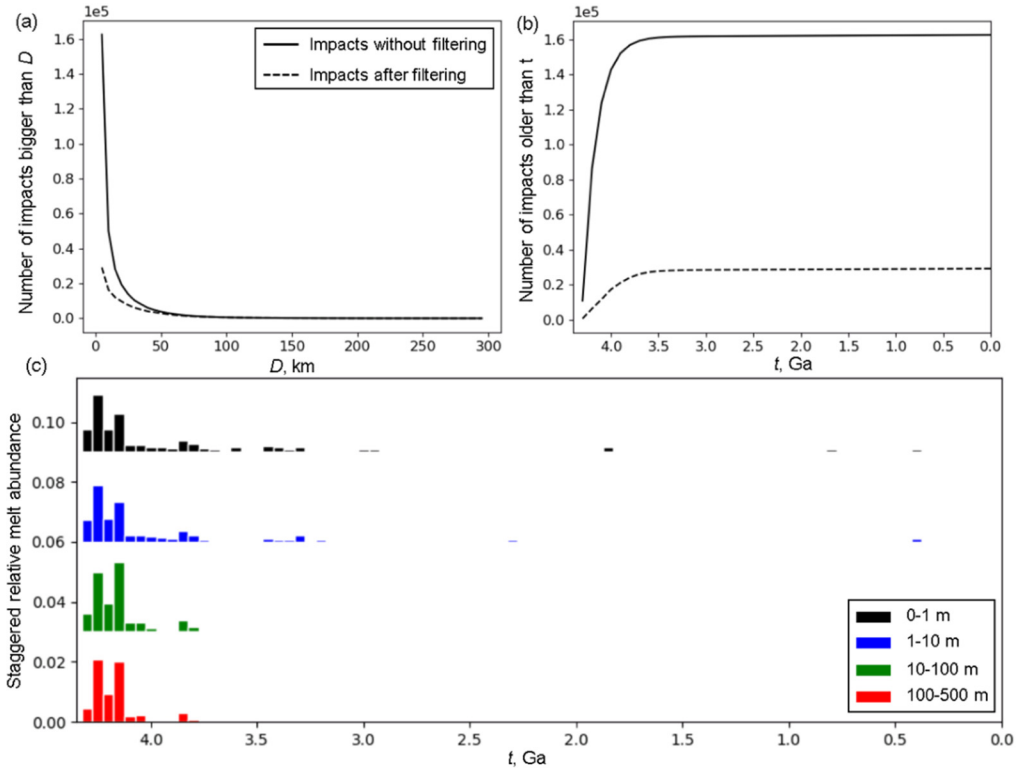

Figure 31 Comparison of the distribution of impact events after filtering. (a) Cumulative distribution of differently sized and of (b) differently-aged craters. The solid and dashed lines represent impacts before and after filtering. (c) Staggered relative melt abundance at various depths after filtering procedure.

5.6.4. Effects on model results of varying input parameters

More simulations are performed to test the sensitivity of the model. Figure 32 and Figure 33 show the relative difference of the fraction of differently-aged melt while altering melt production and the percentage of ejected melt in individual impacts, respectively. To investigate the influence from the basin stratigraphy, the formation time Serenitatis and Nectaris basin is exchanged. Figure 34 shows the corresponding melt abundance of Serenitatis basin in the near surface.

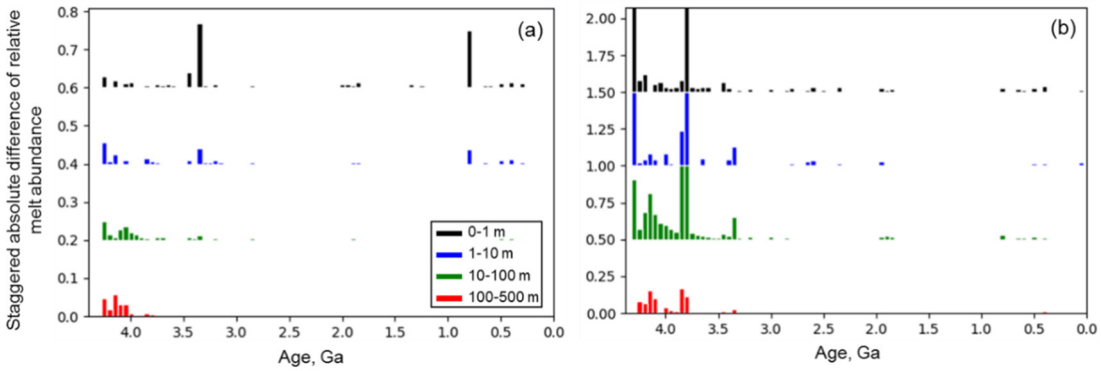

Figure 32 Staggered absolute difference of relative melt abundance at various depths when two times (a) and ten times (b) more melt is produced in individual impacts.

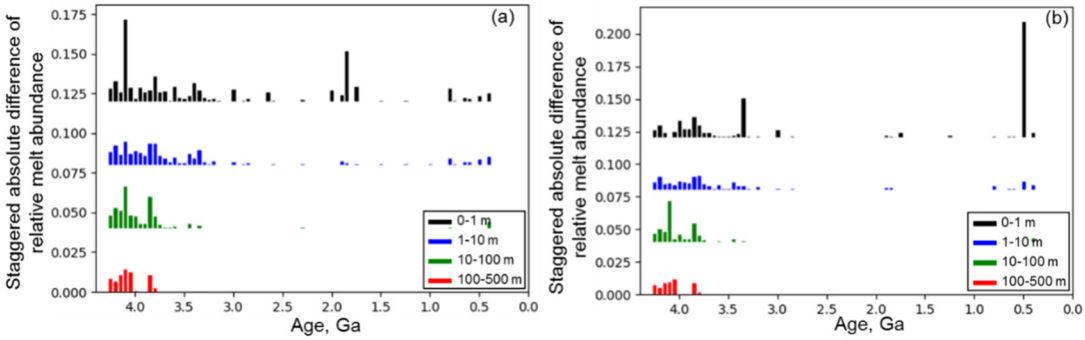

Figure 33 Staggered absolute difference of relative melt abundance at various depths when 5% less (a) and 5% more (b) melt is ejected during the formation individual impacts.

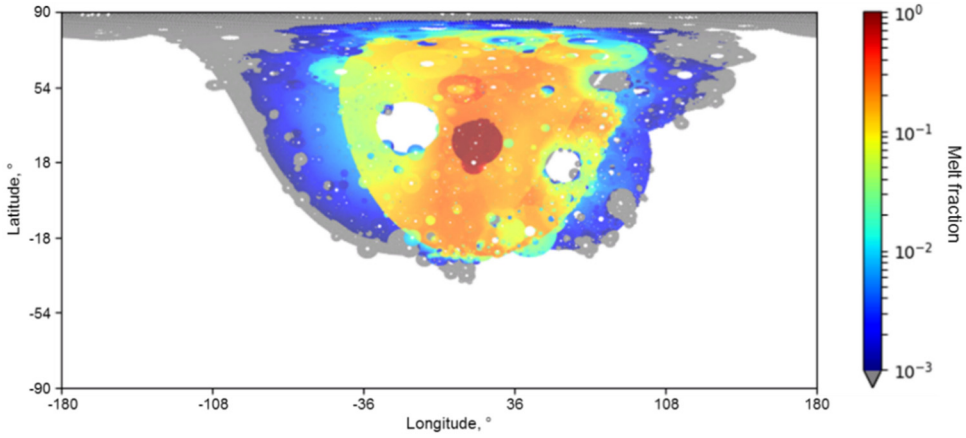

Figure 34 The global present-day distribution of melt from Serenitatis basin in the near-surface (top five meters) when Serenitatis basin forms later than Nectaris basin.

Table 5 Location, size and age of the included basins.

Basin[1]	Longitude,°	Latitude,°	D_f, km^2	D_t, km^3	Age, Ga[4]
South Pole-Aitken	-169	-53	2500	2099	4.31
Nubium	-17	-21	690	414	4.31
Birkhoff	-146	58	330	200.4	4.29
Ingenii	165	-33	320	189	4.28
Amundsen-Ganswindt	123	-81	340	201	4.26
Cruger-Sirsalis	-67	-16	270	160.8	4.26
Smythii	87	-2	880	443	4.26
Fitzgerald-Jackson	-170	25	600	360	4.26
Schiller-Zucchius	-45	-56	360	216.6	4.24
Dirichlet-Jackson	-158	13	450	271.2	4.23
Coulomb-Sarton	-123	52	670	403.2	4.23
Poincare	164	-57	310	187.2	4.23
Serenitatis	18	27	920	657	4.22
Lorentz	-97	35	350	210.6	4.20
Nectaris	35	-15	890	414	4.17
Grimaldi	-68	-5	460	198	4.14
Freundlich-Sharonov	176	19	580	349.2	4.14
Apollo	-151	-36	490	295.2	4.14
Mendeleev	141	5	330	198.6	4.13
Planck	135	-57	320	192.6	4.13
Mendel-Rydberg	-94	-50	650	281	4.13
Korolev	-157	-4	420	250.2	4.11
Humorum	-39	-24	820	358	4.09
Hertzsprung	-129	1	570	342.6	4.09
Moscoviense	148	27	420	252.6	4.09
Humboldtianum	82	57	620	331	4.08
Crisium	59	16	1080	487	4.07
Imbrium	-15	35	1320	744	3.87
Schrödinger	133	-75	330	195.6	3.86
Orientale	-95	-20	940	397	3.81

1 Thirty basins involved in Orgel et al. (2018); 2 Measured final diameter (Michael et al., 2018); 3 Eleven Dt values of basins are derived from Wieczorek & Phillips (1999) where the transient basin size was determined using gravity models, and the other basins was interpolated; 4 Orgel et al. 2018.

Table 6 Abundance of melt from basins in the top one meter, where the total volume of materials including both melt and un-melted component is 3.8×10^4 km^3.

Time, Ga *	Basins	Melt volume, km^3		Fraction of basin melt**
		Named basin	other	
>4.3	South Pole-Aitken, Nubium	6625	115	0.98
4.25 – 4.30	Birkhoff, Ingenii, Amundsen-Ganswindt, Cruger-Sirsalis, Smythii, Fitzgerald-Jackson	563	748	0.43
4.20 – 4.25	Schiller-Zucchius, Dirichlet-Jackson, Coulomb-Sarton, Poincaré, Serenitatis, Lorentz	1677	663	0.72
4.15 – 4.20	Nectaris	256	644	0.29
4.10 – 4.15	Grimaldi, Freundlich-Sharonov, Apollo, Mendeleev, Planck, Mendel-Rydberg, Korolev	862	718	0.55
4.05 – 4.10	Humorum, Hertzsprung, Moscoviense, Humboldtianum Crisium,	1674	728	0.70
3.85 – 4.05	No basin			
3.85 – 3.90	Imbrium, Schrödinger	4804	3829	0.56
3.80 – 3.85	Orientale	2249	1378	0.61

*Note: Basin ages are from Orgel et al. (2018) and are based on the lunar chronology function from Neukum et al. (1983). ** Fraction of basin melt among all the generated melt with ages within in the time interval

Table 7 Abundance of melt with given age interval and its basin-sourced fraction (top one meter) over the Apollo 14-17 and Luna 20 landing region with 50 km in radii from the sampling sites, where the total volume of material both melt and un-melted component is 25 km^3.

Age bin, Ga [a]	Basin	Apollo 14			Apollo 15			Apollo 16		
		$V_{m\text{-}bin}$, km^3 [b]		f_b [c]	$V_{m\text{-}bin}$, km^3 [b]		f_b [c]	$V_{m\text{-}bin}$, km^3 [b]		f_b [c]
		Named basin	Other		Named basin	Other		Named basin	Other	
4.300	South Pole-Aitken Nubium Birkhoff	7.87	0	**1.00**	1.89	0	**1.00**	6.22	0	**1.00**
4.275	Ingenii	0	0.01	0	0	0.01	0	0	0.01	0
4.250	Amundsen-Ganswindt Cruger-Sirsalis Smythii Fitzgerald-Jackson Schiller-Zucchius	0	0.01	0	0	0.01	0	0	4E-3	0
4.225	Dirichlet-Jackson Coulomb-Sarton Poincaré	0	0.04	0	0	0	0	0	0	0
	Serenitatis	2.14		**0.98**	1.44		**1.00**	3.75		**1.00**
4.200	Lorentz	0	2.21	0	0	1.44	0	0	3.76	0
4.175	Nectaris Grimaldi Freundlich-Sharonov	0.0	0.03	0	0	6E-5	0	3.50 0	0.01	**1.00** 0
4.150	Apollo	0	6.43	0	0	6E-6	0	0	3.53	0
4.125	Mendeleev Planck Mendel-Rydberg	0	1E-4	0	0	8E-5	0	0	0.02	0
4.100	Korolev Humorum Hertzsprung Moscoviense	0.32	0	**1.00**	0	8E-5	0	0	2E-3	0
4.075	Humboldtianum Crisium	0	0.33	0	0	0.01	0	0 0.0043	0.005	0 0.46

3.875	Imbrium	5.04	0.03	**0.99**	1.85	0	**1.00**	5.97	0.04	**0.99**
3.850	Schrödinger	0	5.07	0	0	3.51	0	0	6.08	0
3.800	Orientale	0	0	0	0	0.01	0	0	0	0

Table 7 Abundance of melt with given age interval and its basin-sourced fraction (top one meter) over the Apollo 14-17 and Luna 20 landing region with 50 km in radii from the sampling sites, where the total volume of material both melt and un-melted component is 25 km^3 (continued).

Age bin, Ga [a]	Basin	**Apollo 17**			**Luna 20**		
		$V_{m\text{-}bin}$, km^3 [b]		f_b [c]	$V_{m\text{-}bin}$, km^3 [b]		f_b [c]
		Named basin	Other		Named basin	Other	
4.300	South Pole-Aitken Nubium Birkhoff	1.64	0	**1.00**	3.28	0	**1.00**
4.275	Ingenii	0	0.01	0	0.27	0	0
4.250	Amundsen-Ganswindt Cruger-Sirsalis Smythii Fitzgerald-Jackson Schiller-Zucchius	0.0037	0.0043	**0.46**	0.27	0.08	**0.97**
4.225	Dirichlet-Jackson Coulomb-Sarton Poincaré	0	0	0	0	0.1	0
	Serenitatis	1.75		**1.00**	0.56		**0.85**
4.200	Lorentz	0	1.85	0	0	0.65	0
4.175	Nectaris	0.14	0.07	**0.68**	0.23	0	**1.00**
	Grimaldi	0		0	0		0
	Freundlich-Sharonov						
4.150	Apollo	0	0.04	0	0	0.23	0
4.125	Mendeleev Planck Mendel-Rydberg	0	0.10	0	0	0.01	0
4.100	Korolev Humorum Hertzsprung Moscoviense	0	0.10	0	0	0.12	0

4.075	Humboldtianum Crisium	0 1.03	0.0	0 **0.99**	0 1.59	0.14	0 **0.92**
3.875	Imbrium	2.28	0	**1.00**	0	0.95	0
3.850	Schrödinger	0	2.28	0	0	0.95	0
3.800	Orientale	0	0	0	0	0	0

[a] Age values show the precision of 0.001 Ga, which might not reach in the real radioisotope ages.
[b] $V_{\text{m-bin}}$: Volume of the melt within given age interval. It includes melt of both smaller impacts and basins.
[c] f_b: fraction of basin melt among all the generated melt.

6. Research paper III: Evaluation of the non-mare component of mare soils

The following section has been submitted as: Tiantian Liu, Greg Michael, Wilhelm Zuschneid, Kai Wünnemann, and Jürgen Oberst, Lunar megaregolith mixing by impacts: Evaluation of the non-mare component of mare soils, *Icarus*, 0019-1035, 113609, doi: https://doi.org/10.1016/j.icarus.2020.114206. The author contribution is explained in the section of "Structure of the dissertation". This paper presents the results using the 3D-model where not only the impact mixing (Paper I, II) but also the volcanic mare flooding is considered as well.

Abstract

The source of the non-mare component in the lunar mare soil samples is still an open question. A spatially-resolved numerical model tracing the diffusion of non-mare material was developed by means of the Monte Carlo method to study this issue in more detail. The vertically- and laterally-transported non-mare components are recorded separately to assess their concentration on the surface. We find a general higher efficiency of lateral transport than of vertical transport, but the opposite may occur within small zones of interest. The overall (background) distribution of non-mare component is estimated by averaging out regional variations of material composition caused by local impact mixing. We find that almost all the mare surface is mixed with non-mare material. If most of the mare regions have filled basaltic material about 500 m in thickness since the formation of basins, the average non-mare fraction in the top 5 m is about 0.1. The abundance of the non-mare component decreases with increasing distance from the mare-highland boundary, but the slope of the distance-dependence is shallower within ~100 km of the boundary than further away.

By comparing the background composition derived from our model with the geochemical analysis and geological interpretation of the lunar mare soil samples, we infer the most plausible geologic processes that have significantly altered the material composition at the sampling sites: for the Apollo 15 and 17 mare soil samples, the large fraction of non-mare material is likely to have resulted from the downslope slumping or lateral transport of the nearby massifs. The Apollo 12 sampling site that is located interior domains of Oceanus Procellarum has a component of Copernicus ejecta. A mixing of both Copernicus ejecta and excavated local underlying material by high-velocity ejecta has altered the composition at the surface. The non-mare material contained in the Apollo 11 and Luna 24 mare soil samples could have been built up gradually by both long-time lateral and vertical mixing. The mare deposit at the Luna 16 landing site is likely to be relatively thin resulting in the abundant vertically transported non-

mare component. Since the history of the lunar volcanic eruptions - deposit thicknesses, flux curves and onset of activity - have not been well constrained, we make simple estimates with the first-order accuracy. In addition, it was found that the vertically transported non-mare abundance in the top surface is influenced by both the cessation time of the major mare fillings and the total amount of mare deposit; the laterally-transported non-mare abundance in the top surface is mainly dependent on the cessation time of the major mare fillings. The peak time of eruption would not change the abundance of both the laterally and vertically transported non-mare component.

Keywords: Moon, surface; Regoliths; Impact processes; Cratering

6.1. Introduction

6.1.1. Non-mare component in the lunar mare soil samples

The returned lunar mare soil samples consist not only of local mare basalts but also of highland anorthosites (Wood, 1970). We use the term *non-mare* to refer to the components that are clearly not of volcanic mare origin but for which the relationship to the highlands is not clear or firmly established (e.g., Warren & Wasson 1977). The amount of non-mare material in Apollo 11, 12, and Luna 16 mare soil samples is about 20% on average; some of the Apollo 12 soil samples have more than 70% non-mare material (Rhodes, 1977). In addition, data from the orbital X-ray experiments (the measurement depth for the X-ray data is about 20 μm; Lucey et al. 2006) indicated that, for most mare surfaces, the chemical compositions, such as Al/Si concentration ratios, are more comparable with that obtained from the analyzed mare soils than with that of the local basalts. Thus it was suggested that the mixture of non-mare component in mare soils was not only restricted to the sampling sites that are near the mare margins, but may be a mare-wide phenomenon (Prettyman et al., 2006; Rhodes, 1977; Trombka et al., 1977).

The source of the non-mare component contained in the mare samples has been debated since the Apollo epoch (Farrand, 1988; Fischer & Pieters, 1995; Y. Huang et al., 2017; Laul & Papike, 1980; L. Li & Mustard, 2000; Rhodes, 1977; Simon et al., 1982). Two hypotheses have been proposed: It could result mainly from the mixing of material transported laterally by impacts from the distant highland regions (Budney & Lucey, 1998; De Hon, 1974; Evans et al., 2016; Head, 1982). It could also primarily be result from the mixing with local material that originally occurred beneath the mare deposit and was excavated by impact events (Arvidson et al., 1975; Fischer & Pieters, 1995; Hörz, 1978; Laul & Papike, 1980; Rhodes, 1977). Studies of both remote sensing data and collected samples have been used to evaluate the efficiency of lateral and vertical transport. The material mixing process across mare-highland contacts driven by a great number of impact events results in a mixing zone inside mare regions where the surface material has been mixed with a significant amount of non-mare component displaying relative high albedo in optical images. The observed ~4-5 km wide mixing zone across the mare-highland boundary is relatively narrow, indicating inefficient lateral mixing by impact events, while the abundance of highland material in the soil samples far from this boundary suggests more efficient lateral transport.

Y. Huang et al. (2017) implemented a regolith material transport model into the Cratered Terrain Evolution Model (CTEM) to investigate the mixing of material across the mare-highland boundary. The effects of local and distal ejecta were systematically studied and their relatively importance was quantified. It was found that both local and distal material transports were important to the material diffusion across the mare-highland boundary. In addition, the

superposition of crater rays was proposed to be a likely cause for the elevated non-mare abundance in some mare soil samples. For example, the Apollo 12 soil samples that had a significantly higher concentration of non-mare component were suggested to be influenced by the emplacement of the Copernicus Crater ray material.

While the research of Y. Huang et al. (2017) has improved our understanding of non-mare diffusion over the lunar surface, there remain several issues to resolve. First, Huang took the mare deposit as an intact layer on top of a highland layer. But the mare flooding occurred intermittently. Earlier transported non-mare material could become buried decreasing its abundance on the surface. Furthermore, the non-mare components beneath the mare deposit were not traced. Therefore, the relative magnitude of lateral versus vertical transport could not be evaluated.

In this study, we aim to develop a numerical model to trace the diffusion of non-mare material with the cumulative effect of impact mixing and intermittent filling of mare material. Questions that need resolving are: (a) Was the non-mare component transported over large distances on to the mare surfaces following the emplacement of mare material? Or (b) did a significant fraction of it originate beneath the mare surface? (c) How do spatial and temporal variations in mare deposition affect the expected surface abundances of non-mare materials today?

6.1.2. Mare volcanic flooding

Besides the impact mixing process, the volcanic eruptions are a key process to model. Previous work, nevertheless, has shown the difficulty to establish a well-constrained eruption flux (e.g., Head & Wilson, 1992; Hiesinger et al., 2011; Wilson & Head, 2017).

In order to constrain the flux of mare volcanism, the thicknesses of individual flows are required, which are found on the basis of their morphometric characteristics neglecting the problem that most flows are covered by others. Such measurements, nevertheless, are complicated due to the limited availability of suitable data necessary for the recognition of flow fronts (i.e., high-resolution topography and low-sun images), and the obliteration of flow fronts caused by impact cratering.

The onset and duration of mare volcanism are not well understood (summarized by Niquist et al. 2001). The returned samples revealed that mare volcanism was active between ~3.9 and 3.1 Ga (Head, 1976; Nyquist & Shih, 1992). The ages of some basaltic clasts in older breccias point to an onset of mare volcanism prior to 3.9 Ga (Ryder & Spudis, 1980), perhaps as early as 4.2–4.3 Ga (Dasch et al., 1987; Nyquist et al., 2001; Taylor et al., 1983). Dark halo craters found in remote sensing data may support the presence of the older volcanism. These craters are interpreted to be impacts into basaltic deposits that are now buried underneath a veneer of basin

ejecta. These underlying basalts might be among the oldest mare material on the Moon (Hawke & Bell, 1982; P.H. Schultz & Spudis, 1979). In addition, crater counts on mare surfaces suggest that some mare volcanism erupted as late as ~1–2 Ga ago (Hiesinger et al., 2011), which is much younger than that was determined in the collected samples (~3 Ga).

The total thickness/volume of the volcanic deposits is an important quantity in defining the extent of mare volcanism. A variety of techniques have been applied to estimate the total volume, but no consistent results have been obtained. Crater-geometry techniques using pristine crater morphometric relationships and the diameter of partially to almost entirely flooded craters yield values of mare thickness up to 2 km, ranging 200–400 m on average (De Hon, 1974, 1979; De Hon & Waskom, 1976; Hörz et al., 1991). Hörz (1978) further refined the crater-geometry technique by considering the average degradational state of impact craters and argued that the mare thicknesses estimated by De Hon and coworkers should be decreased by a factor of ~2. Other constraints are derived from "mascons" (i.e., the positive gravity anomalies observed over many of the basins filled with mare material). When the excess mass required to produce the observed gravity anomaly is assumed to be entirely mare filling, estimates for mare thickness of 1–2 km are obtained (Phillips et al., 1972; Phillips & Lambeck, 1980; Solomon & Head, 1980). However, these are minimum estimates, because it is not known whether there is additional mare fill below the equilibrium gravitational surface used in the modeling. In addition, there would be at most ten times larger estimates of the total volume if one assumes a specific geometry for the original impact basin cavities, modeled after the Orientale basin, and assumes similar cavity geometries for the all basins (Head, 1977).

Since higher-quality image data are now available, more studies have been done aiming to estimate the basaltic thickness. For example, by using recent high-resolution topographic data, Du *et al* (2019) revisited the previous studies of De Hon and Hörz. They identified 661 buried craters over the lunar surface and concluded that the basaltic thicknesses vary from 33-455 m with a medium value of 105 m. Using the high-resolution gravity and topography data, Gong *et al.* (2016) estimated the total thickness of basalts on the nearside hemisphere, which yield an average thickness of 740 m. In addition, a recent study from Needham & Kring (2017) summarized the thickness estimate of Williams & Zuber (1998) and some other recent estimates to calculate the volume of mare deposit. They derived a thinner average mare thickness of ~250 m.

Both the duration of emplacement and the thickness of mare deposits are not precisely known making it difficult to estimate the eruption flux. Our goal is thus to estimate the diffusion pattern of the non-mare material from different sources. In section 6.2, the main aspects of the previously developed model are outlined and the integration of the lunar volcanic history into it is described.

In section 6.3 and 6.4 two cases including the rapid and continuous mare fillings are present. First, and more simply (section 6.3), we take the volcanic material to be emplaced instantaneously as single layers. Secondly (section 6.4), we investigate a probably more realistic scenario, where the mare material slowly and continuously fills the basins. To investigate the diffusion features of the lateral and vertical mixing, the abundances of the laterally and vertically transported components are traced separately, and the relative rates of lateral versus vertical transport are evaluated. In section 6.5, the overall distribution of non-mare material is presented. Based on the model-predicted non-mare abundance, the origin of the non-mare component in the mare samples is discussed in section 6.6.

6.2. Model

In our previous work (Liu et al., 2020), a spatially-resolved numerical model was developed to investigate the diffusion of impact melts through impact mixing. Using the Monte Carlo method, a sequence of impact events was generated, where the occurrence time and the size of impact craters were calculated on the basis of the chronology and production functions of Neukum (1983). In the model, impact events of different sizes occurred in sequence. The occurrence of each impact event would exhume some local (target) material. The excavation depth, d_{exc}, was approximated to one third of the transient crater depth. The volume of the excavated materials was estimated to be one-third of a disc with d_{exc} in thickness and the transient crater size in diameter. The excavated material would be emplaced outside the crater cavity as ejecta layers, the thickness of which decreases with distance from crater center. In addition, the high-velocity ejecta would mix with local material while emplacing. The degree of mixing was quantified using a mixing ratio of local material to ejecta, $\mu = 0.0183r^{0.87}$ (Oberbeck *et al.* 1975). When μ is larger than 5.0, the value of μ was modified by roughly half: $\mu' = \mu/2 + 2.5$ (Petro & Pieters, 2006).

The evolving distribution of material composition on the surface and with depth caused by each impact event was recorded by the uniformly distributed one million points on a sphere with the Moon's radius (1737.4 km). Each point was related to a certain area of ~5×5 km^2. In addition, the increasing number of deposition layers as the simulation progresses made it necessary to periodically simplify the layer sequence to one: 0.2×1.9^a m, where a = 0, 1, …, 20. Materials within set layers would be mixed together resulting in a more average composition. The thinner layers close to the surface were chosen to preserve a fine resolution of material composition in the near surface. A more detailed explanation of the model is given in Liu et al. (2020).

In this study, we extend the capabilities of the model and take into account the volcanic basin infilling forming the lunar mare regions. The minimum crater diameter considered is 5 km. In the following section, the models used to simulate the ejecta distribution and the mare fillings

are presented in detail. In all model runs of sections 6.3 and 6.4, the simulated cratering is identical in timing, position, and crater sizes, so all changes can be attributed to the varying parameters of the lava emplacement process.

6.2.1. Ejecta distribution

During the formation of an impact crater, the majority of the excavated material is deposited near the crater rim forming a continuous blanket (i.e., the proximal ejecta which is generally distributed within 2-3 radii from the crater center). Further away from the crater, the continuous ejecta is replaced by the patchily distributed distal ejecta, usually in the form of bright rays and grouped secondary craters. Although the volume of distal ejecta is not large (~25% deposits further than five radii away from the transient crater rim; Liu *et al.*, 2019, 2020), previous studies have shown its significance to the material composition of mare regions. For example, the study of Huang et al. (2017) focused on the diffusion of non-mare material across the mare-highland contact. It showed that if only the proximal ejecta contributed to the soil composition, the mare surface would be clearly different from what is actually seen on the Moon, and the mare-highland mixing zone would be rather narrower than observed.

For proximal ejecta, the thickness distribution with distance from crater center (r) conforms to a power law, typically: $\delta(r) = Ar^{-3}$ (A is constant but varies for differently-sized craters, Melosh 1989). However, so far, no systematic research has been performed to obtain a scaling law for the thickness distribution of distal ejecta. In addition, distal ejecta may occur much further out than where we see bright rays and secondary craters. This fraction of the distal ejecta emplaced with high velocity and fine grain size is difficult to distinguish from the background surface.

Places superposed by the patchy distal ejecta locally have thicker transported material than their surrounding background. This clustered material would be redistributed by the subsequent impact events. As time passes, the clustered material diffuses over the larger area decreasing the thickness. That is, the patchy distal ejecta would fade into the background with continuous impact mixing, and the thickness distribution of the patchy ejecta material becomes more uniform. The average effect on distal ejecta looks similar to a uniform distribution. To estimate the distribution of distal ejecta, we therefore assume that the distal ejecta is also continuously distributed, and the thickness is calculated based on the extrapolated power law mentioned above. Although the distal ejecta of recently formed larger impact craters, such as Copernicus crater, could still remain patchy, their regional influence could be easily recognized from their background. If it occurs over the target regions, such as sampling sites, the composition of regional surface could be significantly different from its background.

The power-law distribution of ejecta thickness leads to a thinner deposit at locations further from the impact center. The farthest ejecta that the model would trace should thus have the

minimum deposit thickness (h_{min}), based on which the ejecta coverage range of each impact event can be calculated. All the excavated material would be distributed within the coverage range to maintain the total volume. The value of h_{min} is taken to be 0.01 m in this study. Our simulations showed that a smaller value for the minimum thickness, which would relate to a larger traced range of ejecta, would lead to a similar composition of surface material since the volume of ejecta at greater ranges becomes too small to significantly augment the non-mare component. For example, when the value of h_{min} is ten times smaller (i.e., 0.001 m), the estimated composition of surface material is comparable with that using h_{min} of 0.01 m, and the difference of non-mare fraction in the near surface is generally smaller than ~0.001. On the other hand, a larger value of h_{min} would relate to a smaller range of ejecta deposit. The simulation results then display significantly less mixing of the non-mare component over the mare regions. For example, when the value of h_{min} is ten times larger (i.e., 0.1 m), more than half of the mare surface, especially the central part of mare regions, has no mixing of non-mare material. This is clearly not in agreement with the observed composition of the lunar surface, so that we exclude this value. The simulation results with the varying values of h_{min} are presented in the supplementary file.

Craters smaller than 5 km are not involved in the model. The smaller impact events have high frequency. They have well mixed the material in the top surface producing a fragmental regolith layer. However, since they hardly excavate fresh material from the beneath maria, they would not significantly change the abundance of the material components in the top surface. Given that the typical thickness of regolith layer over the maria is about 5 m (Fa et al., 2014; Fa & Jin, 2010; McKay et al., 1991), in the following discussions, we present the average abundance of non-mare component in the top 5 m. These results can be regarded as the average composition of the regolith where the material has been frequently mixed by smaller impact events and hence the material is homogeneously distributed.

6.2.2. Mare volcanic filling

As indicated by the diverse basalt ages over the mare regions (e.g., 30 units over Mare Imbrium; Hiesinger et al., 2011), the lunar basins were filled with multiple flow units. The intermittent mare flooding would decrease the distribution of early-transported non-mare component on the surface. Therefore, as well as the impact mixing process, the sequential mare volcanic filling is also described by the model. The way to simulate both processes is illustrated in Figure 35a. Before the flooding by volcanic material, both the highland and mare region surfaces are non-mare material. To better trace the vertical and lateral mixing of the non-mare component, the non-mare component originating from the highland regions is tracked as “laterally” transported non-mare material, and that from beneath the mare infill as “vertically” transported non-mare

material. The labels “laterally” and “vertically” are used to specify the spatial origin, but not necessarily a different mineralogical composition.

At the time of a_1 (Figure 35 a1), an eruption occurred, burying the surface of the mare region with volcanic material m_1. Subsequent impact mixing redistributes mare material regionally and excavated some non-mare materials from beneath the mare layer (i.e., vertically transported non-mare component). Some highland material is transported from the highlands to the mare region (indicated by the arrow in Figure 35 a2). At the time of a_3 (Figure 35 a3), another volcanic eruption occurs, the generated mare material deposits m_2 on the top of volcanic deposit m_1. The impact mixing keeps laterally transporting the non-mare material to the mare regions. Some of the early-formed volcanic deposit m_1 are re-excavated to the surface (the open arrow in Figure 35 a4); some of the early-transported highland could be delivered to the surface (the thick closed arrow in Figure 35 a4); some mare material might be transported to the highlands (the thin closed arrow in Figure 35 a4). On the lunar surface, the long-term impact mixing excavates various amounts of both mare and non-mare material to the surface, resulting in the mixing of mare/non-mare components to different degrees in the present day.

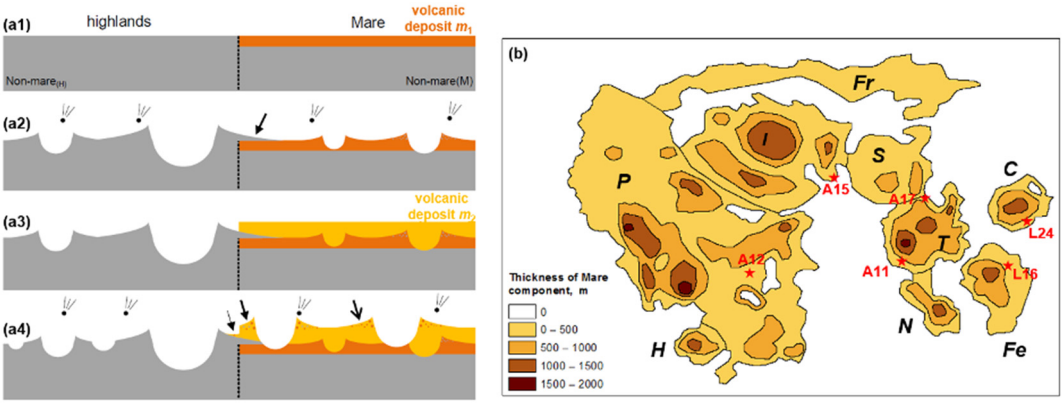

Figure 35 (a1-a4) A schematic of the filling of volcanic material. (b) The thickness distribution of mare material (after De Hon 1974; De Hon 1979; De Hon & Waskom 1976; Hörz et al. 1991) over the Oceanus Procellarum (P), and the Mare Frigoris (Fr), Fecunditatis (Fe), Humorum (H), Imbrium (I), Serenitatis (S), Tranquillitatis (T), Nectaris (N) and Crisium (C). The red stars indicate the locations of Apollo (“A”) and Luna (“L”) sampling sites.

In this study, the volcanic filling of the larger mare regions on the lunar near side are simulated, including Oceanus Procellarum (P), and the Mare Frigoris (Fr), Fecunditatis (Fe), Humorum (H), Imbrium (I), Serenitatis (S), Tranquillitatis (T), Nectaris (N) and Crisium (C). Other regions are taken to consist of non-mare highland material. The pre-existing topography that is covered over by successive mare layers is not considered beyond what is shown in Figure 35a.

The eruption flux has not been well constrained. We approximate *the peak time of eruption*, *the thickness of mare deposits*, and the *cessation time of the major eruptions* for modeling.

Peak time of eruption: The qualitative eruption features of volcanic history of the Moon were pictured previously (Head & Wilson, 1992, 2017; Wilson & Head, 2017). Head & Wilson (1992) compared the flux of volcanic filling derived from different approaches (i.e., the volume of mare material emplaced on the surface as a function of time), all of which pictured a similar trend of eruption flux from high to low but with different peak times. Based on the returned samples, a peak prior to ~3.5 Ga was obtained. The recent study from Needham and Kring (2017) that combined the estimated of mare thickness using different methods also indicted the volume peak at ~3.5 Ga. Using the age of the surface exposure of mare units, the flux curve was shifted toward younger ages with the peak at ~3.2 Ga because the older mare material was covered by the uppermost young deposits. Investigations of the stratigraphy of mare material showed the volumetric significance of early mare deposits yielding a flux curve with a peak at older ages of ~ 3.8 Ga. The peak of 3.8 Ga is taken for simulations, and the influence of the younger peak would be discussed in section 6.4.3.

Thickness of mare deposits: There is no direct measurement of the thickness of lava deposits over the mare regions. The thickness distribution of volcanic deposits was systematically studied using crater-geometry techniques pioneered by De Hon. This approach relies on impact craters flooded by mare material. By using the ideal crater shapes, one can calculate the height of the fresh crater rim. The thickness of mare deposits is then calculated by subtracting the present height from the estimated initial rim height. This approach has been used all observable flooded craters, and isopach maps of the thickness of volcanic filling (Figure 35b) were constructed (De Hon 1974; De Hon 1979; De Hon & Waskom 1976; Hörz et al. 1991). We use this result as an estimate of the total volcanic deposit over the mare regions (H_{DeHon}). Note that, in Figure 35b, the contour of a certain color represents a range of mare thickness. The upper limit (instead of the median value) of each contour is taken for simulations. In this way, the major mare areas are filled with mare material of 500 m in thickness, which is about the median value of the previous estimates (~100 m – ~1 km). The effect of the varying mare thickness on the non-mare distribution is discussed in section 6.4.3. For each mare region, the areas showing the thickest mare deposit are flooded first. As time goes on, mare material accumulates according to the eruption flux. The surrounding areas of thinner mare deposit are subsequently flooded. After the deposit of the youngest volcanic eruption, the thickness of volcanic deposit corresponds to H_{DeHon}. A time step of 0.01 Ga is used to simulate such continuous eruption. At each step, the mare filling occurred within a certain contour region is taken to be uniformly emplaced.

For mare deposits with a thickness of 500 m, a 5 km diameter crater would begin to tap the underlying non-mare material, the evidence of which could be found through remote sensing data. Such craters were proposed to possess a ring of low FeO ejecta, where the FeO abundance

could be calculated using UV-VIS data from the Clementine mission. For example, Thomson et al. (2009) examined 23 craters on Mare Imbrium >10 km in diameter. Six craters were suggested to penetrate the mare deposit indicated by their surrounding halos of low FeO ejecta. However, due to the small volume of the excavated mare component, the ejecta of a crater that just begins to tap the sub-mare material hardly displays obvious low FeO evidence on the surface.

Cessation time of the major eruptions: The mare regions are the result of volcanic infilling after the formation of the giant basins. The absolute age dating of specific rock samples shows that significant periods of time elapsed between basin formation and extrusion of mare material into the basin, but both the basin ages and the onsets of volcanic infilling are only roughly constrained (Head & Wilson, 1992; Hiesinger et al., 2011; Whitten & Head, 2015a, 2015b; Wilhelms, 1987). At one extreme, volcanic eruptions may be assumed to initiate soon after the formation of the respective basin. On the basis of superposed crater density, Wilhelms (1987) documented the relative ages of the lunar basins. Oceanus Procellarum, Frigoris, Fecunditatis, and Tranquilitatis basins were distinguished to be pre-Nectarian, and their formation time was suggested to be around 4.1 Ga. Humorum and Nectaris basins were classified into the Nectarian Period, with formation times around 3.9 Ga. The age of Serenitatis, Crisium and Imbrium could be determined from the returned lunar samples. Although their radioisotopic ages are still debated, the generally accepted formation times of both Crisium and Serenitatis basin are around 3.9 Ga, with the Imbrium basin about 0.05 Ga younger (Stöffler, 2006).

Each volcanic eruption in the model is taken to cover the entire surface within the contour line. This simplified approach can be considered consistent with the early mare filling events, but not with the last flows due to their smaller volume. Head & Wilson (1992) estimated the volume of mare material during different periods and showed that the volume of Upper Imbrian deposits was about thirty times greater than those later than of the Eratosthenian Period. In addition, the total coverage area of these younger deposits was six times smaller than that of the earlier deposits. With the aim to investigate the general features of non-mare diffusion, the irregularly distributed young mare deposits are not taken into account in this model. However, the cessation time of the mare filling that could cover the entire mare surface (i.e., the cessation time of major mare flooding) is difficult to estimate. The age of the youngest flows helps to constrain the infill age. To determine the rough cessation time of the main filling (t_{end}) among different mare regions, we assess the fraction of area of mare deposits younger than a certain age relative to the whole mare region. We take the value of the fraction to be ½, that is, the age t_{end} marks the age when only half of the exposed area would be covered by younger flows, where the age of mare units was estimated by Hiesinger et al. (2011). For Oceanus Procellarum, Mare Frigoris, Humorum, Nectaris, Fecunditatis, Tranquillitatis, Serenitatis, Crisium, and

Imbrium, t_{end} is calculated to be 3.4, 3.5, 3.5, 3.6, 3.6, 3.6, 3.5, 3.3, and 3.3 Ga, respectively. The influence of the varying t_{end} value is discussed in section 6.4.3.

6.3. Results basin filling

In the first case, the volcanic material is taken to be emplaced instantaneously as a single layer at t_{end} over the different mare regions. The thickness of mare material over all the mare regions is taken to be 500 m, the mare thickness in most mare regions (Figure 35b).

6.3.1. Mixing of the laterally transported non-mare component

The excavated non-mare component is entrained in the ejecta of impact craters that occur on the highlands, a part of it travels across the mare-highland boundary, and then falls on the mare regions (i.e., laterally transported non-mare component). As time goes on, the laterally transported non-mare component on the mare surface builds up. But the early-transported non-mare material could become buried, being covered by a rapid filling of volcanic material. The size and frequency of later-formed impact events would then determine the abundance of the laterally transported non-mare component of the mare surface. Only impacts occurring near the mare-highland boundary could bring a significant amount of laterally transported non-mare material to the mare regions; the ejecta of those occurring far away hardly reaches the mare regions except from some really large craters. Especially at the central areas of the mare regions, little mixing with laterally transported non-mare material occurs.

Figure 36a represents the spatial distribution of the laterally transported non-mare component in the near surface (the top 5 m). It shows that in almost all the mare regions some laterally transported non-mare component is present. Near the margin of the mare regions, laterally transported non-mare material is more abundant than in the inner part that can only be reached by the ejecta of larger impact events. In addition, because of the longer exposure time after the volcanic flooding, the mare regions with the older t_{end}, such as Mare Tranquillitatis and Nectaris, accumulate more laterally transported non-mare material. But the regional context of the mare region also influences the amount of the accumulated laterally transported non-mare component. A mare region surrounded by highland regions would have a higher accumulation rate. For example, although the volcanic cessation time of Mare Crisium is 0.3 Ga later than that of Mare Tranquillitatis and Fecunditatis, the surface of those regions displays a comparable abundance of laterally transported non-mare component.

6.3.2. Mixing of vertically transported component

Impact events occurring within the mare regions can penetrate through the mare deposit and excavate underlying non-mare material. These large-scale impact events can exhume a great

amount of non-mare material to the near surface (i.e., vertically transported non-mare component), forming non-mare-enriched zones. The smaller impact events with shallower excavation depth do not contribute a significant amount of non-mare material to the near surface, but locally garden the surface material diluting the regional concentration of the vertically transported non-mare component.

Figure 36b presents the spatial distribution of the vertically transported non-mare component in the near surface (the top 5 m). We see that vertically transported non-mare is also widely mixed in the near surface but is less abundant, as indicated by the bluish color in Figure 36b. The distribution is relatively heterogeneous marked by some striking non-mare-enriched zones shown in red. These zones are well-preserved indicating their slow fading rate as a result of the lower impact cratering rate during the recent period (Neukum 1983).

6.4. Continuous basin filling

In a possibly more realistic simulation, the mare material continuously fills the basins until t_{end}. The value of t_{end} is the same as previously, but the total thickness of the basaltic deposit is equal to H_{DeHon} (Figure 35b). The peak time of mare fillings is 3.8 Ga. Note that the following discussions concerning the abundance of non-mare component is on the basis of those given conditions.

6.4.1. Diffusion features of non-mare material

When the volcanic material is continuously filling the basins, the volume and therefore thickness of each eruption step is much less. Although the surface laterally transported non-mare material would be covered over repeatedly, the smaller thickness of coverage increases the probability that impact events re-excavate the covered laterally transported non-mare material. Some of the laterally transported non-mare component deposited there earlier can become entrained in the ejecta of subsequent impact craters. This way, it could be repeatedly excavated and migrate upwards and finally to the surface layer.

Given the crater diameters of km-scale in simulations, impact events occur on mare regions can easily penetrate through the mare deposit of hundreds of meters in thickness leading to a comparable picture of the concentration of vertically transported non-mare component with that shown in Figure 36b. But on the regions with thicker mare deposit, the abundance of the mare component on the surface should be significantly increased, so that the relative fraction of the vertically transported component becomes less.

6.4.2. Magnitude of lateral versus vertical mixing

Figure 36c displays the laterally transported non-mare component in the near surface (the top 5 m). It appears essentially the same as in the case of a rapid filling, indicating that the stepwise transport of the early-deposited non-mare component to the near surface is too inefficient to result in a significant difference in composition. The total volume of laterally transported non-mare component over the mare surface is only ~2% larger relative to that with rapid flooding (Figure 36a and the upper sub-plot of Figure 36e), that is, ~2% more the buried component is re-excavated to the mare surface. As we can see that, the histogram distribution of the difference caused by the continual filling (the lower sub-plot of Figure 36e) is smaller than 1.

Figure 36d shows that there are fewer zones enriched in non-mare material caused by vertical transport over the Oceanus Procellarum and Mare Imbrium regions. This deficiency of vertically transported non-mare material is caused by the thicker mare deposit, as indicated in Figure 35b. Fewer impact events are able to penetrate the mare material, and thus in those cases, the fraction of the vertically transported non-mare component is lower. The total volume of vertically transported non-mare component over the mare surface (the top 5 m) is ~ 20% smaller relative to that with rapid flooding mainly (Figure 36b and the upper sub-plot of Figure 36f) due to the missing of non-mare zones caused by the vertical transport at the south and southeast of Oceanus Procellarum (Figure 36d). The histogram distribution of the difference caused by the continual filling (the lower sub-plot of Figure 36f) displays the maximum difference is about 5%.

The average fraction of laterally and vertically transported non-mare component is 0.07 and 0.03, respectively (Figure 36c and d). The greater average abundance of laterally transported non-mare component indicates the generally higher efficiency of lateral mixing. But it is notable that for a given area of interest, the evaluation of the relative magnitude of the lateral versus vertical mixing needs to take its geologic context into account. For example, if the area is close to the recently formed impact crater, lateral mixing could become dominant; if the mare material is known to be only thin, the influence of vertical mixing may increase.

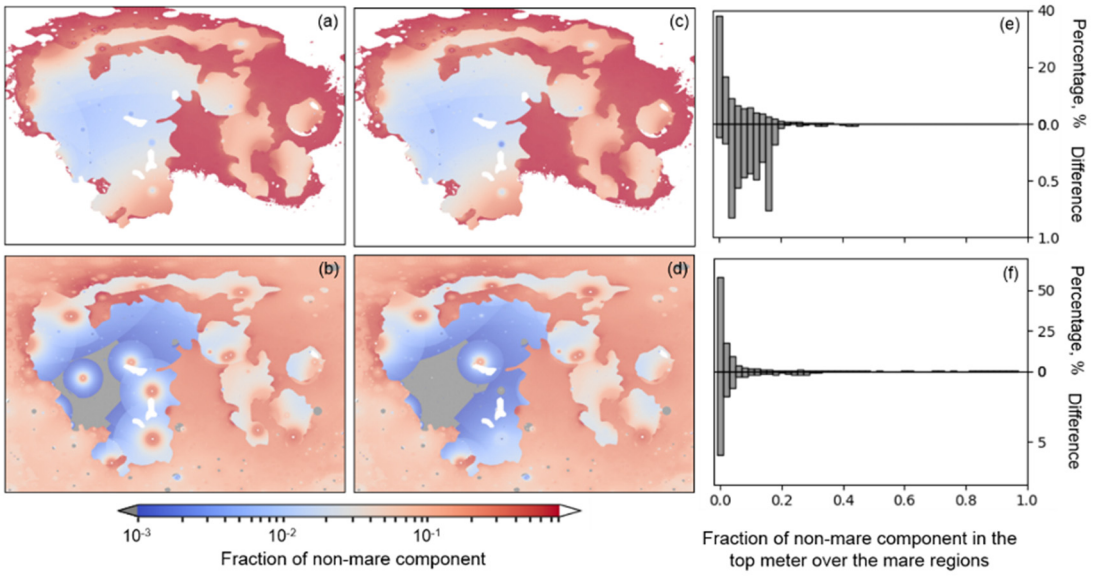

Figure 36 The distribution of non-mare material in the top 5 m. In the first scenario the mare material is emplaced instantaneously (first column, a and b); in the second scenario, it is emplaced by continuous flooding with time (second column, c and d). (a) and (c) present the abundance of non-mare material that is laterally; (b) and (d) show the abundance of non-mare component that was vertically excavated from the beneath. The upper sub-plots of (e) and (f) present histograms of laterally and vertically transported non-mare abundance of the mare regions when the mare material is emplaced instantaneously, and their lower sub-plot the absolute differences of the percentage caused by the continual filling.

6.4.3. Varying parameters concerning mare filling

Given the uncertainty in the flux of mare filling, simulations with varying setting of mare fillings are run to investigate the major factors affecting the non-mare mixing. The parameters studied include the thickness of mare deposits, the cessation time of the major mare filling and the peak time of eruption. To better compare the results, the sequence of impact craters remains the same. Only the studied parameter is varied, the values of all other parameters are identical to those described in section 6.2 in each simulation. Table 8 summarizes the simulations shown in this section.

Table 8 Simulations with varying parameters concerning mare fillings.

Parameters studied	Mare thickness	Cessation time of the major mare fillings	Peak time of eruption (Ga)
Mare thickness	H_{DeHon} 1/5 H_{DeHon} 1.5 H_{DeHon}	t_{end}	3.8
Cessation time of the major mare fillings	H_{DeHon}	t_{end} t'_{end} t''_{end}	3.8
Peak time of eruption	H_{DeHon}	t_{end}	3.8 3.3

Parameter I: Mare thickness

Estimates of total volume of mare deposit vary significantly. The implicit assumption of the crater-geometry approach that De Hon applied is that all the flooded craters were originally formed on pristine basin floors before any lava had been erupted. The volume estimates are therefore minimum values. Du et al. (2019) found that mare thickness derived from measurements of buried craters were systematically over-estimated because the topographic degradation of the impact craters was not considered. After taking degradation into account, they found that the median thickness was 105 m, which is nearly 5× thinner than H_{DeHon} described in section 2.2 (Figure 35b). In contrast, Gong et al. (2016) used GRAIL gravity data to estimate average mare thickness and found it to be 740 m, which is close to 1.5× thicker than H_{DeHon}.

Both simulations with the thinner (1/5 H_{DeHon}) and thicker (1.5 H_{DeHon}) maria are performed. The statistical non-mare abundance is shown in Figure 37 (the spatial distribution is presented in Figure 42 in the supplementary file). It is seen that the abundance of laterally transported material is not affected by the mare volume, but the vertically transported non-mare component is significantly altered. Since the underlying non-mare component is more easily excavated from the thinner mare deposit, the average abundance of vertically-transported non-mare component on the surface increases by 110%. For the thicker mare infill, the abundance of vertically transported material decreases by 40%.

Parameter II: cessation time of the major mare filling

Given the same total deposit of mare material, as the onset of the mare basalt is taken to be the basin formation age (the upper limit of volcanic eruptions, B. A. Ivanov & Melosh, 2003), a later cessation time of volcanic eruptions leads to a lower lava eruption flux (i.e., the thinner mare deposit of each mare eruption). To investigate its influence, the simulations with the later cessation time (t'_{end} and t''_{end}in Table 9) are performed. The value of t'_{end} is obtained when the fraction of area of mare deposits younger than a certain age relative to the whole mare region is taken to be 2/3 (rather than ½, t_{end}); The value of t''_{end} is taken from the age of the youngest mare units of each region representing an extreme simulation.

Table 9 The cessation time of the main flooding among different mare regions.

Mare[1]	t_{end}, Ga[2]	t'_{end}, Ga[3]	t''_{end}, Ga[4]
Oceanus Procellarum	3.4	3.0	1.2
Frigoris	3.5	3.5	2.6
Humorum	3.5	3.5	2.9
Nectaris	3.6	3.5	3.4
Fecunditatis	3.6	3.5	3.4
Tranquillitatis	3.6	3.5	3.4

Serenitatis	3.5	3.3	2.4
Crisium	3.3	3.1	2.7
Imbrium	3.3	3.1	2.0

[1] The ages of geologic units of the Mare Crisium, the Mare Nectaris and the Mare Fecunditatis are derived from Hiesinger, van der Bogert, et al., 2011 and Hiesinger et al. 2008, and Hiesinger et al. 2006, respectively. The others are taken from Hiesinger, Head, et al. 2011; [2] More than half of each mare region is covered with volcanic material older than t_{end}; [3] More than two thirds of each mare region is covered with volcanic material older than t'_{end}. [4] t''_{end} is the age of the youngest mare unit of each mare region.

The later cessation time extends the time when laterally transported non-mare material is being buried by the emplaced volcanic material. The volume of laterally-transported non-mare component in the near surface would therefore be less. As seen from Figure 37, in the near surface, when the cessation time of mare flooding is taken to be $t'_{end}$and t''_{end}, the abundance of the laterally transported non-mare component is 45% and 50% less relative to the estimate shown in Figure 36d, respectively (the spatial distributions are shown in Figure 43).

The later emplacement not only buried the more laterally transported non-mare component, but also the more late-excavated non-mare component caused by the vertical transport. The concentration of vertically transported non-mare component is therefore also less. When the cessation time of mare flooding is taken to be t'_{end} and t''_{end}, its average fraction is decreased by 33% and 40%, respectively (Figure 37 and Figure 44).

Parameter III: peak time of eruption

To investigate the influence from a varying eruption flux, the simulation is performed with a later volcanic eruption peak at 3.3 Ga (instead of 3.8 Ga). Since the abundance of the laterally transported non-mare component depends on the cessation time of the volcanic eruptions, its concentration on the surface is unchanged (Figure 37 and Figure 44).

The younger volcanic peak indicates that the volume (i.e., thickness) of the old volcanic eruption is less. Therefore, in the early period, there would be more vertically transported non-mare being excavated to the near-surface, some of which could be finally delivered to the top surface on present day by the cumulative impact mixing. The simulation results (Figure 37), however, show that the increased amount of the vertically transported non-mare (<1%) is too less to significantly alter the material composition in the top surface.

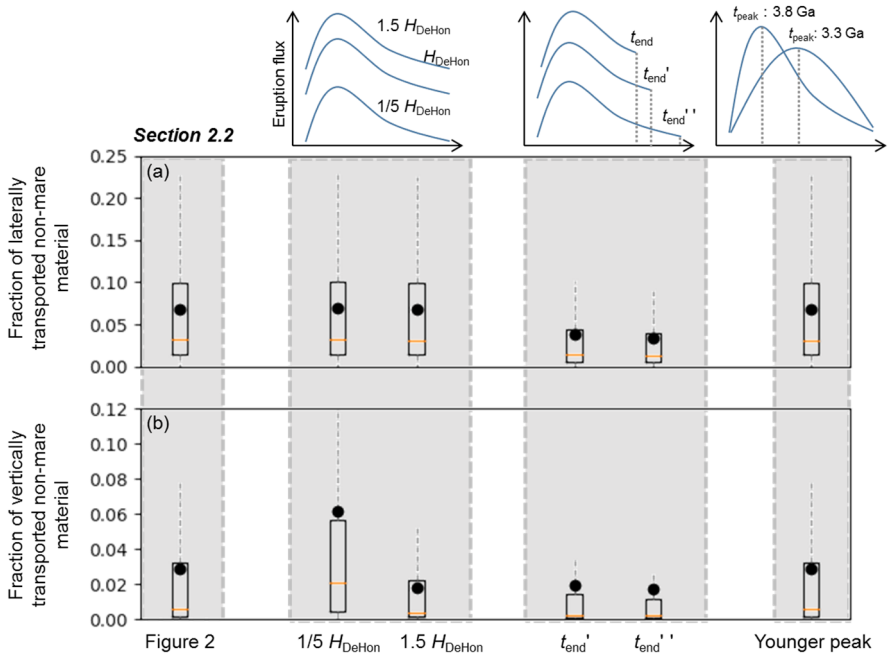

Figure 37 The fraction of laterally (a) and vertically (b) transported non-mare material with varying parameters concerning mare filling in the top 5 m. The results based on the different studied parameters are indicated by four grey zones. For better comparison, the first zone shows the results based on the parameters described in section 2.2 (with mare thickness, H_{DeHon}; cessation time of mare filling, t_{end}; peak time of mare filling, 3.8 Ga). The second, third and fourth zone show the results for other values of mare thickness, cessation and peak time of mare filling, respectively (the parameters are summarized in the Table 8). The schematics above the grey zones illustrate the differences of the studied parameters. The non-mare distribution is shown as box-and-whisker plots. The inside red lines are the median value and the upper and lower boundaries of the boxes are the first and third quantile. The ends of the whiskers represent 99% of data. The black dots represent the mean values.

In summary, on the lateral transport, only the cessation time of the major mare filling has a significant influence. Vertical transport is strongly influenced by both infill thickness variations and the cessation time. The timing of the peak volcanic activity does not exert a significant influence. The non-mare abundance with respective to the simulations of difference parameters is presented in Table 11.

6.5. Spatial distribution of non-mare component

6.5.1. Overall features

Because of local impact mixing, the regional distribution of the non-mare component varies with the different random spatial configuration of the generated impact craters in simulations. By taking an average of the results from ten simulations where the spatial configuration of generated craters is different, the regional differences, especially the non-mare enriched zones caused by vertical transport, are averaged out and the general features of non-mare material concentration are obtained (Figure 38).

The spatial distribution of the total non-mare material including both laterally and vertically transported non-mare component in the near surface (the top 5 m) is shown in Figure 38a. Since the regional enrichment in the non-mare component is averaged out, the distribution in each mare region is relatively homogeneous. In addition, it can be seen that throughout the mare regions the non-mare component is present. This is consistent with the results from orbital X-ray instruments, which demonstrated that the admixture of non-mare components is a ubiquitous feature over the entire mare surface (Prettyman et al., 2006; Rhodes, 1977; Trombka et al., 1977).

The older mare surfaces accumulate more non-mare material. The non-mare component over the Mare Tranquillitatis, Fecunditatis, and Nectaris regions showing the more reddish and lighter color is more abundant than that of Oceanus Procellarum and the Mare Serenitatis, Imbrium and Crisium regions. In addition, the boundary of mare and highland regions is generally clear but that of the mare regions where volcanism ceased early is relatively fuzzy, such as Mare Frigoris, Tranquillitatis and Fecunditatis.

The histogram of the non-mare fraction of all the mare regions in the top 5 m (Figure 38b) shows that if most of the mare regions have filled mare material about 500 m in thickness since the formation of basins, the average and median fractions of non-mare component over all the mare regions are both about 0.1. Half of the mare regions possess a non-mare component fraction between 0.05 and 0.15. The mare regions with non-mare fraction smaller than 0.1 are mainly distributed in the Mare Crisium region and the inner parts of Oceanus Procellarum and Mare Imbrium. This results not only from their late volcanic filling, but also from the long distances between the rim and the central regions.

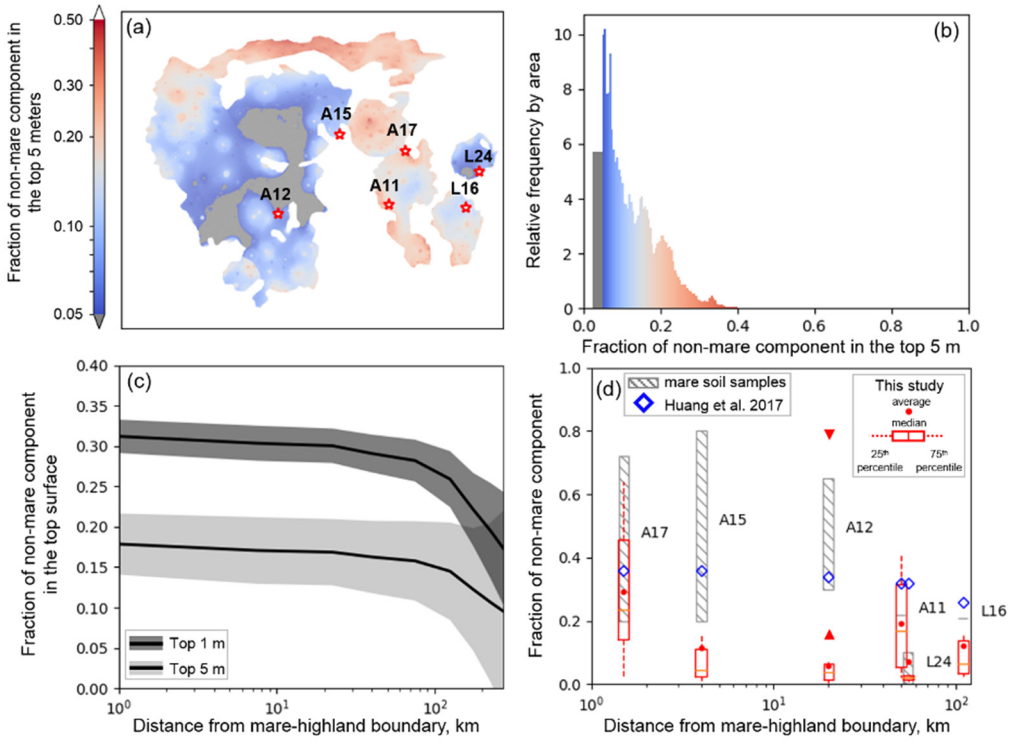

Figure 38 Averaged non-mare material abundance in the top 5 m based on multiple simulations. (a) Spatial distribution of the non-mare component. Red stars indicate the location of Apollo (A) and Luna (L) sampling sites. (b) Histogram of the non-mare component abundance in the top 5m by area over the mare regions. The sum of the bars' value is 100%. (c) Average distribution of non-mare component in the top 1 and 5 m with the distance from mare-highland contact. The black curves indicate the average values and the upper and lower bands of the plots (grey zones) are defined by the 95% confidence intervals from the Monte Carlo simulation results. (d) Non-mare material abundance at the Apollo and Luna sampling sites (Bence & Grove, 1978; Rhodes, 1977), and its distribution with the distance from the mare-highland boundary. The grey bars with slashes represent the chemical estimate of the lunar soil samples. The blue diamonds are the median abundance from Y. Huang et al. (2017). The red symbols are the results of this study where the points indicate the mean value. The box-and-whisker plots are presented for the better comparison with Huang et al.'s results, where the inside red lines are the median values and the upper and lower boundaries of the boxes are the first and third quantile. The red triangle and the red inverted triangle are the predicted non-mare fraction at A12 when the very early cessation time of mare filling (0.1 Ga after the basin formation) and when the formation of Copernicus Crater (0.8 Ga, 98 km in diameter) is considered, respectively (all the other parameters are the same as those in section 2.2).

6.5.2. Distribution with the distance from the mare-highland boundary

The fraction of non-mare component at varying distance from mare-highland boundary is calculated by taking the average value of the non-mare fraction of each mare region at the given distance. In the top 5m, the average fraction of the total non-mare material, i.e., including both laterally and vertically transported non-mare material, within 100 km is both about 0.2; between 100 km and 200 km, the non-mare abundance quickly decreases; on the more internal mare regions, the fraction is smaller than 0.1.

The average composition in the top 5 m is regarded to be comparable with that of the lunar surface regolith where the material is homogeneously distributed due to the long-term

gardening of small impacts. But for a young surface, such as the youngest geologic unit in Oceanus Procellarum with an age of 1.2 Ga (Hiesinger et al., 2011), only the very top surface has been well-mixed. The calculated average non-mare abundance in the top meter (Figure 38c) indicates that a fresh surface without intensive mixing could possess higher abundance of non-mare component.

6.6. Non-mare concentration at sampling sites

This section focuses on the material composition at the sampling sites, to test whether our model is able to reproduce these observations. The results on the basis of multiple simulations weaken the influence of local impact mixing. The calculated average non-mare distribution (Figure 38a) provides expectation values for the spatial composition, although we understand any particular impact configuration will show local differences. Based on the composition of the background surface, the non-mare abundance at the sampling sites is predicted (Table 10).

Figure 38d (red points) shows the expected fraction of the non-mare material of Apollo 11, 12, 15, 17 and Luna 16, 24 sampling sites in the near surface, and in relation to the distance from the mare-highland boundary. All these sampling sites are located near (<~100 km) the mare-highland contact where we expected a weak correlation with the distance. Apollo 11, 17 and Luna 16 are located in Mare Tranquillitatis, at the contact of Mare Tranquillitatis and Serenitatis, and in the Fecunditatis regions, respectively. The volcanic cessation time of these regions was relatively early, resulting in the higher abundance of non-mare component, with a non-mare component fraction of up to ~0.3. The Apollo 15, 12, and Luna 24 sampling sites are located on the Mare Imbrium, Oceanus Procellarum, and the Mare Crisium surfaces, where the volcanic cessation time was later leading to a less non-mare component (~0.1).

The non-mare abundance as a function of distance from the mare-highlands boundary and at the sampling sites were also predicted by Y. Huang et al. (2017). The median values of their results at the sampling site are shown in Figure 38d (blue diamonds). The results of Y. Huang et al. (2017) display no clear relationship between the non-mare abundance and the distance, which is consistent with this study, but the non-mare abundance calculated by Huang et al. is generally higher and more comparable with the average composition predicted for the very top surface by our model (Figure 38c). For better comparison, the predicted median values of non-mare abundance of this study are also presented (the red box-and-whisker plot; Table 10). It is seen that both the average and median abundance of non-mare component are smaller than Y. Huang et al's estimate. This can at least in part be explained by the assumptions in the model of Huang et al.: They divided the lunar surface into mare (4 km in thickness) and non-mare zones and took this as the initial status of the model. They did not consider the varying cessation time of mare flooding among the different mare regions and did not involve the continuous

mare filling that would bury the early-transported non-mare material, decreasing its abundance. In addition, as indicated in the Figure 38c, the top surface is expected to possess a higher abundance of non-mare material. Y. Huang et al. calculated the abundance of non-mare material of the very top surface (the uppermost millimeter(s)) which could result in the greater non-mare abundance than this study (the upper meters of the lunar surface material). The process of regolith gardening was contained in Y. Huang et al's model. Such a process would make the material, especially of the top surface (Figure 6 in Y. Huang et al. 2017), homogeneously distributed diluting the non-mare concentration. Even though such a process is not considered in this study, our predicted non-mare abundance is still less than Y. Huang et al's estimate. It may indicate that other factors, such as the sampling depth and the burial by the mare material, have a greater influence on the surface non-mare concentrations. Li and Mustard (2000) also calculated the non-mare abundance through an anomalous diffusion model, but only a narrow zone of the mare/highland boundaries was analyzed. Their results showed that the non-mare fraction quickly decreased from ~0.5 to ~0.2 over 5 km (the mixing-zone). Due to the limit of our model's resolution (5 km), although the drop of the non-mare concentration is not presented in this study (Figure 38), our estimates both in the top one (~0.2) and the top five (~0.3) meters near the mare/highland boundary are consistent with Li and Mustard's results.

Table 10 Non-mare fraction at the sampling sites.

Sampling sites	Chemically estimate[1]	This study[2]		Huang et al. (2017)
		Average	Median[3]	Median
A11	0.2	0.19	$0.17^{0.32}_{0.06}$	0.36
A12	0.3 – 0.7	0.06	$0.04^{0.07}_{0.01}$	0.36
A15	0.2 – 0.8	0.12	$0.04^{0.11}_{0.03}$	0.34
A17	0.1 – 0.7	0.29	$0.24^{0.64}_{0.14}$	0.32
L16	0.2	0.12	$0.07^{0.14}_{0.03}$	0.32
L24	0 – 0.1	0.07	$0.02^{0.02}_{0.01}$	0.26

[1] Rhodes 1977, Bence & Grove 1978; [2] parameters concerning mare flooding are taken to be: mare thickness: H_{DeHon}; the cessation time of the major filling: t_{end}; the peak time of mare eruption: 3.8 Ga;[3] the upper and the lower limit indicate the first and the third quantile.

Grey bars in Figure 38d present the abundance of the non-mare component in the soil samples of Apollo 11, 12, 15, 17 and Luna 16, 24 (Rhodes, 1977). The model-predicted non-mare abundance and the measurements of the mare soil samples are then compared:

Apollo 15/17: Both Apollo 15 and 17 samples were collected from multiple stations with the different geologic settings, and thus the non-mare concentrations display widely varying ranges of non-mare concentration. Rhodes et al. (1974) classified the Apollo 17 soils samples into three compositional groups. Each one related to a specific geologic setting: valley floor type, south massif type and north massif type. The south massif type soils contain abundant non-mare material with a fraction up to ~0.75 (e.g., Korotev and Kremser 1992), which is much greater than that of the valley floor type soils (~0.2). Similarly to the Apollo 17 soil samples, the Apollo 15 soil samples were found to be dominated by two types (Apennine Front and Apennine base) and the non-mare fraction ranges from about 0.2 to 0.8 (Duncan et al., 1975). As can be seen from Figure 38d, the model-predicted non-mare abundance falls at the lower range of the chemically estimated abundance in the mare soil samples. Given that the sampling site is adjacent to the highland massifs which present the similar chemical composition (KREEPy) with those non-mare samples (Korotev, 1976; Laul et al., 1978), downslope transport by slumping of nearby highlands could be the most plausible process enriching the non-mare abundance of the collected samples.

Apollo 12: The measurements of different Apollo 12 sub-samples also present a wide range of non-mare fraction from 0.3 to 0.7 which is greater than the model-predicted concentration (~0.05). Such a great non-mare abundance (the inverted red triangle in Figure 38d) may be obtained when the very early cessation time of mare-filling is considered in our model (e.g., 0.1 Ga after the basin formation). However, given the KREEP background of the landing site, such an early cessation time of mare-filling is unlikely. The role of other factors is likely more important. The sampling site is close to the late-formed Copernicus crater (390 km north of the site; Wilhelms 1987). According to the orientation of the bright rays of the Copernicus crater, the ejecta material has been believed to be derived from Copernicus crater. The non-mare material entrained in the ejecta of Copernicus could have been spread across the sampling site; in the meanwhile, the high-velocity ejecta could have excavated a certain amount of the underlying non-mare component (Y. Huang et al., 2017; Quaide et al., 1971; Schonfeld & Meyer, 1972). Multiple simulations with the formation of Copernicus crater (800 Ma, 96 km in diameter) are also performed. The results show that if all the other parameters remain the same as those in section 2.2, the non-mare fraction at A12 is increased by a factor of two (the red triangle in Figure 38d). This is still less than both the results of the chemical estimate and Huang et al. A plausible explanation is that the distal ejecta is taken to be continuously distributed so that the spatial geometry of crater rays that were included in Y. Huang et al are not considered. The continuously distributed distal ejecta could be regarded as the consequence of prolonged impact mixing. However, given the young age of Copernicus crater, most of its rays are well-preserved, and thus its influence on the A12 sites could be more significant than we predict.

Apollo 11/Luna 24: The sampling site is far away from the highland-mare boundary and no obvious disturbance of the young ejecta is observed. The model-predicted non-mare fraction of the Apollo 11 and Luna 24 soil samples is ~0.2 and ~0.1, respectively, which falls within the range of the chemical estimates. It indicates that the non-mare component in these soil samples has been mixed with both laterally and vertically transported non-mare material caused by the cumulative impact mixing.

Luna 16: The model-predicted abundance of the non-mare component is less than the chemical estimate of the samples. This may indicate either that the Mare Crisium mare deposit is thinner than 500 m or that the mare surface is older than 3.3 Ga (t_{end} in Table 9).

For the Apollo 11, 15 and Luna 16 samples, rays from Theophilus, Aristarchus or Autolycus, and Langrunus or Tarunius have been proposed as the sources for the highland non-mare components, respectively (Duncan et al., 1975; Schonfeld, 1975). Taking the Apollo 11 sampling site as an example, it is ~380 km (~7.6 radii) away from Theophilus crater (99 km in diameter). The ray length of Theophilus crater can be estimated to be ~950 km (Elliott et al., 2018), so that some of its distal ejecta might have deposited at the Apollo 11 sampling site. If the scaling law of ejecta thickness distribution is extrapolated to this distance, the thickness of Theophilus ejecta at the Apollo 11 sampling is about 1 m. The ratio of the amount of local material to that of ejecta is estimated to be ~3, that is, the fraction of ejecta is about 25%. This is comparable with the chemically estimated value of ~20%. However, the bright ray of Theophilus ejecta has been degraded and is hardly detectable on the present day. It is difficult to determine whether the Apollo 11 sampling site is really located on the ray deposit. If it is, the calculation of the local ejecta thickness indicates that the non-mare component in the samples is mainly derived from Theophilus ejecta. The new look at the Apollo 11 regolith which suggested the more mixing of non-mare component (>20%; Korotev & Gillis, 2001) may further support the deposit of the Theophilus ejecta.

In addition to the impact mixing, some other factors could also affect the non-mare abundance at the sampling sites, such as very young mare lava flows. Due to their small volume, they are typically regionally restricted and can be detected based on spectral data (e.g., the spectral ratios of Clementine imaging data used for the definition of the basaltic units; Hiesinger, Head et al. 2011). In addition, thorough studies of soils samples (e.g., Apollo 17; Rhodes 1974) suggested that the less coherent anorthositic (highland) material was preferentially sampled. Therefore, the sampling strategy could also have led to a bias towards a higher abundance of non-mare material resulting in the difference between the predicted abundance and the chemical estimate of the samples.

It should be mentioned that the abundance of non-mare material is predicted on the basis of the given model parameters including the mare thickness (H_{DeHon}), the cessation (t_{end}) and peak time (3.8 Ga) of mare flooding. Varying these values would change the predicted absolute value of non-mare abundance, but would not significantly change relative abundance among the areas covered with different amount of mare material.

For the Apollo 11 and Luna 24 sampling sites, the consistency between the model-predicted and the chemically estimated non-mare abundance suggests that the mare thickness at both sites is likely to be on the order of 500 m, and that other geologic processes aside from impact mixing did not play a significant role.

6.7. Conclusions

Lunar mare soil samples from the Apollo and Luna missions contain non-mare component (Rhodes, 1977). To investigate the possible origin and distribution of the contained non-mare component, a numerical model was developed to trace the diffusion of non-mare material, where both the vertical and lateral mixing are recorded to investigate their evolving features. The volcanic flux is the most important parameter, but it is not well constrained (e.g., the total mare volume and the onset and end of eruptions). The abundance of non-mare material is therefore calculated for various possible scenarios.

The laterally and vertically-derived non-mare component display different diffusion features. The distribution of the laterally transported non-mare material is relatively homogeneous and closely related to the distance to the mare-highland boundary. The majority of it is distributed near the mare-highland boundary, while the central mare areas possess a significantly lower abundance of laterally transported non-mare material. In contrast, the vertically-derived non-mare material is patchily distributed. It is closely related to the distribution of large impact events that could excavate a large amount of the underlying non-mare material to the surface, generating non-mare enriched regions. In addition, we find a higher efficiency of lateral transport than that of vertical transport in general. Those diffusion features of both laterally- and vertically-derived non-mare material could be helpful for the choice of future landing sites that aim to collect deep-seated material and for the interpretation of the source of non-mare component in the collected material.

It is found that, across almost the entirety of the mare regions of the Moon, a non-mare component is present. If the mare thickness is on the order of 500 m, the average non-mare fraction over the whole mare regions is about 0.1, and half of the areas possess a fraction ranging from 0.05 to 0.15. The mare surfaces with older volcanic cessation times contain more non-mare material, with an average fraction of ~0.3.

We compared our results with the analysis of the collected soil samples and discuss the most plausible geologic processes that may have altered the non-mare material abundance at the sampling sites. In the Apollo 15 and 17 samples, the downslope slumping and lateral transport from nearby high relief regions are a likely cause for the larger non-mare component. At the Apollo 12 sampling site, the ejecta of the nearby crater Copernicus, that not only delivered a non-mare component but excavated local material, could increase the regional non-mare concentration. The low amount of non-mare material contained in the Apollo 11, Luna 16 and 24 mare soil samples may result from the gradual accumulation of both the lateral and vertical mixing. In addition, the region where Luna 16 landed may have a very thin mare deposit.

In the future, a model involving topographic relief could be further developed to assess the influence of highland slumping. In addition, with greater understanding of the distribution of distal ejecta, the model could consider some realistic young craters of interest, such as crater Copernicus, and get a more reliable picture of non-mare distribution.

Without a well-constrained estimate of volcanic eruption flux, we performed tentative simulations with the varying mare thickness, the peak time of mare eruption and the cessation time of the major mare filling. It is found that on the surface, the total amount of mare deposit can significantly change the abundance of vertically delivered non-mare, but does not influence the abundance of the laterally transported non-mare material; the peak time of mare eruption could not significantly affect the abundance of both laterally and vertically transported component; the cessation time of the major mare fillings is the major factor altering the abundance of laterally transported non-mare material, and it could also affect the fraction of the buried vertically transported non-mare material that had ever been excavated to the near-surface.

Acknowledgments: We gratefully acknowledge David Minton and Noah Petro for their careful reviews of the manuscript and discussions about cratering processes and formation of impact ejecta with Robert Luther. This work was supported by German Research Foundation (DFG) SFB TRR-707 170-1 TP A4. This is TRR 170 contribution 123.

6.8. Supplementary material

In this supplementary file, we present the influence of the choice of h_{min}, the distribution of non-mare component with the varying parameters concerning the mare filling.

6.8.1. Effect of the different choice of h_{min}

For each impact cratering event, the farthest ejecta that the model would trace have the minimum deposit thickness (h_{min}). The smaller the value of h_{min}, the larger the traced range of ejecta deposit. The results of Y. Huang et al. (2017) present the importance of distal ejecta on

the non-mare mixing. But the very farther ejecta possess less volume which may not induce the significant difference on the non-mare abundance. In the main text, the value of h_{min} is taken to be 0.01 m.

The simulations where the value of h_{min} varies but all the other parameters are the same are performed as those described in the section 6.2 of the main text: the spatial distribution of impact events is the same as that shown in Figure 36; the mare thickness is H_{DeHon}; the cessation time of the major mare flooding is t_{end}; the peak time of the mare eruptions is 3.8 Ga. The results show that when the greater value is taken, the non-mare distribution over the mare regions is distinctly bias from that on the realistic lunar surface. When the smaller value is taken, it presents no significant difference from that with h_{min} of 0.01 m.

Figure 39 presents the average fraction of vertically and laterally transported non-mare component in different depths when different value of h_{min} is taken. Comparing with that from the model with h_{min} of 0.01 m, when h_{min} is ten times greater (i.e., 0.1 m), the fraction of vertically and laterally transported non-mare component in the top meter is decreased by 0.01 and 0.06, respectively. When h_{min} is ten times smaller (i.e., 0.001 m), the difference of the vertically and laterally transported non-mare fraction in the top meter is less than 0.02 and 0.004, respectively.

In addition, it shows that the difference is getting smaller with the increasing depth. In the top 5 m, when h_{min} is ten times greater (i.e., 0.1 m), the difference of the fraction of vertically and laterally transported non-mare component is 0.05 and 0.01, respectively. When h_{min} is ten times smaller (i.e., 0.001 m), the difference of the vertically and laterally transported non-mare fraction is less than 0.001 and 0.005, respectively.

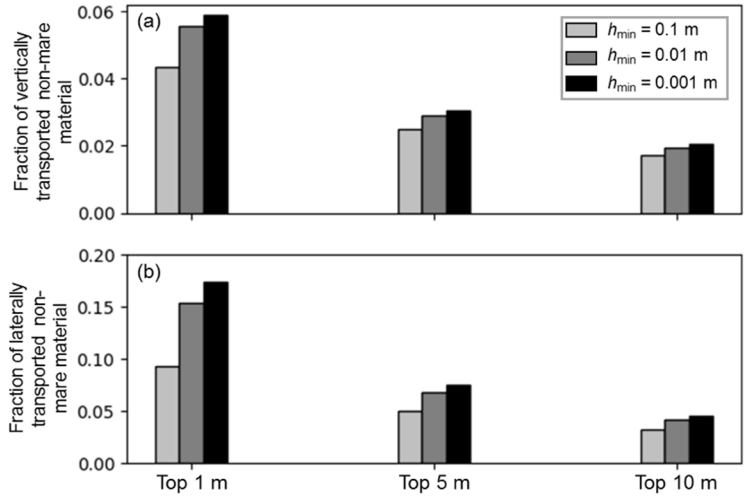

Figure 39 The average vertically (a) and laterally (a) transported non-mare material in the top 1, 5, and 10 m over the mare regions when the different value of h_{min} is taken.

Figure 40 and Figure 41 present the spatial distribution of vertically and laterally transported non-mare component in the different depth when the various value of h_{min} is taken. It shows that when the greater h_{min} is taken, the interior mare regions appear no mixing of both vertically and laterally transported non-mare component. When the smaller value of h_{min} is taken, the major difference also distributes over the interior domains of mare regions, but the difference of fraction is mostly smaller than ~0.001, which is smaller than the accuracy that the current research can reach.

Therefore, both the statistical and spatial distribution of non-mare components suggest that the h_{min} of 0.01 m is reasonable for the current study (the minimum crater diameter is 5 km).

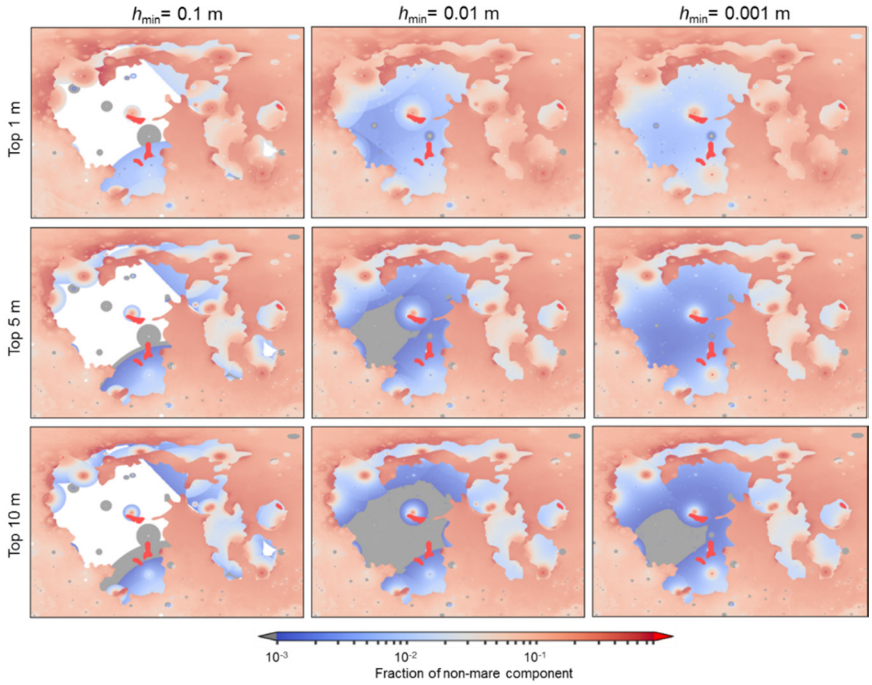

Figure 40 The spatial distribution of vertically transported non-mare component in the top 1, 5 and 10 m when the different values of h_{min} are taken.

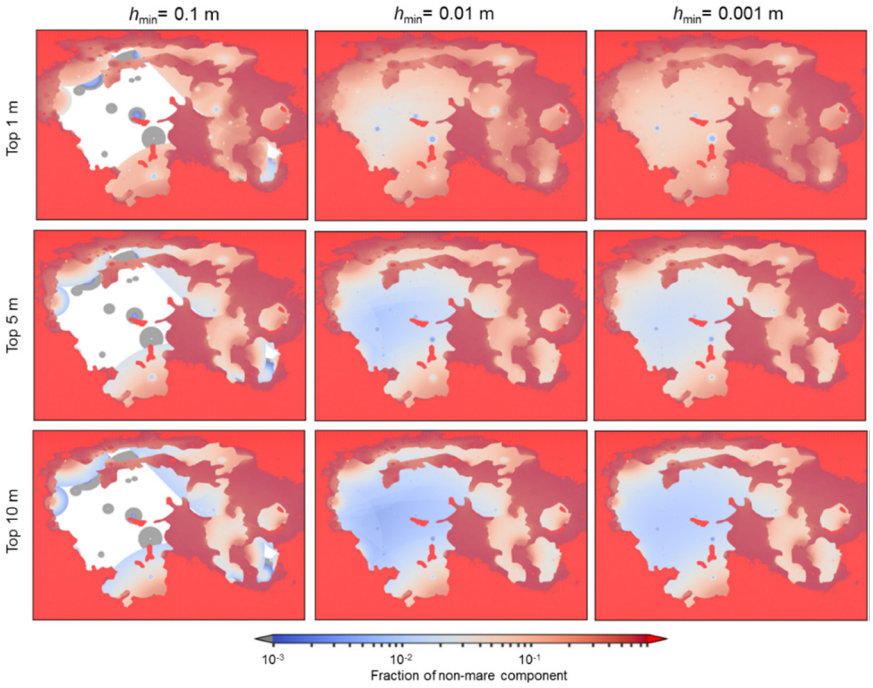

Figure 41 The spatial distribution of laterally transported non-mare component in the top 1, 5 and 10 m when the different values of h_{min} are taken.

6.8.2. Simulations results with the varying parameters concerning mare filling

The spatial distributions of non-mare component in the top 5 m with the varying parameters concerning mare filling, including the mare thickness, the cessation time and the peak time of mare eruption are shown in Figure 42, Figure 43 and Figure 44 respectively. The statistical distribution of the non-mare component with the varying parameters is summarized in Table 11.

6.8.2.1. Simulations with varying mare thickness

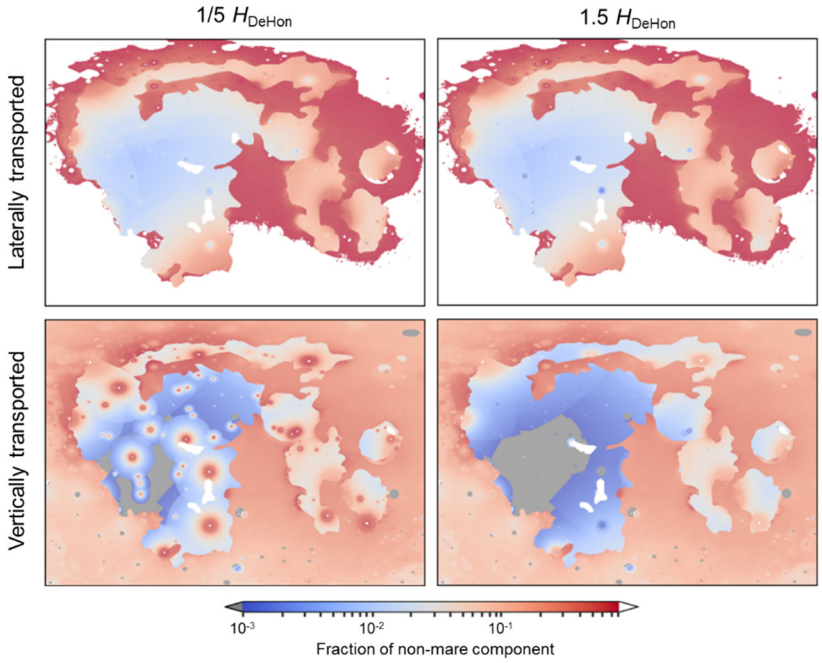

Figure 42 The spatial distributions of non-mare component in the top 5 m when different thickness of mare deposit is taken into account.

6.8.2.2. Simulations with varying cessation time of the major mare filling

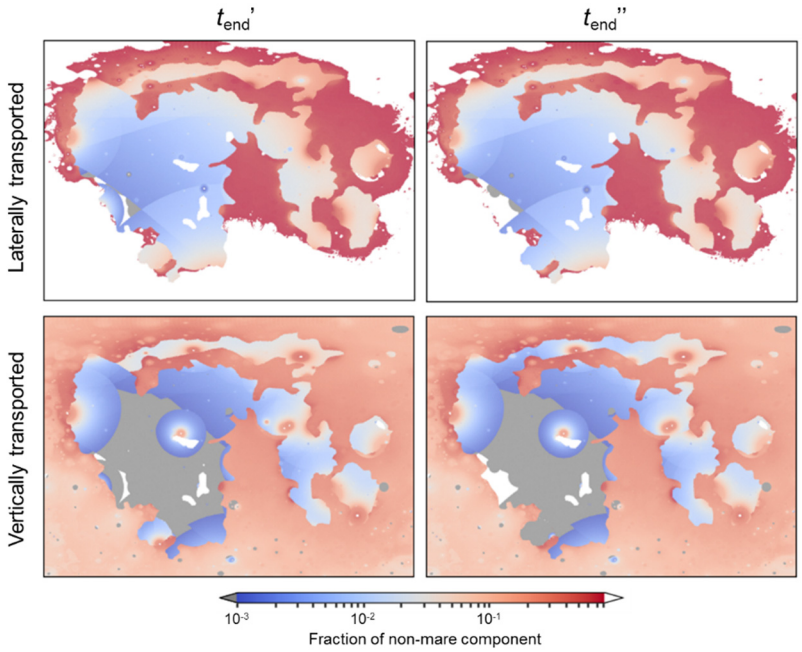

Figure 43 The spatial distributions of non-mare component in the top 5 m when the different cessation time of the major mare filling is taken into account.

6.8.2.3. Simulation with the younger peak time of mare eruption

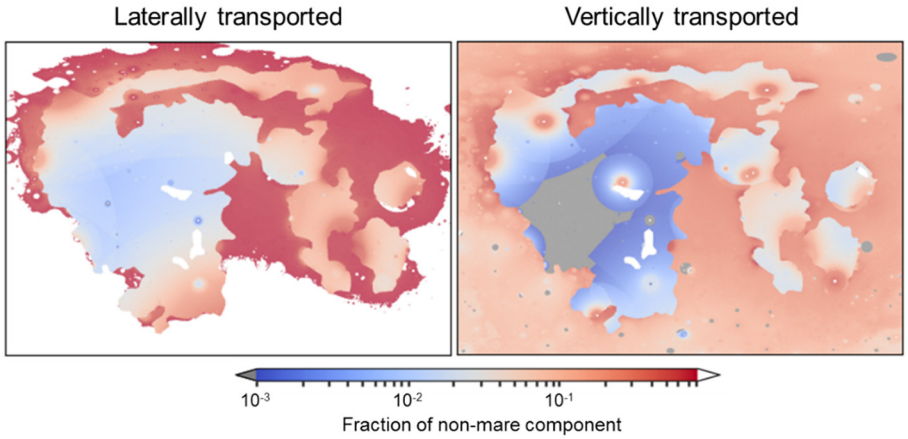

Figure 44 The spatial distributions of non-mare component in the top 5 m when the younger peak time of mare eruption (3.3 Ga) is taken into account.

Table 11 Statistics of non-mare fraction in the top 5 m when the difference parameters are taken.

			Simulations					
Parameter studied	Mare thickness		H_{DeHon}	$1/5H_{\mathrm{DeHon}}$	$1.5H_{\mathrm{dehon}}$	H_{DeHon}		H_{DeHon}
	Cessation time of eruptions		t_{end}	t_{end}		t_{end}'	t_{end}''	t_{end}
	Peak time of eruptions (Ga)		3.8	3.8		3.8		3.3
Non-mare fraction	Laterally transported	Mean	0.07	0.07	0.07	0.04	0.03	0.07
		Quartile	$0.03^{0.10}_{0.01}$	$0.03^{0.10}_{0.01}$	$0.03^{0.10}_{0.01}$	$0.01^{0.04}_{0.005}$	$0.01^{0.04}_{0.005}$	$0.03^{0.10}_{0.013}$
	Vertically transported	Mean	0.03	0.06	0.02	0.02	0.02	0.03
		Quartile	$0.006^{0.03}_{0.002}$	$0.02^{0.06}_{0.004}$	$0.003^{0.02}_{0.001}$	0.002^{3e-3}_{3e-4}	$0.002^{0.01}_{7e-4}$	$0.006^{0.03}_{0.002}$

7. Discussion

7.1. Sensitivity to the uncertainty in scaling laws

The thickness distribution of ejecta and impact melt in ejecta follows the power laws. The typical exponent values are taken in this thesis. The ejecta thickness follows: $\delta(r) = \mathrm{a}r^{-3.0}$ and the melt thickness in ejecta follows: $\delta_m = a_m r^{-2.0}$, where r is the distance to the crater center and a and a_m are both constant. Previous studies show that various conditions of impact events (e.g., different thermal conditions and properties of the target, impact angle, and impact velocity) could make the slope of the power laws deviate from the typical values. The uncertainty of exponent value for thickness distribution of melt and ejecta could range from -1.8 to -2.2 and from -2.5 to -3.5 (section 3.3), respectively.

To investigate the model sensitivity to the uncertainty in the scaling laws of ejecta distribution, two additional simulations where the exponent of melt thickness distribution is unchanged, but the exponent of ejecta thickness distribution is taken to be -2.5 and -3.5 are performed. For a single impact event, when the exponent value is -3.5 (-2.5), there is more (less) ejected material deposited near the rim. But the uncertainty of ejecta distribution does not significantly change the statistical melt distribution over the global surface. Compared with Figure 24c, both simulations result in the difference of relative melt fraction in the near-surface smaller than 0.3. For the melt younger than 3 Ga, the difference is smaller than 0.01 (Figure 45a). Similarly, to investigate the model sensitivity to the uncertainty in the scaling laws of melt distribution, two simulations where the exponent of ejecta thickness distribution is unchanged, but the exponent of melt thickness distribution is taken to be -1.8 and -2.2 are performed. For a single impact event, when the exponent value is -2.2 (-1.8), there is more (less) ejected melt material deposited near the rim. But its influence on the statistical melt distribution over the global surface is not distinct as well. Compared with Figure 24c, both the simulations result in the difference of relative melt fraction in the near-surface mostly smaller than 0.1. For the melt younger than 3 Ga, the difference is smaller than 0.01 (Figure 45b).

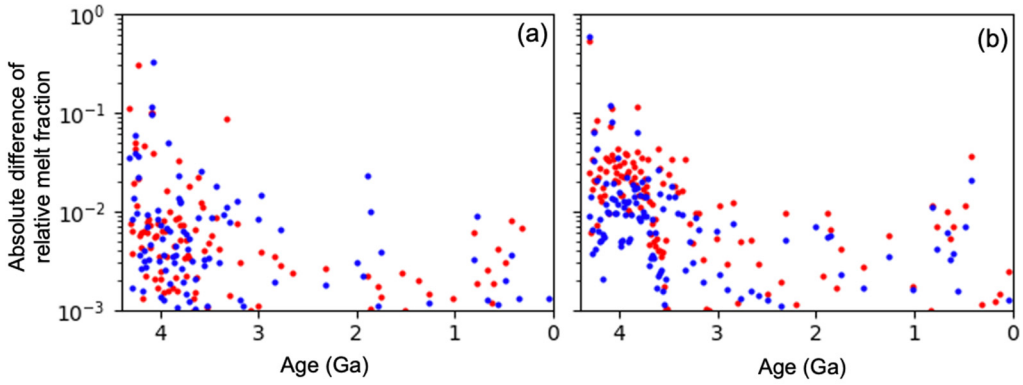

Figure 45 The difference of relative melt distribution of the near-surface compared with the result of Figure 24c when (a) the exponent of melt thickness distribution is typical value, but the exponent of ejecta thickness distribution is taken to be -2.5 (blue dots) and -3.5 (red dots); (b) the exponent of ejecta thickness distribution is typical value, but the exponent of melt thickness distribution is taken to be -1.8 (blue dots) and -2.2 (red dots).

7.2. Key findings

In this thesis, a numerical model was developed to investigate the spatial diffusion of surface material with long-time impact mixing. Many simulations were run for a common purpose: to provide a quantitative context for the interpretation of the returned lunar samples. Figure 46 presents the relationship of the key findings.

The presence and abundance of impact melt were investigated first. The lateral diffusion behavior of the impact melt was presented in the results of the 2D model (Paper I). In this study, the impact melt of three mid- to late-forming basins was particularly investigated. The work demonstrated the expected abundant Imbrium melt mixed into the Apollo and Luna samples.

Then, a more complete picture of the diffusion pattern was obtained when the model was further developed into three dimensions (Paper II). A more complete list of basin-forming events was involved in the simulations. The spatial distributions of all these basins were estimated. The mixture of the ejecta of different basin origins was recorded and their relative abundance in the samples was calculated. As for the 2D model, the simulation results of the 3D model also show a significant mixing of Imbrium ejecta in the collected samples. In addition, this study predicts a large amount of the ancient impact melt that has not been found in the collected samples. This old impact melts in the samples are suggested to be dated based on a different chronometer with the higher close temperature, such as U-Pb system.

The key findings of both 2D and 3D models indicate that the clustering of isotopic ages of ancient lunar impactites from the Apollo and Luna landing sites at ~3.9 Ga was likely to have been caused by the mixing of Imbrium ejecta into the sampled material. It is, therefore, not necessary to have a surge in the impact rate at about this time, the so-called terminal cataclysm. The numerical simulations of the evolution of small bodies have also been used to investigate

different scenarios of late bombardment history. These simulations are constrained by the abundance of the high siderophile elements (HSEs) in the lunar mantle. Morbidelli et al. (2018) revisit the previous work that examined which scenario could be compatible with both the lunar crater record and the abundance of HSE in the lunar mantle. This study came to the same conclusion: there is no need for a late surge in the bombardment.

Using the 3D model, the spatial diffusion of the different components of samples can be investigated (Paper III). Since the origin of the non-mare component in the lunar mare samples has been debated for decades, this model was then applied to trace the evolving distribution of non-mare material on the surface of the maria. It was found that almost the entirety of the mare regions is mixed with both laterally- and vertically-derived non-mare material and the fractional presence in the top meter is ~0.1. The mare samples that contain a significant abundance (>~50%) of non-mare material are suggested to be explained by geologic processes not accounted for, such as the downslope slumping of the nearby massif, the disturbance of the ejecta of craters that excavated many non-mare materials, the sampling strategy of astronauts, and the selection bias of geochemistry analysis.

The simulations can provide informative context when selecting future sampling sites. The zones inside the basins that have been excavated by later impacts are expected to be the most fruitful place to collect the ancient material no matter whether it was covered by the thick ejecta of later-formed basin event.

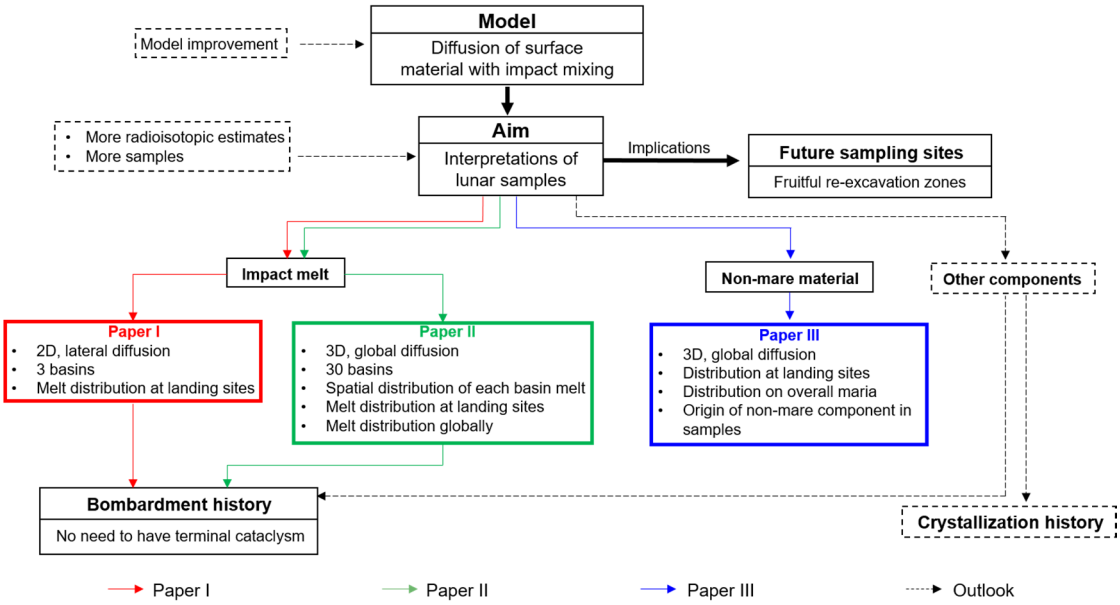

Figure 46 Key results and outlook of this thesis.

7.3. Outlook

7.3.1. Refinements of the model

Small impact craters with a diameter smaller than 5 km were not taken into account in the developed model. This model can be improved by involving the impact mixing of small craters to further constrain the distribution of impact melt. Due to the great number of small craters (Neukum, 1983), smaller regional areas, rather than a global surface, would be simulated. The area should be large enough for the occurrence of craters > ~1 km. Taking the occurrence of craters of 1 km in diameter as an example, in the last 3 Ga, few such craters would present over areas smaller than ~100 km^2. However, the number of impact events would be highly increased with the increasing area lowering the model efficiency. Overlying areas with different sizes would be used to reach the compromise between the occurrence of the large craters and the limit of the number of small craters. The obtained gardening features of smaller craters would finally be integrated into the current 3D model. This research is now in preparation.

This study indicates that once the melt of basins is formed, the subsequent gardening of the smaller impacts cannot significantly change its distribution. The predicted distribution of basin melts mainly lies on the applied scaling law. However, the ejecta and melt distribution of basin-forming events are complicated and it varied according to the Moon's status (e.g., the varying thermal condition of the Moon). Zhu et al. (2017) investigated how different temperature gradients of the Moon affect the ejection of molten materials for impact basins several hundred kilometers in diameter. They found that the ejecta thickness and melt content are sensitive to the thermal properties of the target. For a "warm" target, the ejecta thickness with radial distance declines faster than for a "cold" target. The impact on the warm target produces more molten ejecta than that on the cold target. Therefore, thermal effects on the ejecta thickness distribution should be considered while investigating large impact basins, especially for basins formed shortly after the planet's formation, when the planets are thought to be much warmer. In the future, the distribution of basin ejecta will be systematically studied, the obtained distribution features will then be embedded into the model to better constrain the melt distribution.

Some other scaling laws of impact cratering remain to be further studied as well, most importantly the scaling laws of the melt distribution in the ejecta. These scaling laws shown in section 3.3 are the preliminary result. The more systematic simulations with the various impact conditions are required to better constrain the melt distribution. If the small craters are involved, since most of them form in the surface regolith that possesses a high porosity, the scaling law considering the target porosity may also be required. These scaling laws will be studied using

iSALE Eulerian shock physics code (Wünnemann et al., 2006), which are the main goals of my current postdoc researches.

7.3.2. Application of the model

The developed 3D model simulates the long-time gardening process. In this thesis, it is applied to trace the diffusion of impact melt, and mare/non-mare material. In the next step, the 3D model will be further developed to investigate the mixing with other ejecta (Figure 46). Compositional information will be included to track compositional changes during mixing. On the basis of the FeO and Th abundances measured by the Clementine and Lunar Prospector missions, the lunar crust is divided into three major terranes (Stöffler, 2006): (1) the Feldspathic Highlands Terrane (FHT) (2) the Procellarum KREEP Terrane (PKT) and the South Pole-Aitken Terrane (SPAT). These three types of terranes have distinctive compositions. Taking thorium concentration as an example, it is greater than 3 ppm in the PKT, while less in SPAT and FHT with values of 1.5-3.5 and <1.5 ppm, respectively. By tracing the diffusion of the material of different types of terrane, the variation of diverse constituents could be estimated over the lunar surface and at regions of particular interest, such as the sampling sites. The simulated distribution of different components could provide constraints on the modeling of the crystallization of the lunar magma ocean.

The nature of the lunar impact flux has been a topic of enduring concern (Figure 2) for the planetary science and astrobiology communities. The developed model will be used to further constrain the lunar impact flux. Different scenarios of impact flux can be embedded into the model, which would lead to various predictions of melt distribution. By comparing the corresponding results with the radioisotopic ages of lunar samples, the most plausible scenario of impact flux will be proposed.

This model can also be particularly applied to study the growth history of lunar regolith that results from the cumulative comminution of surface rocks by impact mixing. Almost all our knowledge of the Moon derives from its surface by in situ samplings, physical experiments, and remote sensing (our knowledge of lunar regolith is summarized in McKay et al., 1991). Until lunar samples were returned by the Apollo missions, our understanding of the Moon was severely limited since meteorites had been the only extraterrestrial materials available for laboratory analysis. In the aspect of its composition, there had been speculation that the Moon might be an ancient body and unaffected by the terrestrial processes of segregation into crust, mantle, and core. The Apollo samples provided ample evidence for over a billion years of planetary evolution, showing that intense igneous activity has altered the Moon since its origin. In the aspect of physical properties, before the launch of the Apollo missions, some scientists were concerned that the lunar regolith would be too light and powdery to support the weight of

the lunar lander. They were worried that the lander would sink down into it. However, landings performed by robotic Surveyor spacecraft showed that the lunar soil was firm enough to support a spacecraft.

The returned lunar samples have greatly improved the knowledge of lunar regolith, but there are still many questions that have only been partially studied. What is the origin of regolith? How does regolith grow with time? How has the extent of mixing varied as a function of time? By considering smaller impact events, the model developed here may be further applied to investigate those questions. To address those questions, the impact mixing of small craters should be considered in the model. Each impact event generates fragmental ejecta and distributes it near the crater rim. Although the scaling law concerning the distribution of fragment material is not available so far, the relative degree of fragmentation could be estimated. The more impact gardening events occur, the smaller the relative size of the fragments. The impact frequency at different locations and depths is changing with time resulting in a very complicated picture in the present day. By tracing the frequency of fragmentation at different time, the evolution of regolith thickness through time can be calculated and the relative growth rate of fragmental regolith during the different time period can be determined.

7.3.3. More constrains of radioisotopic data

A number of radioisotopic datings of impact melt contained in the samples have been performed using K-Ar techniques (section 2.3.2). The distribution of the K-Ar ages displays a bulge at ~3.9 Ga, and the less old melt was found. The modeling results in this thesis suggest that there is probably a significant amount of old melt in the collected samples. The deficiency of the old melt in the K-Ar ages could be caused by the restrictions of the dating technique (the further discussions in section 5.4). For example, due to the extensive impact mixing, the grain size of the old impact melt could be too small to maintain enough Ar for the proper K-Ar age dating. In addition, the context of the small grains is difficult to determine, and hence the origin of impacts or volcanism is uncertain. Using different chronometer systems, the more ancient impact melt is likely to be found. New U-Pb data, for example, obtained by in situ methods on minerals that have a high close temperature (e.g., zircon and baddeleyite) provides evidence for the occurrence of impact events at ~4.2-4.3 Ga (Vanderliek et al., 2018), which further imply the survival of the old impact melt in the returned samples. Therefore, more isotopic dating using different chronometer systems may help to find the older impact melt in the future.

More samples will be brought back from the Moon. China's Chang'e-5 mission, for example, has recently returned ~2 kg samples from the Moon (C. Li et al., 2019; Zou & Li, 2017). These samples were collected from the regions that have not yet been investigated which could provide new clues to our understanding of the lunar bombardment history. For the sampling

missions that are located far away from the Imbrium basin, the composition of the collected material probably has not been altered by the Imbrium ejecta. The distribution of radioisotopic ages of the impact melts in the collected samples could compare with that of the Apollo and Luna missions to see whether it still presents the similar grouped ages of ~3.9 Ga. Particularly if the landing sites are located on the SPA basin, which is believed to be the oldest giant impact on the Moon, it is likely to find its ancient SPA melt (Wieczorek et al., 2012), which would provide constraints of the early bombardment history with an important pinpoint.

8. Synthesis

The aim of this thesis was to establish a spatially-resolved numerical model to investigate the diffusion of different components of material caused by the cumulative effect of impact mixing. The modeling results can provide a more precise statistical analysis of the mixing of different components at sampling sites, and hence can help interpretations of collected samples. Since impact melts record the occurrence time of the impacts, they can be the key to understanding the bombardment history and are thus the major focus of this thesis.

Paper I presents a first-developed 2D model focusing on the lateral diffusion features of surface material. The evolving history of impact melt with different ages along a path on the lunar surface was obtained. Paper II shows the development of a 3D model presenting a more complete picture of the surface material's evolution. Based on this model, the melt composition was examined over the whole of the Moon and in particular at the sampling sites. The findings of the 3D model support the results of 2D while providing more inspirations for sample interpretations.

The predicted abundance of impact melt with different ages in both Paper I and Paper II was compared with the radioisotopic ages of the lunar samples. This aids our understanding of the survival probability of basin melt and thus makes more secure links between measured samples and particular basin-forming impact events. The results of both 2D and 3D model indicate a significant mixing of Imbrium melt in the collected samples which likely lead to the grouped radioisotopic ages of 3.9 Ga. In addition, the old basin melts are hardly detected in the samples. This thesis (Paper II) suggests abundant old basin melts at sampling sites and these old basin melts are probably found using new radioisotopic techniques.

In Paper III, with the developed 3D model, the process of volcanic flooding over the mare regions that was not considered in Paper I and II was finally taken into account. The abundance of the mare and non-mare material was calculated. The ratio of local-origin to foreign-origin non-mare components in the mare soil samples was inferred. In addition, the results display the mixing of the non-mare components over the overall maria surface, indicating that future missions aiming to collect samples on the maria should at least contain some non-mare material. The predicted non-mare concentration is generally consistent with that of samples. It indicates the robustness of the developed model which further confirms the model's capability of being applied to the other components of interest in the future.

9. Bibliography

Abramov, O., Wong, S. M., & Kring, D. A. (2012). Differential melt scaling for oblique impacts on terrestrial planets. *Icarus*, *218*(2), 906–916. https://doi.org/10.1016/j.icarus.2011.12.022

Ahrens, T. J., & O'Keefe, J. D. (1977). Equations of state and impact-induced shock-wave attenuation on the moon. In *Impact and Explosion Cratering* (pp. 639–656). https://doi.org/10.1063/1.1745670

Arvidson, R., Drozd, R. J., Hohenberg, C. M., Morgan, C. J., & Poupeau, G. (1975). Horizontal transport of the regolith, modification of features, and erosion rates on the lunar surface. *The Moon*, *13*(1–3), 67–79. https://doi.org/10.1007/BF00567508

Baldwin, R. B. (1974). Was there a "terminal lunar cataclysm" 3.9-4.0×109 years ago? *Icarus*, *23*(2), 157–166. https://doi.org/10.1016/0019-1035(74)90003-7

Baldwin, R. B. (1987). On the relative and absolute ages of seven lunar front face basins: I. From Viscosity Arguments. *Icarus*, *71*(1), 1–18. https://doi.org/https://doi.org/10.1016/0019-1035(87)90158-8

Bence, A. E., & Grove, T. L. (1978). The Luna 24 highland component. *Mare Crisium: The View from Luna 24*, 429–444.

Bottke, W. F., & Norman, M. D. (2017). The late heavy bombardment. *Annual Review of Earth and Planetary Sciences*, *45*(1), 619–647. https://doi.org/10.1146/annurev-earth-063016-020131

Bottke, W. F., Vokrouhlický, D., Minton, D., Nesvorný, D., Morbidelli, A., Brasser, R., Simonson, B., & Levison, H. F. (2012). An Archaean heavy bombardment from a destabilized extension of the asteroid belt. *Nature*, *485*(7396), 78–81. https://doi.org/10.1038/nature10967

Budney, C. J., & Lucey, P. G. (1998). Basalt thickness in Mare Humorum: The crater excavation method. *Journal of Geophysical Research: Planets*, *103*(E7), 16855–16870. https://doi.org/10.1029/98JE01602

Canup, R. M., & Asphaug, E. (2001). Origin of the Moon in a giant impact near the end of the Earth's formation. *Nature*, *412*(6848), 708–712. https://doi.org/10.1038/35089010

Cassata, W. S., Renne, P. R., & Shuster, D. L. (2009). Argon diffusion in plagioclase and implications for thermochronometry: A case study from the Bushveld Complex, South Africa. *Geochimica et Cosmochimica Acta*, *73*(21), 6600–6612. https://doi.org/https://doi.org/10.1016/j.gca.2009.07.017

Chapman, C. R., Cohen, B. A., & Grinspoon, D. H. (2007). What are the real constraints on the existence and magnitude of the late heavy bombardment? *Icarus*, *189*(1), 233–245. https://doi.org/10.1016/j.icarus.2006.12.020

Cintala, M. J., & Grieve, R. A. F. (1998). Scaling impact melting and crater dimensions: Implications for the lunar cratering record. *Meteoritics and Planetary Science*, *33*(4), 889–912. https://doi.org/10.1111/j.1945-5100.1998.tb01695.x

Cohen, B. A. (2000). Support for the lunar cataclysm hypothesis from lunar meteorite impact melt ages. *Science*, *290*(5497), 1754–1756. https://doi.org/10.1126/science.290.5497.1754

Cohen, B. A., Petro, N. E., Lawrence, S. J., Clegg, S. M., Denevi, B. W., Dyar, M. E., Elardo, S. M., Grinspoon, D. H., Hiesinger, H., Liu, Y., McCanta, M. C., Moriarty, D. P., Norman, M. D., Runyon, K. D., Schwenzer, S. P., Swindle, T. D., van der Bogart, C. H., & Wiens, R. C. (2018). Curie: Constraining solar system bombardment using in situ radiometric dating. *49th Lunar and Planetary Science Conference*. http://oro.open.ac.uk/53545/

Cooper, B. L., Carter, J. L., & Sapp, C. A. (1994). New evidence for graben origin of Oceanus Procellarum from lunar sounder optical imagery. *Journal of Geophysical Research: Planets*, *99*(E2), 3799–3812. https://doi.org/10.1029/93JE03096

Croft, S. K. (1985). The scaling of complex craters. *Journal of Geophysical Research Supplement*, *90*(S02), C828–C842. https://doi.org/10.1029/JB090iS02p0C828

Dalrymple, G. B., & Ryder, G. (1996). Argon-40/argon-39 age spectra of Apollo 17 highlands breccia samples by laser step heating and the age of the Serenitatis basin. *Journal of Geophysical Research: Planets*, *101*(E11), 26069–26084. https://doi.org/10.1029/96JE02806

Dasch, E. J., Shih, C.-Y., Bansal, B. M., Wiesmann, H., & Nyquist, L. E. (1987). Isotopic analysis of basaltic fragments from lunar breccia 14321: Chronology and petrogenesis of pre-Imbrium mare volcanism. *Geochimica et Cosmochimica Acta*, *51*(12), 3241–3254. https://doi.org/10.1016/0016-7037(87)90132-3

De Hon, R. A. (1974). Thickness of mare material in the Tranquillitatis and Nectaris basins. *Lunar and Planetary Science Conference Proceedings*, *5*, 53–59.

De Hon, R. A. (1979). Thickness of western mare basalts. *Proceedings of the 10th Lunar and Planetary Science Conference*, 2935–2955.

De Hon, R. A., & Waskom, J. D. (1976). Geologic structure of the eastern mare basins. *Lunar and Planetary Science Conference Proceedings*, *3*, 2729–2746.

Dence, M. R., Douglas, J. A. V, Plant, A. G., & Traill, R. J. (1971). Mineralogy and petrology of some Apollo 12 samples. *Lunar and Planetary Science Conference Proceedings*, *2*, 285.

Deutsch, A., & Stöffler, D. (1987). Rb-Sr-analyses of Apollo 16 melt rocks and a new age estimate for the Imbrium basin: Lunar basin chronology and the early heavy bombardment of the moon. *Geochimica et Cosmochimica Acta*, *51*(7), 1951–1964. https://doi.org/10.1016/0016-7037(87)90184-0

Du, J., Fa, W., Wieczorek, M. A., Xie, M., Cai, Y., & Zhu, M.-H. (2019). Thickness of lunar mare basalts: New results based on modeling the degradation of partially buried craters. *Journal of Geophysical Research: Planets*, *124*, 1–30. https://doi.org/10.1029/2018JE005872

Duncan, A. R., Sher, M. K., Abraham, Y. C., Erlank, A. J., Willis, J. P., & Ahrens, L. H. (1975). Interpretation of the compositional variability of Apollo 15 soils. *Lunar and Planetary Science Conference Proceedings*, *2*, 2309–2320.

Elliott, J. R., Huang, Y.-H., Minton, D. A., & Freed, A. M. (2018). The length of lunar crater rays explained using secondary crater scaling. *Icarus*, *312*, 231–246. https://doi.org/https://doi.org/10.1016/j.icarus.2018.04.015

Evans, A. J., Soderblom, J. M., Andrews-Hanna, J. C., Solomon, S. C., & Zuber, M. T. (2016). Identification of buried lunar impact craters from GRAIL data and implications for the nearside maria. *Geophysical Research Letters*, *43*(6), 2445–2455. https://doi.org/10.1002/2015GL067394

Fa, W., & Jin, Y. Q. (2010). A primary analysis of microwave brightness temperature of lunar surface from Chang-E 1 multi-channel radiometer observation and inversion of regolith layer thickness. *Icarus*, *207*(2), 605–615. https://doi.org/10.1016/j.icarus.2009.11.034

Fa, W., Liu, T., Zhu, M.-H., & Haruyama, J. (2014). Regolith thickness over Sinus Iridum: Results from morphology and size-frequency distribution of small impact craters. *Journal of Geophysical Research E: Planets*, *119*(8), 1914–1935. https://doi.org/10.1002/2013JE004604

Farrand, W. H. (1988). Highland contamination and minimum basalt thickness in northern Mare Fecunditatis. *Lunar and Planetary Science Conference Proceedings*, *18*, 319–329.

Fassett, C. I., Head, J. W., Kadish, S. J., Mazarico, E., Neumann, G. A., Smith, D. E., & Zuber, M. T. (2012). Lunar impact basins: Stratigraphy, sequence and ages from superposed impact crater populations measured from Lunar Orbiter Laser Altimeter (LOLA) data. *Journal of Geophysical Research: Planets*, *117*(2), 1–13. https://doi.org/10.1029/2011JE003951

Fernandes, V. A., Fritz, J., Weiss, B. P., Garrick-Bethell, I., & Shuster, D. L. (2013). The bombardment history of the Moon as recorded by 40 Ar-39 Ar chronology. *Meteoritics and Planetary Science*, *48*(2), 241–269. https://doi.org/10.1111/maps.12054

Fischer, E. M., & Pieters, C. M. (1995). Lunar surface aluminum and iron concentration from Galileo solid state imaging data, and the mixing of mare and highland materials. *Journal of Geophysical Research*, *100*(E11), 23279. https://doi.org/10.1029/95JE02359

Flude, S., Halton, A. M., Kelley, S. P., Sherlock, S. C., Schwanethal, J., & Wilkinson, C. M. (2014). Observation of centimetre-scale argon diffusion in alkali feldspars: implications for 40Ar/39Ar thermochronology. *Geological Society, London, Special Publications*, *378*(1), 265–275.

French, B. M. (1998). Traces of catastrophe: A handbook of shock metamorfic effects in terrestial meteorite impact structure. *Technical Report, LPI-Contrib-954*, *954*, 120.

Frey, H. (2011). Previously unknown large impact basins on the Moon: Implications for lunar stratigraphy. *Geological Society of America Special Papers*, *477*, 53–75.

Gault, D. E., Quaide, W. L., & Oberbeck, V. R. (1968). *Impact cratering mechanics and structure, Shock Metamorphism of Natural Materials, edited by BM French and NM Short*. Mono Books, Baltimore, Md.

Gomes, R., Levison, H. F., Tsiganis, K., & Morbidelli, A. (2005). Origin of the cataclysmic late heavy bombardment period of the terrestrial planets. *Nature*, *435*, 466.

Gong, S., Wieczorek, M. A., Nimmo, F., Kiefer, W. S., Head, J. W., Huang, C., Smith, D. E., & Zuber, M. T. (2016). Thicknesses of mare basalts on the Moon from gravity and topography. *Journal of Geophysical Research: Planets*, *121*(5), 854–870. https://doi.org/10.1002/2016JE005008

González, Á. (2010). Measurement of areas on a sphere using Fibonacci and Latitude–Longitude Lattices. *Mathematical Geosciences*, *42*(1), 49–64. https://doi.org/10.1007/s11004-009-9257-x

Grange, M. L., Nemchin, A. A., & Jourdan, F. (2010). Review of ages of lunar impact rocks: Implication to the timing of Serenitatis and Imbrium impacts and the LHB model. *Lunar and Planetary Science Conference*, *41*, 1275.

Grieve, R. A. F., & Cintala, M. J. (1992). An analysis of differential impact melt-crater scaling and implications for the terrestrial impact record. *Meteoritics*, *27*(5), 526–538. https://doi.org/10.1111/j.1945-5100.1992.tb01074.x

Hartmann, W. K. (1970). Lunar cratering chronology. *Icarus*, *13*(2), 299–301. https://doi.org/10.1016/0019-1035(70)90059-X

Hartmann, W. K. (1975). Lunar "cataclysm": A misconception? *Icarus*, *24*(2), 181–187. https://doi.org/10.1016/0019-1035(75)90095-0

Hartmann, W. K. (1995). Planetary cratering I: Lunar highlands and tests of hypotheses on crater populations. *Meteoritics*, *30*, 451.

Hartmann, W. K. (2003). Megaregolith evolution and cratering cataclysm models—Lunar cataclysm as a misconception (28 years later). *Meteoritics & Planetary Science*, *38*(4), 579–593. https://doi.org/10.1111/j.1945-5100.2003.tb00028.x

Hartmann, W. K., Quantin, C., & Mangold, N. (2007). Possible long-term decline in impact rates. 2. Lunar impact-melt data regarding impact history. *Icarus*, *186*(1), 11–23. https://doi.org/10.1016/j.icarus.2006.09.009

Haskin, L. A. (1998). The Imbrium impact event and the thorium distribution at the lunar highlands surface. *Journal of Geophysical Research: Planets*, *103*(E1), 1679–1689. https://doi.org/10.1029/97JE03035

Haskin, L. A., Korotev, R. L., Rockow, K. M., & Jolliff, B. L. (1998). The case for an Imbrium origin of the Apollo thorium-rich impact-melt breccias. *Meteoritics and Planetary Science*, *33*(5), 959–975. https://doi.org/10.1111/j.1945-5100.1998.tb01703.x

Hawke, B. R., & Bell, J. F. (1982). Remote sensing studies of lunar dark-halo impact craters: preliminary results and implications for early volcanism. *Lunar and Planetary Science Conference Proceedings*, *12*, 665–678.

Head, J. W. (1976). Lunar volcanism in space and time. In *Reviews of Geophysics* (Vol. 14, Issue 2, pp. 265–300). https://doi.org/10.1029/RG014i002p00265

Head, J. W. (1982). Lava flooding of ancient planetary crusts: Geometry, thickness, and volumes of flooded lunar impact basins. *The Moon and the Planets*, *26*(1), 61–88. https://doi.org/10.1007/BF00941369

Head, J. W. (2001). The Moon and terrestrial planets: geology and geophysics. In J. A. M. Bleeker, J. Geiss, & M. C. E. Huber (Eds.), *The Century of Space Science* (pp. 1295–1323). Springer Netherlands. https://doi.org/10.1007/978-94-010-0320-9_54

Head, J. W. (1977). Origin of outer rings in lunar multi-ringed basins: evidence from morphology and ring spacing. In D. J. Roddy, R. O. Pepin, & R. B. Merrill (Eds.), *Impact and Explosion Cratering: Planetary and Terrestrial Implications* (pp. 563–573).

Head, J. W., & Wilson, L. (1992). Lunar mare volcanism: Stratigraphy, eruption conditions, and the evolution of secondary crusts. *Geochimica et Cosmochimica Acta*, *56*(6), 2155–2175. https://doi.org/10.1016/0016-7037(92)90183-J

Head, J. W., & Wilson, L. (2017). Generation, ascent and eruption of magma on the Moon: New insights into source depths, magma supply, intrusions and effusive/explosive eruptions (Part 2: Predicted emplacement processes and observations). *Icarus*, *283*, 176–223. https://doi.org/10.1016/j.icarus.2016.05.031

Hiesinger, H., & Head, J. W. (2006). New views of lunar geoscience: An introduction and overview. *Reviews in Mineralogy and Geochemistry*, *60*(1), 1–81. https://doi.org/10.2138/rmg.2006.60.1

Hiesinger, H., Head, J. W., Wolf, U., Jaumann, R., & Neukum, G. (2006). New ages for basalts in Mare Fecunditatis based on crater size-frequency measurements. *Lunar Planet. Sci. XXXVII*.

Hiesinger, H., Head, J. W., Wolf, U., Jaumann, R., & Neukum, G. (2011). Ages and stratigraphy of lunar mare basalts: A synthesis. *Recent Advances and Current Research Issues in Lunar Stratigraphy*, *477*, 1–51.

Hiesinger, H., Head, J. W., Wolf, U., Neukum, G., & Jaumann, R. (2008). Ages of mare basalts on the lunar nearside: A synthesis. *Lunar and Planetary Science Conference*, 1269.

Hiesinger, H., van der Bogert, C. H., Reiss, D., & Robinson, M. S. (2011). Crater size-frequency distribution measurements of Mare Crisium. *Lunar and Planetary Science Conference*, 2179.

Hikida, H., & Wieczorek, M. A. (2007). Crustal thickness of the Moon: New constraints from gravity inversions using polyhedral shape models. *Icarus*, *192*(1), 150–166. https://doi.org/https://doi.org/10.1016/j.icarus.2007.06.015

Holsapple, K. A. (1993). The scaling of impact processes in planetary sciences. *Annual Review of Earth and Planetary Sciences*, *21*(1), 333–373. https://doi.org/10.1146/annurev.ea.21.050193.002001

Hörz, F. (1978). How thick are lunar mare basalts. *Lunar and Planetary Science Conference Proceedings*, *9*, 3311–3331.

Hörz, F., Grieve, R., Heiken, G., Spudis, P. D., & Binder, A. (1991). Lunar surface processes. *Lunar Sourcebook*, 61–120.

Hörz, F., Ostertag, R., & Rainey, D. A. (1983). Bunte Breccia of the Ries: Continuous deposits of large impact craters. In *Reviews of Geophysics* (Vol. 21, Issue 8, pp. 1667–1725). https://doi.org/10.1029/RG021i008p01667

Huang, J., Xiao, Z., Flahaut, J., Martinot, M., Head, J. W., Xiao, X., Xie, M., & Xiao, L. (2018). Geological characteristics of Von Kármán Crater, northwestern South Pole-Aitken basin: Chang'E-4 landing site region. *Journal of Geophysical Research: Planets*, *1*, 1–17. https://doi.org/10.1029/2018JE005577

Huang, Y., Minton, D. A., Masatoshi, H., Elliott, J. R., Richardson, J. E., Fassett, C. I., & Zellner, N. E. B. (2017). Heterogeneous impact transport on the Moon. *Journal of Geophysical Research: Planets*, *122*, 1–23. https://doi.org/10.1002/2016JE005160

Hubbard, N. J., Meyer, C., Gast, P. W., & Wiesmann, H. (1971). The composition and derivation of Apollo 12 soils. *Earth and Planetary Science Letters*, *10*(3), 341–350. https://doi.org/https://doi.org/10.1016/0012-821X(71)90040-9

Ivanov, B. A., & Melosh, H. J. (2003). Impacts do not initiate volcanic eruptions: Eruptions close to the crater. *Geology*, *31*(10), 869–872. https://doi.org/10.1130/G19669.1

Ivanov, M. A., Hiesinger, H., Orgel, C., Pasckert, J.-H., van der Bogert, C. H., & Head, J. W. (2018). Geology of the northern portion of the SPA basin on the Moon: Evidence for compositional stratification of the ancient lunar crust. *Lunar and Planetary Science Conference*, *49*.

Jessberger, E. K., Kirsten, T., & Staudacher, T. (1977). One rock and many ages - further K-Ar data on consortium breccia 73215. *Lunar and Planetary Science Conference Proceedings*, *2*, 2567–2580.

Jourdan, F. (2012). The 40Ar/39Ar dating technique applied to planetary sciences and terrestrial impacts. *Australian Journal of Earth Sciences*, *59*(2), 199–224. https://doi.org/10.1080/08120099.2012.644404

Jourdan, F., Mark, D. F., & Verati, C. (2014). Advances in 40Ar/ 39Ar dating: from archaeology to planetary sciences – introduction. *Geological Society, London, Special Publications*, *378*(1), 1–8. https://doi.org/10.1144/SP378.24

Jourdan, F., Renne, P. R., & Reimold, W. U. (2009). An appraisal of the ages of terrestrial impact structures. *Earth and Planetary Science Letters*, *286*(1), 1–13. https://doi.org/https://doi.org/10.1016/j.epsl.2009.07.009

Korotev, R. L. (1994). Compositional variation in Apollo 16 impact-melt breccias and inferences for the geology and bombardment history of the Central Highlands of the Moon. *Geochimica et Cosmochimica Acta*, *58*(18), 3931–3969. https://doi.org/https://doi.org/10.1016/0016-7037(94)90372-7

Korotev, R. L. (1976). Geochemistry of grain-size fractions of soils from the Taurus-Littrow valley floor. *Lunar and Planetary Science Conference Proceedings*, *7*, 695–726.

Korotev, R. L., & Gillis, J. J. (2001). A new look at the Apollo 11 regolith and KREEP. *Journal of Geophysical Research: Planets*, *106*(E6), 12339–12353. https://doi.org/https://doi.org/10.1029/2000JE001336

Korotev, R. L., & Kremser, D. T. (1992). Compositional variations in Apollo 17 soils and their relationship to the geology of the Taurus-Littrow site. *Lunar and Planetary Science Conference Proceedings*, *22*, 275–301.

Krüger, T., Kenkmann, T., & Hergarten, S. (2017). Structural uplift and ejecta thickness of lunar mare craters: New insights into the formation of complex crater rims. *Meteoritics and Planetary Science*, *52*(10), 2220–2240. https://doi.org/10.1111/maps.12925

Laneuville, M., Wieczorek, M. A., Breuer, D., & Tosi, N. (2013). Asymmetric thermal evolution of the Moon. *Journal of Geophysical Research: Planets*, *118*(7), 1435–1452. https://doi.org/10.1002/jgre.20103

Laul, J. C., & Papike, J. J. (1980). The lunar regolith-comparative chemistry of the Apollo sites. *Lunar and Planetary Science Conference Proceedings*, *11*, 1307–1340.

Laul, J. C., Vaniman, D. T., Papike, J. J., & Simon, S. (1978). Chemistry and petrology of size fractions of Apollo 17 deep drill core 70009-70006. *Lunar and Planetary Science Conference Proceedings*, *9*, 2065–2097.

Le Feuvre, M., & Wieczorek, M. A. (2011). Nonuniform cratering of the Moon and a revised crater chronology of the inner Solar System. *Icarus*, *214*(1), 1–20. https://doi.org/10.1016/j.icarus.2011.03.010

Li, C., Wang, C., Wei, Y., & Lin, Y. (2019). China's present and future lunar exploration program. *Science*, *365*(6450), 238 LP – 239. https://doi.org/10.1126/science.aax9908

Li, L., & Mustard, J. F. (2000). Compositional gradients across mare-highland contacts: Importance and geological implication of lateral transport. *Journal of Geophysical Research: Planets*, *105*(E8), 20431–20450. https://doi.org/10.1029/1999JE001168

Li, L., & Mustard, J. F. (2005). On lateral mixing efficiency of lunar regolith. *Journal of Geophysical Research: Planets*, *110*(11), 1–16. https://doi.org/10.1029/2004JE002295

Liu, T., Michael, G., Engelmann, J., Wünnemann, K., & Oberst, J. (2019). Regolith mixing by impacts : Lateral diffusion of basin melt. *Icarus*, *321*(0019–1035), 691–704. https://doi.org/10.1016/j.icarus.2018.12.026

Liu, T., Michael, G., Wünnemann, K., Becker, H., & Oberst, J. (2020). Lunar megaregolith mixing by impacts: Spatial diffusion of basin melt and its implications for sample interpretation. *Icarus*, *339*. https://doi.org/10.1016/j.icarus.2019.113609

Lucey, P., Korotev, R. L., Gillis, J. J., Taylor, L. A., Lawrence, D., Campbell, B. A., Elphic, R., Feldman, B., Hood, L. L., Hunten, D., Mendillo, M., Noble, S., Papike, J. J., Reedy, R. C., Lawson, S., Prettyman, T., Gasnault, O., & Maurice, S. (2006). Understanding the lunar surface and space-Moon interactions. *Reviews in Mineralogy and Geochemistry*, *60*(1), 83–219. https://doi.org/10.2138/rmg.2006.60.2

Luther, R., Zhu, M.-H., Collins, G., & Wünnemann, K. (2018). Effect of target properties and impact velocity on ejection dynamics and ejecta deposition. *Meteoritics & Planetary Science*, *53*(8), 1705–1732. https://doi.org/10.1111/maps.13143

Maher, B. A. (1988). Magnetic properties of some synthetic sub-micron magnetites. *Geophysical Journal*, *94*(1), 83–96. https://doi.org/10.1111/j.1365-246X.1988.tb03429.x

Maurer, P., Eberhardt, P., Geiss, J., Grögler, N., Stettler, A., Brown, G. M., Peckett, A., & Krähenbühl, U. (1978). Pre-Imbrian craters and basins: ages, compositions and excavation depths of Apollo 16 breccias. *Geochimica et Cosmochimica Acta*, *42*(11), 1687–1720. https://doi.org/10.1016/0016-7037(78)90257-0

McDougall, I., & Harrison, T. M. (1999). *Geochronology and Thermochronology by the 40Ar/39Ar Method*. Oxford University Press on Demand.

McGetchin, T. R., Settle, M., & Head, J. W. (1973). Radial thickness variation in impact crater ejecta: implications for lunar basin deposits. *Earth and Planetary Science Letters*, *20*(2), 226–236. https://doi.org/https://doi.org/10.1016/0012-821X(73)90162-3

McKay, D., Heiken, G., Basu, A., Blanford, G., Simon, S., Reedy, R., French, B. M., & Papike, J. (1991). The lunar regolith. In G. H. Heiken, D. T. Vaniman, & B. M. French (Eds.), *Lunar Source-Book: A user's guide to the Moon* (pp. 285–356). Cambridge University Press. https://doi.org/10.1006/icar.1999.6165

McKinnon, W. B., Zahnle, K. J., Ivanov, B. A., & Melosh, H. J. (1997). Cratering on Venus: Models and Observations. *Venus II: Geology, Geophysics, Atmosphere, and Solar Wind Environment*, 969.

Melosh, H. J. (1989). *Impact cratering: A geologic process*. Oxford University.

Melosh, H. J., Kendall, J., Horgan, B., Johnson, B. C., Bowling, T., Lucey, P. G., & Taylor, G. J. (2017). South Pole–Aitken basin ejecta reveal the Moon's upper mantle. *Geology*, *45*(12), 1063. https://doi.org/10.1130/G39375.1

Michael, G., Basilevsky, A., & Neukum, G. (2018). On the history of the early meteoritic bombardment of the Moon: Was there a terminal lunar cataclysm? *Icarus*, *302*, 80–103. https://doi.org/10.1016/j.icarus.2017.10.046

Michael, G., Kneissl, T., & Neesemann, A. (2016). Planetary surface dating from crater size-frequency distribution measurements: Poisson timing analysis. *Icarus*, *277*, 279–285. https://doi.org/10.1016/j.icarus.2016.05.019

Miljković, K., Collins, G. S., Wieczorek, M. A., Johnson, B. C., Soderblom, J. M., Neumann, G. A., & Zuber, M. T. (2016). Subsurface morphology and scaling of lunar impact basins. *Journal of Geophysical Research: Planets*, *121*(9), 1695–1712. https://doi.org/10.1002/2016JE005038

Morbidelli, A., Lunine, J. I., O'Brien, D. P., Raymond, S. N., & Walsh, K. J. (2012). Building terrestrial planets. *Annual Review of Earth and Planetary Sciences*, *40*(1), 251–275. https://doi.org/10.1146/annurev-earth-042711-105319

Morbidelli, A., Marchi, S., Bottke, W. F., & Kring, D. A. (2012). A sawtooth-like timeline for the first billion years of lunar bombardment. *Earth and Planetary Science Letters*, *355–356*, 144–151. https://doi.org/10.1016/j.epsl.2012.07.037

Morbidelli, A., Nesvorny, D., Laurenz, V., Marchi, S., Rubie, D. C., Elkins-Tanton, L., Wieczorek, M., & Jacobson, S. (2018). The timeline of the lunar bombardment: Revisited. *Icarus*, *305*, 262–276. https://doi.org/https://doi.org/10.1016/j.icarus.2017.12.046

Morota, T., Haruyama, J., Miyamoto, H., Honda, C., Ohtake, M., Yokota, Y., Matsunaga, T., Hirata, N., Demura, H., Takeda, H., Ogawa, Y., & Kimura, J. (2009). Formation age of the lunar crater Giordano Bruno. *Meteoritics & Planetary Science*, *44*(8), 1115–1120. https://doi.org/https://doi.org/10.1111/j.1945-5100.2009.tb01211.x

Naumenko-Dèzes, M. O., Nägler, T. F., Mezger, K., & Villa, I. M. (2018). Constraining the 40K decay constant with 87Rb-87Sr – 40K-40Ca chronometer intercomparison. *Geochimica et Cosmochimica Acta*, *220*, 235–247. https://doi.org/10.1016/j.gca.2017.09.041

Needham, D. H., & Kring, D. A. (2017). Lunar volcanism produced a transient atmosphere around the ancient Moon. *Earth and Planetary Science Letters*, *478*, 175–178. https://doi.org/10.1016/j.epsl.2017.09.002

Neukum, G. (1983). Meteoritenbombardement und Datierung Planetarer Oberflaechen. *Habilitation Dissertation for Faculty Membership, Univ. of Munich*, 1–186.

Neukum, G., & Ivanov, B. A. (1994). Crater size distributions and impact probabilities on Earth from lunar, terrestrial-planet, and asteroid cratering data. *Hazards Due to Comets and Asteroids*, *359*(1), 359–416.

Neukum, G., Ivanov, B. A., & Hartmann, W. K. (2001). Cratering records in the inner solar system in relation to the lunar reference system. *Space Science Reviews*, *96*(1–4), 55–86. https://doi.org/10.1023/A:1011989004263

Neukum, G., König, B., Fechtig, H., & Storzer, D. (1975). Cratering in the Earth-Moon system-Consequences for age determination by crater counting. *Lunar and Planetary Science Conference Proceedings*, *6*, 2597–2620.

Neumann, G. A., Zuber, M. T., Wieczorek, M. A., Head, J. W., Baker, D. M. H., Solomon, S. C., Smith, D. E., Lemoine, F. G., Mazarico, E., Sabaka, T. J., Goossens, S. J., Melosh, H. J., Phillips, R. J., Asmar, S. W., Konopliv, A. S., Williams, J. G., Sori, M. M., Soderblom, J. M., Miljković, K., … Kiefer, W. S. (2015). Lunar impact basins revealed by Gravity Recovery and Interior Laboratory measurements. *Science Advances*, *1*(9). https://doi.org/10.1126/sciadv.1500852

Niihara, T., Beard, S. P., Swindle, T. D., Schaffer, L. A., Miyamoto, H., & Kring, D. A. (2019). *Evidence for multiple 4.0 - 3 .7 Ga impact events within the Apollo 16 collection*. *698*(4), 675–698. https://doi.org/10.1111/maps.13237

Norman, M. D., Duncan, R. A., & Huard, J. J. (2006). Identifying impact events within the lunar cataclysm from 40Ar–39Ar ages and compositions of Apollo 16 impact melt rocks. *Geochimica et Cosmochimica Acta*, *70*(24), 6032–6049. https://doi.org/https://doi.org/10.1016/j.gca.2006.05.021

Norman, M. D., Duncan, R. A., & Huard, J. J. (2010). Imbrium provenance for the Apollo 16 Descartes terrain: Argon ages and geochemistry of lunar breccias 67016 and 67455. *Geochimica et Cosmochimica Acta*, *74*(2), 763–783. https://doi.org/https://doi.org/10.1016/j.gca.2009.10.024

Norman, M. D., & Nemchin, A. A. (2014). A 4.2 billion year old impact basin on the Moon: U–Pb dating of zirconolite and apatite in lunar melt rock 67955. *Earth and Planetary Science Letters*, *388*, 387–398. https://doi.org/10.1016/j.epsl.2013.11.040

Nyquist, L. E., Bogard, D. D., & Chi-Yu, S. (2001). Radiometric chronology of the Moon and Mars. In *The century of space science* (pp. 1325–1376). Springer.

Nyquist, L. E., & Shih, C. Y. (1992). The isotopic record of lunar volcanism. *Geochimica et Cosmochimica Acta*, *56*(6), 2213–2234. https://doi.org/10.1016/0016-7037(92)90185-L

O'Keefe, J. D., & Ahrens, T. J. (1977). Impact-induced energy partitioning, melting, and vaporization on terrestrial planets. *In: Lunar Science Conference*, *8*, 3357.

Oberbeck, V. R., Hörz, F., Morrison, R. H., Quaide, W. L., & Gault, D. E. (1975). On the origin of the lunar smooth plains. *The Moon*, *12*(1), 19–54.

Orgel, C., Michael, G., Fassett, C. I., van der Bogert, C. H., Riedel, C., Kneissl, T., & Hiesinger, H. (2018). Ancient bombardment of the inner solar system: Reinvestigation of the "fingerprints" of different impactor populations on the lunar surface. *Journal of Geophysical Research: Planets*, *123*(3), 748–762. https://doi.org/10.1002/2017JE005451

Osinski, G. R., & Pierazzo, E. (2012). *Impact cratering: Processes and products*. John Wiley & Sons.

Petro, N. E., & Pieters, C. M. (2004). Surviving the heavy bombardment: Ancient material at the surface of South Pole-Aitken basin. *Journal of Geophysical Research: Planets*, *109*(6). https://doi.org/10.1029/2003JE002182

Petro, N. E., & Pieters, C. M. (2006). Modeling the provenance of the Apollo 16 regolith. *Journal of Geophysical Research*, *111*(E9), E09005. https://doi.org/10.1029/2005JE002559

Phillips, R. J., Conel, J. E., Abbott, E. A., Sjogren, W. L., & Morton, J. B. (1972). Mascons: Progress toward a unique solution for mass distribution. *Journal of Geophysical Research (1896-1977)*, *77*(35), 7106–7114. https://doi.org/10.1029/JB077i035p07106

Phillips, R. J., & Lambeck, K. (1980). Gravity fields of the terrestrial planets: Long-wavelength anomalies and tectonics. *Reviews of Geophysics*, *18*(1), 27–76. https://doi.org/10.1029/RG018i001p00027

Pierazzo, E., & Melosh, H. J. (2000). Melt production in oblique impacts. *Icarus*, *145*, 252–261. https://doi.org/10.1006/icar.1999.6332

Pierazzo, E., Vickery, A. M., & Melosh, H. J. (1997). A reevaluation of impact melt production. *Icarus*, *127*(2), 408–423. https://doi.org/10.1006/icar.1997.5713

Pike, R. J. (1977). Apparent depth/apparent diameter relation for lunar craters. *Lunar and Planetary Institute Science Conference Abstracts*, *3*, 3427–3436.

Potter, R. W. K., Collins, G. S., Kiefer, W. S., McGovern, P. J., & Kring, D. A. (2012). Constraining the size of the South Pole-Aitken basin impact. *Icarus*, *220*(2), 730–743. https://doi.org/https://doi.org/10.1016/j.icarus.2012.05.032

Potter, R. W. K., Kring, D. A., Collins, G. S., Kiefer, W. S., & McGovern, P. J. (2012). Estimating transient crater size using the crustal annular bulge: Insights from numerical modeling of lunar basin-scale impacts. *Geophysical Research Letters*, *39*(18), 1–5. https://doi.org/10.1029/2012GL052981

Potts, L. V, & von Frese, R. R. B. (2003). Comprehensive mass modeling of the Moon from spectrally correlated free-air and terrain gravity data. *Journal of Geophysical Research*, *108*(E4), 5024. https://doi.org/10.1029/2000JE001440

Prettyman, T. H., Hagerty, J. J., Elphic, R. C., Feldman, W. C., Lawrence, D. J., McKinney, G. W., & Vaniman, D. T. (2006). Elemental composition of the lunar surface: Analysis of gamma ray spectroscopy data from Lunar Prospector. *Journal of Geophysical Research: Planets*, *111*(E12). https://doi.org/10.1029/2005JE002656

Quaide, W., Oberbeck, V. R., Bunch, T., & Polkowski, G. (1971). Investigations of the natural history of the regolith at the Apollo 12 site. *Lunar and Planetary Science Conference Proceedings*, *2*, 701.

Rhodes, J. M. (1977). Some compositional aspects of lunar regolith evolution. *Philosophical Transactions of the Royal Society A: Mathematical, Physical and Engineering Sciences*, *285*(1327), 293–301. https://doi.org/10.1098/rsta.1977.0068

Rhodes, J. M., Rodgers, K. V., Shih, C.-Y., Bansal, B. M., Nyquist, L. E., Wiesmann, H., & Hubbard, N. J. (1974). The relationships between geology and soil chemistry at the Apollo 17 landing site. *Lunar and Planetary Science Conference Proceedings*, *2*, 1097–1117.

Riedel, C., Michael, G., Kneissl, T., Orgel, C., Hiesinger, H., & van der Bogert, C. H. (2018). A new tool to account for crater obliteration effects in crater size-frequency distribution measurements. *Earth and Space Science*, *5*(6), 258–267. https://doi.org/10.1002/2018EA000383

Rotenberg, E., Davis, D. W., Amelin, Y., Ghosh, S., & Bergquist, B. A. (2012). Determination of the decay-constant of 87Rb by laboratory accumulation of 87Sr. *Geochimica et Cosmochimica Acta*, *85*, 41–57. https://doi.org/10.1016/j.gca.2012.01.016

Ryder, G. (1994). Coincidence in time of the Imbrium basin impact and Apollo 15 KREEP volcanic flows: The case for impact-induced melting. *Large Meteorite Impacts and Planetary Evolution*, *293*, 11.

Ryder, G. (2001). Mass flux during the ancient lunar bombardment: The cataclysm. *32nd Annual Lunar and Planetary Science Conference*.

Ryder, G., & Spudis, P. D. (1980). Volcanic rocks in the lunar highlands. In R. B. Merrill & J. J. Papike (Eds.), *Lunar Highlands Crust* (pp. 353–375).

Ryder, G., Spudis, P. D., & Taylor, G. J. (1989). The case for planetary sample return missions: Origin and evolution of the Moon and its environment. *Eos, Transactions American Geophysical Union*, *70*(47), 1495–1509. https://doi.org/10.1029/89EO00356

Schaeffer, G. A., & Schaeffer, O. A. (1977). 39Ar-40Ar ages of lunar rocks. *Lunar and Planetary Science Conference Proceedings*, *2*, 2253–2300.

Schonfeld, E. (1975). Component abundances in Apollo 15 soils and breccias by the mixing model technique. *Lunar and Planetary Science Conference*, *6*, 712.

Schonfeld, E., & Meyer, J. (1972). The abundances of components of the lunar soils by a least-squares mixing model and the formation age of KREEP. *Lunar and Planetary Science Conference Proceedings*, *3*, 1397.

Schultz, P. H., & Spudis, P. D. (1979). Evidence for ancient mare volcanism. *Lunar and Planetary Science Conference Proceedings*, *3*, 2899–2918.

Shervais, J. W., Taylor, L. A., & Lindstrom, M. M. (1985). Apollo 14 Mare basalts: Petrology and geochemistry of clasts from Consortium Breccia 14321. *Journal of Geophysical Research: Solid Earth*, *90*(S02), C375–C395. https://doi.org/10.1029/JB090iS02p0C375

Shkuratov, Y. (2001). Regolith layer thickness mapping of the Moon by radar and optical data. *Icarus*, *149*(2), 329–338. https://doi.org/10.1006/icar.2000.6545

Shuvalov, V. (2011). Ejecta deposition after oblique impacts : An influence of impact scale. *Meteoritics & Planetary Science*, *1718*(11), 1713–1718. https://doi.org/10.1111/j.1945-5100.2011.01259.x

Shuvalov, V., & Dypvik, H. (2013). Distribution of ejecta from small impact craters. *Meteoritics and Planetary Science*, *48*(6), 1034–1042. https://doi.org/10.1111/maps.12127

Simon, S. B., Papike, J. J., & Laul, J. C. (1982). The lunar regolith: Comparative studies of the Apollo and Luna sites. Petrology of soils from Apollo 17, Luna 16, 20, and 24. *Lunar and Planetary Science Conference Proceedings*, *12*, 371–388.

Snape, J. F., Nemchin, A. A., Grange, M. L., Bellucci, J. J., Thiessen, F., & Whitehouse, M. J. (2016). Phosphate ages in Apollo 14 breccias: Resolving multiple impact events with high precision U–Pb SIMS analyses. *Geochimica et Cosmochimica Acta*, *174*, 13–29. https://doi.org/10.1016/j.gca.2015.11.005

Solomon, S. C., & Head, J. W. (1980). Lunar Mascon Basins: Lava filling, tectonics, and evolution of the lithosphere. *Reviews of Geophysics*, *18*(1), 107–141. https://doi.org/10.1029/RG018i001p00107

Spudis, P. D. (1993). *The geology of multi-ring impact basins: the Moon and other planets*. Cambridge University Press. https://doi.org/10.1017/CBO9780511564581

Spudis, P. D., & Sliz, M. U. (2017). Impact melt of the lunar Crisium multiring basin. *Geophysical Research Letters*, *44*(3), 1260–1265. https://doi.org/10.1002/2016GL071429

Spudis, P. D., Wilhelms, D. E., & Robinson, M. S. (2011). The Sculptured Hills of the Taurus Highlands: Implications for the relative age of Serenitatis, basin chronologies and the cratering history of the Moon. *Journal of Geophysical Research*, *116*(12), E00H03. https://doi.org/10.1029/2011JE003903

Stöffler, D. (2006). Cratering history and lunar chronology. *Reviews in Mineralogy and Geochemistry*, *60*(1), 519–596. https://doi.org/10.2138/rmg.2006.60.05

Stöffler, D., Gault, D. E., Wedekind, J., & Polkowski, G. (1975). Experimental hypervelocity impact into quartz sand: Distribution and shock metamorphism of ejecta. *Journal of Geophysical Research*, *80*(29), 4062–4077. https://doi.org/10.1029/JB080i029p04062

Stöffler, D., Hamann, C., & Metzler, K. (2017). Shock metamorphism of planetary silicate rocks and sediments: Proposal for an updated classification system. *Meteoritics & Planetary Science*, 1–45. https://doi.org/10.1111/maps.12912

Stöffler, D., & Ryder, G. (2001). Stratigraphy and isotope ages of lunar geologic units: Chronological standard for the inner solar system. In R. Kallenbach, J. Geiss, & W. K. Hartmann (Eds.), *Chronology and Evolution of Mars* (pp. 9–54). Springer Netherlands.

Swindle, T. D., Spudis, P. D., Taylor, G. J., Korotev, R. L., Nichols R.H., J., & Olinger, C. T. (1991). Searching for Crisium Basin ejecta: Chemistry and ages of Luna 20 impact melts. *Lunar and Planetary Science Conference Proceedings*, *21*, 167–181.

Taylor, L. A., Shervais, J. W., Hunter, R. H., Shih, C.-Y., Bansal, B. M., Wooden, J., Nyquist, L. E., & Laul, L. C. (1983). Pre-4.2 AE mare-basalt volcanism in the lunar highlands. *Earth and Planetary Science Letters*, *66*, 33–47. https://doi.org/10.1016/0012-821X(83)90124-3

Tera, F., Papanastassiou, D. A., & Wasserburg, G. J. (1974). Isotopic evidence for a terminal lunar cataclysm. *Earth and Planetary Science Letters*, *22*(1), 1–21. https://doi.org/10.1016/0012-821X(74)90059-4

Thomson, B. J., Grosfils, E. B., Bussey, D. B. J., & Spudis, P. D. (2009). A new technique for estimating the thickness of mare basalts in Imbrium Basin. *Geophysical Research Letters*, *36*(12). https://doi.org/https://doi.org/10.1029/2009GL037600

Tonks, W. B., & Melosh, H. J. (1993). Magma ocean formation due to giant impacts. *Journal of Geophysical Research: Planets*, *98*(E3), 5319–5333. https://doi.org/10.1029/92JE02726

Trombka, J., Arnold, J. R., Adler, I., Metzger, A. E., & Reedy, R. C. (1977). Lunar elemental analysis obtained from the Apollo gamma-ray and X-ray remote sensing experiment. In *NASA Special Publication* (Vol. 370, pp. 153–182).

Tsiganis, K., Gomes, R., Morbidelli, A., & Levison, H. F. (2005). Origin of the orbital architecture of the giant planets of the Solar System. *Nature*, *435*, 459.

Turner, G., Cadogan, P. H., & Yonge, C. J. (1973). Apollo 17 age determinations. *Nature*, *242*(5399), 513–515. https://doi.org/10.1038/242513b0

van der Bogert, C. H., Hiesinger, H., Spudis, P. D., Fernandes, V. A., Runyon, K. D., & B.W., D. (2018). Constraining the age of the Crisium impact basin. *European Lunar Symposium*.

Vanderliek, D. M., Becker, H., & Rocholl, A. (2018). In situ U-Pb dating of lunar breccia 15455: Impact resetting and growth of zircons at 4.2 Ga. *Lunar and Planetary Science Conference*, *49*, 1931.

Vaniman, D., Dietrich, J., Taylor, G. J., & Heiken, G. (1991). Exploration, samples, and recent concepts of the Moon. In G. H. Heiken, D. T. Vaniman, & B. M. French (Eds.), *Lunar Source-Book: A user's guide to the Moon* (pp. 5–26). Cambridge University Press.

Warren, P. H., & Wasson, J. T. (1977). Pristine nonmare rocks and the nature of the lunar crust. *Lunar and Planetary Science Conference Proceedings*, *2*, 2215–2235.

Wartho, J.-A., Kelley, S. P., & Elphick, S. C. (2014). Ar diffusion and solubility measurements in plagioclases using the ultra-violet laser depth-profiling technique. *Geological Society, London, Special Publications*, *378*(April 2014), 137–154. https://doi.org/10.1144/SP378.13

Whitten, J. L., & Head, J. W. (2015a). Lunar cryptomaria: Mineralogy and composition of ancient volcanic deposits. *Planetary and Space Science*, *106*, 67–81. https://doi.org/https://doi.org/10.1016/j.pss.2014.11.027

Whitten, J. L., & Head, J. W. (2015b). Lunar cryptomaria: Physical characteristics, distribution, and implications for ancient volcanism. *Icarus*, *247*, 150–171. https://doi.org/https://doi.org/10.1016/j.icarus.2014.09.031

Wieczorek, M. A., & Phillips, R. J. (1999). Lunar multiring basins and the cratering process. *Icarus*, *139*, 246–259. https://doi.org/10.1006/icar.1999.6102

Wieczorek, M. A., Weiss, B. P., & Stewart, S. T. (2012). An impactor origin for lunar magnetic anomalies. *Science*, *335 6073*, 1212–1215.

Wilhelms, D. E. (1987). The geologic history of the Moon. In *U.S. Geological Survey Professional Paper* (Vol. 1348). https://doi.org/10.1007/s13398-014-0173-7.2

Williams, K. K., & Zuber, M. T. (1998). Measurement and analysis of lunar basin depths from Clementine altimetry. *Icarus*, *131*(1), 107–122. https://doi.org/https://doi.org/10.1006/icar.1997.5856

Wilson, L., & Head, J. W. (2017). Generation, ascent and eruption of magma on the Moon: New insights into source depths, magma supply, intrusions and effusive/explosive eruptions (Part 1: Theory). *Icarus*, *283*, 146–175. https://doi.org/10.1016/j.icarus.2015.12.039

Wood, J. A. (1970). Petrology of the lunar soil and geophysical implications. *Journal of Geophysical Research*, *75*(32), 6497–6513. https://doi.org/10.1029/JB075i032p06497

Wood, J. A., Dickey Jr, J. S., Marvin, U. B., & Powell, B. N. (1970). Lunar anorthosites and a geophysical model of the moon. *Geochimica et Cosmochimica Acta Supplement*, *1*, 965.

Wu, W., Wang, Q., Tang, Y., Yu, G., Liu, J., Zhang, W., Ning, Y., & Lu, L. (2017). The lunar far side soft landing design of "Chang'E-4" mission (Chinese). *Journal of Deep Space Exploration*, *4*(2), 111–117.

Wünnemann, K., Collins, G. S., & Melosh, H. J. (2006). A strain-based porosity model for use in hydrocode simulations of impacts and implications for transient crater growth in porous targets. *Icarus*, *180*(2), 514–527. https://doi.org/https://doi.org/10.1016/j.icarus.2005.10.013

Wünnemann, K., Collins, G. S., & Osinski, G. R. (2008). Numerical modelling of impact melt production in porous rocks. *Earth and Planetary Science Letters*, *269*(3), 530–539. https://doi.org/https://doi.org/10.1016/j.epsl.2008.03.007

Wünnemann, K., Zhu, M.-H., & Stöffler, D. (2016). Impacts into quartz sand: Crater formation, shock metamorphism, and ejecta distribution in laboratory experiments and numerical models. *Meteoritics and Planetary Science*, *51*(10), 1762–1794. https://doi.org/10.1111/maps.12710

Zellner, N. E. B. (2017). Cataclysm no more: New views on the timing and delivery of lunar impactors. *Origins of Life and Evolution of Biospheres*, *47*(3), 261–280. https://doi.org/10.1007/s11084-017-9536-3

Zhu, M.-H., Artemieva, N., Morbidelli, A., Yin, Q.-Z., Becker, H., & Wünnemann, K. (2019). Reconstructing the late-accretion history of the Moon. *Nature*, *571*(7764), 226–229. https://doi.org/10.1038/s41586-019-1359-0

Zhu, M.-H., & Wünnemann, K. (2013). Modeling of meteorite impact-induced secondary mass wasting {\mdash} Case study by means of the Bunte breccia ejecta blanket at Ries crater, Germany. *Lunar and Planetary Science Conference*, *44*, 1921.

Zhu, M.-H., Wünnemann, K., & Artemieva, N. (2017). Effects of Moon's thermal state on the impact basin ejecta distribution. *Geophysical Research Letters*, *44*(22), 11,211-292,300. https://doi.org/10.1002/2017GL075405

Zhu, M.-H., Wünnemann, K., & Potter, R. W. K. (2015). Numerical modeling of the ejecta distribution and formation of the Orientale basin on the Moon. *Journal of Geophysical Research: Planets*, *120*(12), 2118–2134. https://doi.org/https://doi.org/10.1002/2015JE004827

Zou, Y. L., & Li, W. (2017). Scientific visions of lunar research-station from China. *Lunar and Planetary Science Conference*, 1730.